Exploiting multiple antennas in maritime radio channels

Sandra, Michiel

2025

Document Version:
Publisher's PDF, also known as Version of record

Exploiting Multiple Antennas in Maritime Radio Channels

Michiel Sandra

Doctoral Dissertation
Electrical Engineering

Lund University
Lund, Sweden
2025

Doctoral dissertation which, by due permission of the Faculty of Engineering, Lund University, will be publicly defended on June 13, 2025, at 9.15 a.m. in lecture hall E:1406, Klas Anshelms väg 10, Lund, for the degree of Doctor of Philosophy in Electrical Engineering.

Department of Electrical and Information Technology
Communications Engineering
Lund University
P.O. Box 118, S-221 00 Lund, Sweden

Series of licentiate and doctoral theses
ISSN: 1654-790X; No.187
ISBN: 978-91-8104-575-8 (print)
ISBN: 978-91-8104-576-5 (pdf)

Typeset in Computer Modern 10 pt using LaTeX and BibTeX.
Printed in Sweden by *Tryckeriet i E-huset*, Lund University, Lund.
May, 2025

To my wife

Abstract

Reliable maritime communication systems are essential for both safety-critical operations and emerging applications such as autonomous shipping, remote pilotage, and drone-assisted search and rescue. These scenarios demand ultra-reliable, low-latency wireless connectivity, where communication outages are unacceptable. Equally important is the need for dependable positioning systems. In situations where GNSS (Global Navigation Satellite System) signals are unreliable, a robust backup positioning solution is essential. Recent wireless technology trends, such as massive multiple-input multiple-output (MIMO) in fifth-generation (5G) and distributed MIMO in future sixth-generation (6G) networks, involve the deployment of large-scale antenna arrays to enhance reliability and capacity. Inspired by these developments, this thesis investigates the use of multiple antennas in maritime radio channels to improve both communication reliability and positioning capability. The investigation focuses on sea surface fading mitigation and ranging, supported by both theoretical analysis and real-world measurements. A high-performance wideband distributed massive MIMO channel sounder operating in the 5 GHz band was developed to support this research. The sounder is also well-suited for broader 6G research, including distributed MIMO and joint communication and sensing. The thesis demonstrates that deploying multiple antennas, particularly in vertical configurations, yields significant advantages for maritime wireless systems. Through a combination of analytical modeling and empirical measurements, it shows that vertical antenna arrays can effectively mitigate deep fading caused by sea surface reflections. Closed-form expressions based on the two-ray model are derived to identify optimal antenna spacing and array configurations and to provide practical design insights. Experimental validation in open-sea environments confirms that even arrays of only three elements can enhance link reliability by up to 15 dB. Furthermore, the two-ray model is extended to enable GNSS-independent ranging between vessels and base stations on land without requiring time synchronization, achieving sub-10-meter accuracy with eight vertically distributed antennas, offering a viable independent positioning method.

Popular science summary

Maritime communication was one of the first applications of wireless technology and has played a crucial role in ensuring safety and aiding navigation at sea. As technology evolves, new applications are emerging, such as autonomous shipping and remote pilotage, which require faster and more reliable connectivity. Wireless communication networks can also provide position information, offering vital redundancy when GPS malfunctions or experiences disturbances, ensuring continuous navigational safety in maritime environments.

To enhance maritime wireless systems, multiple antennas have been employed since the early days of wireless communication. Despite successful integration in other wireless networks, the application of multiple antennas in modern maritime communication systems has been limited and under-investigated. To fully understand how multiple antennas could improve reliability and to realize their potential in maritime environments, detailed measurements of their behavior in these environments are necessary. These measurements form the basis for mathematical models that help predict and optimize system performance and coverage. To this end, a novel, highly flexible measurement system was designed and implemented in the first stage of this research. The system is capable of measuring wireless signals with hundreds of antennas in various environments, including maritime settings, and is a crucial tool for developing future wireless networks such as 6G. Using this measurement system, two measurement campaigns were conducted, providing the data necessary for addressing the research questions in this thesis.

It is well established that more antennas generally lead to better reliability but also incur greater costs. Hence, the questions emerge: How many antennas are sufficient? And what should be their optimal spacing? This thesis demonstrates that vertical orientation of antennas is essential, and provides practical formulas to calculate the required number of antennas and their spacing based on coverage requirements.

The maritime environment can be highly diverse, as vessels operate in both busy harbors and open seas. Therefore, this thesis investigates the differences that exist in signal characteristics between in-harbor environments and open-sea conditions. Measurements show that signal variability can change rapidly, highlighting the dynamic nature of maritime communication. Understanding and addressing these rapid variations is important for ensuring reliable communication.

Since other contributions of the thesis demonstrated that multiple vertically-oriented antennas are beneficial for communication performance, the question arises whether this antenna configuration is also useful for positioning. The answer is affirmative. This thesis presents an algorithm that estimates the distance between a vessel and a land-based wireless station, achieving an average error under 10 meters, which is comparable to GPS accuracy. The algorithm addresses various real-world challenges, making it nearly ready for implementation in real communication systems. The novel positioning technique complements other positinging techniques and could provide redundancy when GPS is unreliable, increasing safety at sea.

Preface

This thesis summarizes the research I have carried out over the years at the Department of Electrical and Information Technology, Lund University, Sweden. The thesis starts with an introduction to the research field followed by the scientific papers as listed below.

List of Included Papers

Paper I M. Sandra, G. Tian, X. Cai, A. J. Johansson, "Antenna Array Configuration for Reliable Communications in Maritime Environments," *2022 IEEE 95th Vehicular Technology Conference (VTC Spring)*, Helsinki, Finland, 2022.

Contributions of the author: I conceived the idea for this paper, derived the equations, implemented the simulations in Python, and drafted the complete manuscript.

Paper II M. Sandra, G. Tian, A. Fedorov, X. Cai, A. J. Johansson, "Measurement-Based Wideband Maritime Channel Characterization," *2023 17th European Conference on Antennas and Propagation (EuCAP)*, Florence, Italy, 2023.

Contributions of the author: I designed and built the measurement system, planned the measurement campaign, and carried it out with the support of my colleagues. Afterward, I conducted all the data analysis and took the lead in writing the manuscript.

Paper III M. Sandra, C. Nelson, X. Li, X. Cai, A. J. Johansson, "A Wideband Distributed Massive MIMO Channel Sounder for Communication and Sensing," *IEEE Transactions on Antennas and Propagation*, 2025.

Contributions of the author: I designed and implemented the channel sounder, handling every aspect from antenna design and component sourcing to assembly, FPGA programming, PCB design, laser cutting, 3D printing, and software development. I performed calibration of the antenna patterns in the anechoic chamber, for which I also planned and executed the measure-

ment campaign alongside some of my colleagues. Additionally, I developed the SAGE code for the high-resolution parameter estimation algorithm from scratch and drafted the full manuscript.

Paper IV M. Sandra, S. Willhammar, A. J. Johansson, "Mitigating Sea Surface Fading with D-MIMO: Experimental Validation," *2025 19th European Conference on Antennas and Propagation (EuCAP)*, Stockholm, Sweden, 2025.

Contributions of the author: The theoretical derivations forming the foundation of this work were originally developed by me in Paper I. I planned and carried out the measurements with the support of a few colleagues. Afterward, I processed the data and took the lead in writing the manuscript.

Paper V M. Sandra, M. Wirsing, S. Willhammar, R. Raulefs, A. J. Johansson, "Leveraging the Two-Ray Model for C-band Ranging in Maritime Applications," *Submitted to IEEE Transactions on Vehicular Technology*, 2025.

Contributions of the author: I conceived the idea for this paper and derived both the estimator and the Cramér-Rao bound. For measurement validation, I utilized the same dataset as in Paper IV. Additionally, I progressively refined the model by incorporating calibration parameters to enhance ranging performance. In parallel, I developed and implemented the estimation algorithm and all the other data processing software. Finally, I took the lead in drafting the entire manuscript.

Other Scientific Work by the Author

The author of this dissertation is also the author or co-author of the following publications and scientific work which are related to but not considered part of the dissertation:

- M. Sandra, S. Willhammar and A. J. Johansson, "Internet of Buoys: An Internet of Things Implementation at Sea," *2020 54th Asilomar Conference on Signals, Systems, and Computers*, Pacific Grove, CA, USA, 2020, pp. 1096-1100.
- M. Sandra, C. Nelson and A. J. Johansson, "Ultrawideband USRP-Based

Channel Sounding Utilizing the RFNoC Framework," *2022 IEEE Conference on Antenna Measurements and Applications (CAMA),* Guangzhou, China, 2022.

- G. Tian, I. Yaman, M. Sandra, X. Cai, L. Liu and F. Tufvesson, "High-Precision Machine-Learning Based Indoor Localization with Massive MIMO System," *ICC 2023 - IEEE International Conference on Communications*, Rome, Italy, 2023, pp. 3690-3695.

- G. Callebaut et al., "An Open Dataset Storage Standard for 6G Testbeds," *2023 IEEE Conference on Antenna Measurements and Applications (CAMA)*, Genoa, Italy, 2023, pp. 347-352.

- G. Tian, I. Yaman, M. Sandra, X. Cai, L. Liu and F. Tufvesson, "Deep-Learning-Based High-Precision Localization With Massive MIMO," in *IEEE Transactions on Machine Learning in Communications and Networking*, vol. 2, pp. 19-33, 2024.

- I. Yaman et al., "The LuViRA Dataset: Synchronized Vision, Radio, and Audio Sensors for Indoor Localization," *2024 IEEE International Conference on Robotics and Automation (ICRA)*, Yokohama, Japan, 2024, pp. 11920-11926.

- Y. Xu, M. Sandra, X. Cai, S. Willhammar and F. Tufvesson, "Spatial Separation of Closely-Spaced Users in Measured Distributed Massive MIMO Channels," *2024 IEEE 25th International Workshop on Signal Processing Advances in Wireless Communications (SPAWC)*, Lucca, Italy, 2024, pp. 381-385.

Acknowledgments

This work would not have been possible without the support, encouragement, and contributions of many wonderful people. First of all, I am deeply grateful to my incredible wife, whose unwavering emotional support, patience, and belief in me helped carry me through the most challenging moments of this journey. Соня, я тебя люблю!

I would like to sincerely thank my supervisor, Anders J Johansson, for offering me the opportunity to embark on this research path and for granting me the freedom and trust to explore it in my own way, at times perhaps a bit too freely, but always with encouragement and a listening ear. Your openness to my ideas and consistent support have meant a great deal.

My heartfelt thanks also go to my co-supervisor, Xuesong Cai, for the many technical insights you shared, for the confidence you instilled in me during key stages of my journey, and for learning me how to write a good response letter. Your guidance and insightful discussions were invaluable.

I am especially thankful to Guoda Tian, who played a key role in helping me write my first "academic rubbish" (his words), and who introduced me into the academic world with a healthy dose of humor. Our whiteboard sessions, trips, and shared laughs helped make this experience not just intellectually rewarding, but genuinely fun.

I am also grateful to Christian Nelson for the many engaging conversations about hardware and channel sounders.

The colleagues I have had the pleasure of working with, including Juan V, Ilayda, Aleksei, Sara, Fredrik T, Xuhong, Yingjie, Vincent, Hedieh, Ashkan, Emil, Aleksandar, Yujie, Yu-Yan, Ove, John B, Michael, Jiawang, Susanna, Makambi, Juan S, Neharika, Ali, Galina, Johan S, Johan T, Amirreza, Linus, Leif, Russ, Dino, Junshi, have all contributed in various ways, and I am thankful for the supportive environment we shared.

Looking further back, my adventure in Lund began with an Erasmus exchange during my master studies at KU Leuven, an opportunity that was made possible thanks to the efforts of Liesbet Van der Perre and Sara Willhammar.

I also want to thank my colleagues at the German Aerospace Center (DLR), Ronald, Michael, Robert, Christian, Armin, and Markus, for the engaging discussions and the welcoming atmosphere during my research visit there.

On a more personal note, I am deeply thankful for the love and support of my family. Aan mijn familie in België, dank jullie wel voor jullie onvoorwaardelijke

steun, liefde, aanmoediging en geloof in mij. In het bijzonder wil ik mijn ouders, pappie, mijn broer en mijn grootouders bedanken. Jullie hebben mijn hele traject van dichtbij gevolgd en zijn altijd een bron van motivatie geweest.
Спасибо моей семьей в России, особенно моей тёще Татьяне и тестю Юрию. Ваша поддержка и интерес к моей работе значат для меня очень многое.
To my friends, thank you for your support and all the fun that kept me sane throughout this journey.
Finally, I wish to thank the Klagshamn Harbor Association for allowing us to use part of the harbor infrastructure for our measurement campaigns.

Acronyms and Abbreviations

1PPS 1 pulse-per-second

3GPP 3rd generation partnership project

5G fifth-generation

6G sixth-generation

AoA angle-of-arrival

AoD angle-of-departure

CFO carrier frequency offset

CPU central-processing unit

DFT discrete Fourier transform

D-MIMO distributed MIMO

EM electromagnetic

FFT fast Fourier transform

FPGA field-programmable gate array

FR3 Frequency Range 3

GNSS global navigation satellite system

GPS Global Positioning System

GSCM geometry-based stochastic channel model

IMO International Maritime Organization

IMU inertial measurement unit

ISAC integrated sensing and communication

JCAS joint communication and sensing

LAN local area network

LNA low-noise amplifier

LoS line-of-sight

MIMO multiple-input multiple-output

MPC multipath component

MU-MIMO multi-user multiple-input multiple-output

NLoS non line-of-sight

NTN non-terrestrial network

NTP network time protocol

OFDM orthogonal frequency-division multiplexing

OTA over-the-air

PA power amplifier

PAPR peak-to-average power ratio

PNT Position, Navigation and Timing

RF radio frequency

RFNoC RF Network-on-Chip

RMS root-mean-square

RMSE root mean square error

RTK real time kinematics

SAR synthetic aperture radar

SDR software-defined radio

SLAM simultaneous localization and mapping

SNR signal-to-noise ratio

SPM small perturbation method

SSD solid state drive

SU-MIMO single-user multiple-input multiple-output

TDD time division duplexing

TDoA time-difference-of-arrival

TN terrestrial network

ToA time-of-arrival

ToF time-of-flight

UAV unmanned aerial vehicle

UHD USRP hardware driver

USRP universal software radio peripheral

UTC universal time

UWB ultrawideband

VHF very high frequency

VNA vector network analyzer

ZMCSCG zero-mean circularly symmetric complex Gaussian

Contents

Abstract v
Popular science summary vii
Preface ix
List of Included Papers ix
Other Scientific Work by the Author x
Acknowledgments xiii
Acronyms and Abbreviations xvii
Contents xix
Part I: Introduction and Research Overview 1

1 Introduction **3**
1.1 Background and Motivation 3
1.2 Scope and Outline 5
1.3 Limitations 8
1.4 Research Questions 8

2 Maritime Radio Channel **9**
2.1 Propagation Mechanisms in Maritime Environments 10
2.2 Channel Modeling at Sea 12

3 Channel Sounding **19**
3.1 Introduction 19
3.2 Channel Sounder Requirements and Constraints 22
3.3 Channel Sounder Design and Implementation 25
3.4 Metadata 31
3.5 Calibration 32

4 Applications with Multiple Antennas at Sea **33**
4.1 Maritime Communication Systems 33
4.2 Radio-based Positioning 36

5 Contributions and Conclusions **41**
5.1 General Conclusions 41
5.2 Research Contributions 42
5.3 Future Work 45
5.4 Outlook 46
Part II: Included Papers 57
I Antenna Array Configuration for Reliable Communications in Maritime Environments 59
1 Introduction 61
2 Channel Model 62
3 Analysis 64
4 Results and Discussion 67
5 Conclusion 70
II Measurement-Based Wideband Maritime Channel Characterization 75
1 Introduction 77
2 Measurement campaign and setup 78
3 Data processing 80
4 Results and discussion 80
5 Conclusion 85
6 Acknowledgment 85
III A Wideband Distributed Massive MIMO Channel Sounder for Communication and Sensing 89
1 Introduction 91
2 Design and Implementation 95
3 Post-processing and calibration 107
4 Verification and Measurements 109
5 Conclusions 113
IV Mitigating Sea Surface Fading with D-MIMO: Experimental Validation 121
1 Introduction 123
2 Fading Mitigation at Sea 124
3 Measurement campaign and setup 126
4 Signal model and data processing 127
5 Results and Analysis 128
6 Conclusion 132

V Leveraging the Two-Ray Model for C-band Ranging in Maritime Applications 135
1 Introduction 137
2 The Ranging Problem 140
3 Measurement equipment and campaign 144
4 Calibrated Channel Model and Parameter Estimation 146
5 Parameter Estimation Results 152
6 Range Estimation Results 159
7 Conclusion 160

Part I: Introduction and Research Overview

Michiel Sandra

Chapter 1

Introduction

1.1 Background and Motivation

One of the first wireless applications was wireless communication over sea, which transformed maritime safety and navigation. In 1897, Guglielmo Marconi demonstrated the first successful wireless transmission over the Bristol Channel, proving that radio waves could travel long distances over water [1]. By the early 1900s, wireless telegraphy had become an essential tool for ships, allowing them to send distress signals, weather updates, and navigational alerts. This technology played a crucial role in the Titanic disaster of 1912, when SOS transmissions helped facilitate the rescue of hundreds of passengers. The success of wireless communication at sea marked the beginning of modern radio technology, leading to widespread adoption in aviation, military operations, and commercial telecommunications.

Today, wireless communication remains crucial for maritime safety and navigation at sea, but with the advancements in modern technology, new applications are emerging, placing greater demands on wireless systems. In general, modern technology requires high-bandwidth data transfer to support conventional applications such as video streaming and real-time monitoring. However, maritime-specific applications, such as remote pilotage [2], autonomous shipping [3], and search and rescue operations, require even higher levels of reliability and performance from wireless networks. Remote pilotage enables experienced pilots to assist vessels in navigating complex waterways, ports, and hazardous areas without being physically on board, reducing risks, saving time, and lowering operational costs. This application requires ultra-reliable, low-latency connectivity, as any disruption in communication could compromise navigational safety. Similarly, autonomous shipping relies heavily on continuous and stable wireless

connectivity, where any interruption could lead to navigational failures or even catastrophic incidents. In addition, search and rescue services are looking into using unmanned aerial vehicles (UAVs) to enhance their operations [4]. Remote control of UAVs over vast maritime areas is dependent on ultra-reliable, low-latency wireless networks, especially in challenging environments. As these applications continue to evolve, the demand for high-capacity, low-latency, and resilient wireless systems will only grow.

State-of-the-art wireless systems are already capable of meeting some requirements. These systems can be broadly classified into terrestrial networks (TNs) and non-terrestrial networks (NTNs). NTNs, such as Starlink and Inmarsat, offer the advantage of global coverage. However, they come with significant drawbacks, including high costs and practical limitations. For example, installing a Starlink antenna on a lightweight UAV is often unfeasible due to weight and power constraints. As a result, there is strong interest in delivering wireless connectivity in coastal areas via TNs. Maritime communications have been recognized as a vertical domain of fifth-generation (5G) networks since 3rd generation partnership project (3GPP) Release 16. In this context, the 3GPP standardization team [5] developed a dedicated specification. In the future, sixth-generation (6G) networks are expected to further expand maritime connectivity by integrating TN and NTN, enabling coverage even in remote and sparsely populated coastal regions [6].

In addition to wireless communications, positioning and navigation play a vital role in ensuring maritime safety and supporting the development of emerging maritime applications. Although global navigation satellite system (GNSS) has been the most prominent technology for these functions, its reliability can be compromised in certain environments, making alternative positioning methods crucial, especially in high-risk situations [7]. These situations may include dense maritime traffic, narrow waterways with shallow depths, or navigation within harbors, both with and without the aid of pilot vessels. To address these challenges, the International Maritime Organization (IMO) issued guidelines (MSC.1/Circ.1575) outlining best practices for shipborn Position, Navigation and Timing (PNT) data processing [8]. The objective is to improve navigational safety and efficiency by promoting a modular system architecture capable of integrating data from various sensors and services. The rise of new wireless network technologies has also marked a shift in the maritime sector, which is now actively exploring applications of cellular radio systems for both broadband connectivity and navigational support. A major benefit of employing 5G (or

future 6G) networks for positioning and navigation is that the existing network infrastructure can be used, leading to high coverage without additional cost.

Multiple antennas have been an integral part of wireless communication systems since their invention. The first application of multiple antenna technology can be traced back to phased arrays for beamforming, which enabled directional transmission and reception of radio signals. Multiple antenna technology has evolved to serve various purposes, including antenna diversity to combat fading, spatial multiplexing to increase data throughput, or direction finding for positioning applications. More recent developments have led to massive multiple-input multiple-output (MIMO) systems [9, 10], which employ on the order of hundreds of antenna elements to serve multiple users simultaneously, and distributed MIMO systems, where the antenna arrays are geographically separated to improve the reliability and spatial separability of the users [11]. In the maritime domain, several existing communication systems already utilize multiple antennas, primarily for beamforming and diversity purposes. For example, maritime very high frequency (VHF) systems often employ two antennas to mitigate the effects of multipath fading and improve reliability.

Multiple antenna technology is expected to continue to play a key role in future communication systems such as 6G. Nevertheless, the effective implementation of maritime communication systems with multiple antennas requires a comprehensive understanding of the propagation environment, which can be achieved through channel measurements and modeling. Although numerous sophisticated (massive) MIMO measurements have been performed and channel models have been developed for environments on land, the maritime setting presents unique properties that distinguish it significantly from land-based scenarios. Despite considerable research in maritime channel modeling, there remains a notable gap in the literature on multiple antenna applications in maritime environments. This thesis seeks to contribute to closing that gap by investigating two multi-antenna applications in maritime radio channels: fading mitigation and ranging.

1.2 Scope and Outline

This thesis investigates two applications of multiple antennas in maritime environments: fading mitigation and ranging, enhancing both communication reliability and positioning capability of wireless networks. Both applications depend heavily on sufficient understanding of the wireless propagation environment at sea, which can be done through channel models. A channel model is a simplified

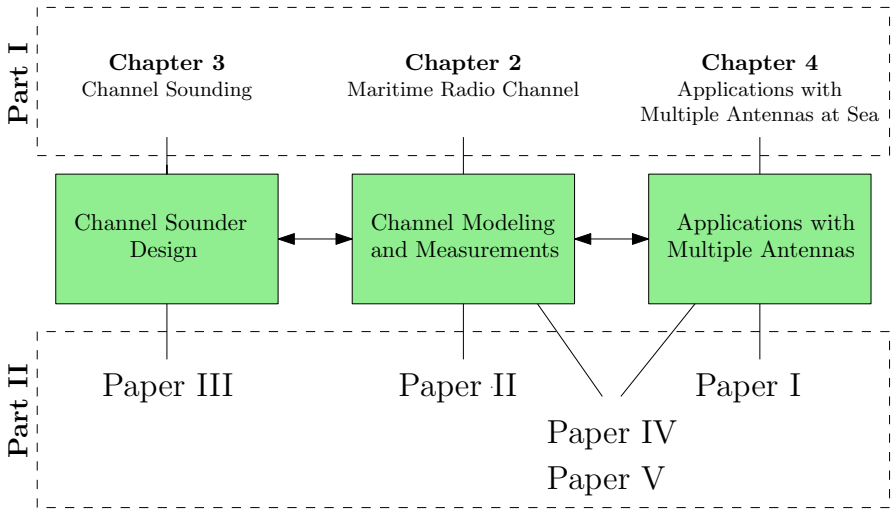

Figure 1.1: Illustration of the scope of the thesis.

and structured representation of the wireless channel that captures the essential characteristics of electromagnetic (EM) wave propagation in a given environment. These models are inherently based on assumptions and simplifications, and their effectiveness depends largely on how well they represent the environment relevant to the target application. Because channel models cannot fully capture the complexities of real-world maritime environments, empirical channel measurements are necessary. These measurements can serve two functions: they can directly contribute to the development of new channel models or they can be utilized to validate and evaluate the applicability of existing models for specific use cases. To enable such measurements, a significant part of this thesis is devoted to the design and development of a state-of-the-art channel sounder. Although the sounder is designed with the flexibility to support a wide range of 6G use cases, a particular emphasis was placed on portability and ease of deployment to ensure its practicality in challenging maritime conditions.

The scope of the thesis spans channel sounder design, channel modeling and measurements, and applications with multiple antennas. This thesis is divided into two parts. Part I contains an introduction to the research field to give more context to the compilation of research articles in Part II. The relation between the chapters of Part I and the papers in Part II is illustrated in Fig. 1.1, as well as the connection between the papers themselves.

Paper I presents an analysis of the antenna array configuration for a land-based base station, examining the orientation of the array, the number of antenna

elements required, and the required spacing of the array elements to mitigate deep fades caused by the reflection of the sea surface. The analysis relies on an analytical derivation utilizing the well-known two-ray channel. Motivated by the need for multi-antenna channel measurements at sea, a wideband distributed massive MIMO channel sounder has been developed and presented in Paper III. Note that the channel sounder is not limited to maritime environments. The system has also been deployed in other environments and has the novel capabilities necessary to support 6G research and development. Using an initial version of the channel sounder implementation, a single-antenna channel measurement has been performed in Paper II. In this paper, the multipath behavior and wideband properties of the maritime channel have been investigated. When the extension of the channel sounder to multiple antennas had been completed, a channel measurement at sea with a sailboat and a large vertical antenna array was performed and the results have been used in Paper IV and Paper V. In Paper IV, the theoretical findings of Paper I have been verified by measurements. For the ranging application in Paper V, the results of Paper I have been used to evaluate the lower bound of the Cramér-Rao range problem. The two-ray model also has been extended by integrating several calibration parameters that are needed to fit the measurement to the channel model. A novel channel estimation algorithm has also been introduced that can estimate the calibration parameters, the average reflection coefficient, and the instantaneous antenna height on the sailboat. The channel model is then applied to estimate the distance between a vessel and a base station. In addition, the estimation problem is investigated and solved, supported by measurement data.

Chapter 2 provides an overview of the propagation mechanisms in a maritime environment and how they have been mathematically modeled in the recent literature as well as in the research articles in Part II. In particular, it gives more background to the two-ray model used in the papers and its assumptions and limitations. Chapter 3 presents the field of channel sounding and elaborates on different strategies to build a channel sounder. In addition, more details on how the channel sounder in Paper III is built are included, together with the motivations behind the design choices. Chapter 4 introduces applications with multiple antennas at sea with a focus on fading mitigation and radio-based positioning. Finally, the contributions and conclusions are summarized in Chapter 5.

1.3 Limitations

The investigations in this thesis are limited to a single maritime communication scenario in which a vessel or an UAV is connected to a land-based base station equipped with a vertical antenna array. The research work is also limited to coastal areas, which extend up to several tens of kilometers from the shoreline, typically up to the 60% Fresnel zone clearance distance. Up to this distance, the propagation environment is assumed to be unobstructed and diffraction loss owing to the curvature of the Earth is assumed to be negligible. The ducting effect is also not considered. The results and insights this thesis provides therefore go into the design of wireless systems close to the shore. Addressing limitations is identified as a possible direction for future work.

1.4 Research Questions

The research work summarized in this thesis can be summarized by the following research questions:

- How can a scalable, cost-effective, and high-performance channel sounder be designed and implemented to enable wideband, phase-coherent, multi-node distributed massive MIMO measurements for both communication and integrated sensing applications?
- How many antennas should be deployed at the base station and how much should they be spaced to effectively mitigate fading in maritime applications?
- What is the multipath behavior in different maritime environments and what effect do they have on the channel?
- Can we avoid time synchronization in one-way ranging in maritime applications?

Chapter 2

Maritime Radio Channel

The wireless propagation channel is the medium through which signals travel from the transmitter to the receiver. Its characteristics directly influence the information-theoretic capacity and the behavior of wireless systems. Therefore, understanding the wireless channel is crucial both for analyzing communication limits and designing reliable wireless systems [12].

The modeling of EM wave propagation fundamentally emerges from Maxwell's equations. Although these equations fully describe EM phenomena, they are often impractical for analyzing real-world wireless communication systems. Instead, engineers and designers typically understand and model EM wave propagation through simpler propagation mechanisms that capture the key physical effects: reflection, diffraction, scattering, etc. For frequencies where the wavelength is much smaller than the objects in the environment, ray optics provides a useful approximation. In this approach, EM waves are modeled as rays that travel in straight lines and interact with the environment according to geometric principles. This ray-tracing technique is particularly effective for modeling reflection and direct path propagation. It is important to note that ray optics cannot adequately model phenomena such as diffraction, which require "wave-based" approaches since diffraction fundamentally involves the wave nature of EM radiation. The ray-tracing technique has been very popular for modeling the maritime radio channel, which is the basis for the popular two-ray model used to describe the effect of the sea surface reflection. For an extensive overview and history of channel models, the reader is referred to [12,13] and references therein.

This chapter starts with an introduction of the propagation mechanisms that constitute the terrestrial maritime radio channel. The subsequent section reviews how several of these effects have been modeled in the existing literature, with a

focus on aspects most relevant to the research papers presented in Part II.

2.1 Propagation Mechanisms in Maritime Environments

In the following subsections the propagation mechanisms are introduced according to the "interacting objects". Note that propagation mechanisms below 100 MHz are not included as they are irrelevant for today's commercial wireless systems. For example, we have not included ground-wave propagation as it is negligible above 30 MHz.

2.1.1 Sea surface

The sea surface plays a crucial role in shaping the maritime radio channel, as it is the main interacting object. Due to its rough nature, the sea surface affects signal propagation, depending on factors such as wavelength, wave height, and angle of incidence. Under light to moderate sea conditions, most of the signal energy is scattered in the specular direction. This strong reflection from the sea surface can interfere with the line-of-sight (LoS) component, often causing destructive interference, resulting in significant signal fading at the receiver. However, in rougher sea states, the power of specular reflection decreases and diffuse scattering increases [14].

2.1.2 The Earth

Our planet Earth is a large sphere with a conducting (rough) surface. Consequently, as transmitter and receiver move apart, their LoS connection will eventually be obstructed. Let us call the distance between transmitter and receiver at which this occurs the horizon distance. Despite the LoS blockage, it is well-known that EM waves can still propagate beyond the horizon distance through the diffraction mechanism.

2.1.3 The atmosphere

The free-space path loss equation assumes that EM waves propagate through a vacuum. This assumption works well for short-range systems, but in reality, the atmosphere is a heterogeneous medium, with spatial variations in temperature, pressure, and humidity that affect wave propagation. At larger distances, the

effects of the heterogeneous atmosphere are no longer negligible [15]. One of these effects is refraction. As altitude increases, the refractive index of air decreases due to the falling air pressure, temperature, and relative humidity, causing EM waves to bend downward towards the Earth. A familiar visual example is the sun appearing above the horizon even after it has technically set, because of the bending of sunlight through the atmosphere. This bending can extend the effective range of radio signals because the effect path of the radio signal is located higher above the sea surface, reducing diffraction losses.

The refractivity profile, i.e. the change in refractive index with altitude, varies with weather conditions. Sharper gradients can lead to superrefraction, where waves bend more strongly. If the refractive index decreases very rapidly and this altitude of the superrefractive layer is low enough, waves can become trapped between the sea surface and the superrefractive layer, forming a duct [16]. This phenomenon, known as atmospheric ducting, allows signals to travel far beyond the radio horizon by confining them within a natural waveguide. Ducting can significantly extend the communication range or cause unexpected signal fading.

Another propagation mechanism is tropospheric scattering, or troposcatter [17]. In this case, irregularities in the lower atmosphere scatter part of the signal toward a distant receiver. Although only a small fraction of the signal is captured, this effect can enable communication well beyond LoS. However, troposcatter typically requires high-power transmitters and large, high-gain antennas, making it unsuitable for small or mobile devices. It was widely used before the advent of satellite communications.

Furthermore, hydrometeors such as precipitation and fog significantly impact signal propagation, particularly at frequencies above approximately 5 GHz [18]. Droplets or particles within hydrometeors absorb and scatter EM waves, reducing the signal strength. The degree of attenuation depends on the intensity of the hydrometeor, signal frequency, and path length.

2.1.4 Other

Large objects in the maritime environment with high radar cross sections, such as containerships, islands, and coastal structures, can substantially influence EM wave propagation [19–21]. They cause reflection and scattering of radio signals, producing multipath effects that lead to signal fading. Additionally, these structures can physically obstruct the direct signal path, creating shadow regions where signal strength is severely reduced or completely blocked.

Local scattering effects at the transmit or receive antenna also influence sig-

nal propagation. For example, ships commonly have multiple antennas, radar installations, and other metallic instruments mounted on their superstructures that act as secondary scattering sources.

2.2 Channel Modeling at Sea

2.2.1 Planar two-ray model

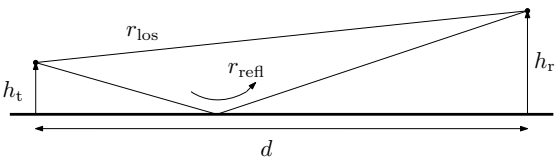

Figure 2.1: Visualization of the two-ray model.

The reflection from the sea surface is taken in account by modeling the path loss by the two-ray ground reflection model [22]. In this section, the planar two-ray ground reflection model is formulated in a general sense by also taking taking account the antenna radiation pattern and the polarization. The goal is to show the approximations that have been made in order to get a simpler two-ray model expression which is used in the papers, and consequently will lead to a better understanding of their limitations. Fig. 2.1 visualizes the two-ray model, a LoS and a reflection component with path lengths r_{los} and r_{refl} can be observed together with the distance d between transmitter and the receiver and their respective antenna heights h_{t} and h_{r}. The full complex-valued model could mathematically be formulated as

$$\begin{aligned}&\frac{\lambda \exp(-\mathrm{j}\frac{2\pi}{\lambda} r_{\text{los}})}{4\pi r_{\text{los}}} \boldsymbol{a}_{\text{r}}^{T}(\phi_{\text{r,los}}, \theta_{\text{r,los}}) \boldsymbol{a}_{\text{t}}(\phi_{\text{t,los}}, \theta_{\text{t,los}}) \\ &+ \frac{\lambda \exp(-\mathrm{j}\frac{2\pi}{\lambda} r_{\text{refl}})}{4\pi r_{\text{refl}}} \boldsymbol{a}_{\text{r}}(\phi_{\text{r,refl}}, \theta_{\text{r,refl}}) \begin{bmatrix} \rho^{\text{VV}} & \rho^{\text{VH}} \\ \rho^{\text{HV}} & \rho^{\text{HH}} \end{bmatrix} \boldsymbol{a}_{\text{t}}(\phi_{\text{t,refl}}, \theta_{\text{t,refl}}),\end{aligned} \tag{2.2.1}$$

where λ is the wavelength, $\boldsymbol{a}_{\text{t}}$ and $\boldsymbol{a}_{\text{r}}$ represent the polarimetric antenna responses of the transmitter and receiver antennas, and ρ is the reflection coefficient where V and H denote the vertical and horizontal polarization, respectively. The angles ϕ and θ are the azimuth and elevation angles of the LoS and reflection path seen from the antennas. Now, several approximations can be made. First, one can assume that $\boldsymbol{a}_{\text{r}}(\phi_{\text{r,los}}, \theta_{\text{r,los}}) \approx \boldsymbol{a}_{\text{r}}(\phi_{\text{r,refl}}, \theta_{\text{r,refl}})$ and $\boldsymbol{a}_{\text{t}}(\phi_{\text{t,los}}, \theta_{\text{t,los}}) \approx \boldsymbol{a}_{\text{t}}(\phi_{\text{t,refl}}, \theta_{\text{t,refl}})$, which is a valid approximation in a typical

maritime scenario as d is much larger than h_t and h_r. The second approximation is that the transmitter and receiver have the same linear polarization. The third approximation is

$$r_\mathrm{refl} - r_\mathrm{los} = \sqrt{d^2 + (h_\mathrm{t} + h_\mathrm{r})^2} - \sqrt{d^2 + (h_\mathrm{t} - h_\mathrm{r})^2} \approx \frac{2h_\mathrm{r}h_\mathrm{t}}{d}, \tag{2.2.2}$$

which is obtained through the Taylor expansion of the square roots. Only after these approximations the two-ray model may be expressed in a more simpler form:

$$\frac{\lambda \exp(-\mathrm{j}\frac{2\pi}{\lambda} r_\mathrm{los})}{4\pi r_\mathrm{los}} \left(1 + \rho \exp \frac{-\mathrm{j}4\pi h_\mathrm{t} h_\mathrm{r}}{\lambda d}\right). \tag{2.2.3}$$

For low grazing angles, the phase of the reflection coefficient is $\angle\rho \approx \pi$ and the amplitude can be close to 1, which applies to both V and H polarization, leading to deep fades when $d = \frac{2h_\mathrm{t}h_\mathrm{r}}{\lambda k}$ with $k \in \mathbb{N}_0$.

The complex reflection coefficient has been modeled as the sum of a coherent component, whose amplitude and phase are deterministic given the two-ray geometry and the sea surface roughness, and an incoherent component whose amplitude and phase are random variables [14]. One could also interpret the coherent and incoherent component as a specular and diffuse component, respectively. For smooth seas the incoherent component can be neglected, while for rough seas it is dominant. Mathematically, a random term can be added the parentheses of (2.2.3), while ρ would then model the coherent reflection. The distribution of this random term is assumed to be zero-mean circularly symmetric complex Gaussian (ZMCSCG) distributed [14]. Another formulation for the incoherent component could evolve from the assumption that the incoherent component is a superposition of a large amount of non-specular reflections from the sea surface, see [20, 23–25]. The next subsection is dedicated to the modeling of the coherent reflection coefficient.

2.2.2 Coherent reflection coefficient

In the domain of radio wave propagation, the scattering of the sea surface has been widely investigated through EM simulations. An overview can be found in [26]. As mentioned in the introduction of this chapter, EM simulations are often not practical. Within the field of channel modeling, asymptotic methods to calculate the coherent reflection coefficient are therefore more popular. Over the years, several methods have been developed to model the coherent reflection coefficient that consider the sea state. Two classes of fast asymptotic methods can be identified. The first one is based on the Kirchhoff approximation, where

the reflection is modeled by the multiplication of the Fresnel reflection coefficient and a roughness factor. This was first done by [27], also known as the "Ament approximation" and similarly by [28], the "Miller-Brown approximation". The simpler Ament approximation can be derived as follows:

$$\rho(\theta) = \rho_0(\theta) \int_{-\infty}^{+\infty} \exp(-\mathrm{j}2k_0 z \sin\theta)\, p_z(z)\, \mathrm{d}z, \tag{2.2.4}$$

where ρ_0 is the Fresnel reflection coefficient, $k_0 = \frac{2\pi}{\lambda}$, θ is the grazing angle of the incident field of the surface, and $p_z(z)$ is the sea surface height distribution. In [27], it was assumed that the height of the sea surface follows a zero-mean Gaussian distribution. For a zero-mean Gaussian distributed height with variance σ_z^2, the integral in (2.2.4) can be solved using the characteristic function of a Gaussian distribution:

$$\rho(\theta) = \rho_0(\theta) \exp\left(-2k_0^2 \sigma_z^2 \sin^2\theta\right). \tag{2.2.5}$$

The Fresnel reflection coefficient can be calculated as a function of the grazing angle θ and the complex relative permittivity ϵ_r:

$$\rho_0^{\mathrm{H}} = \frac{\sin\theta - \sqrt{\epsilon_r - \cos^2\theta}}{\sin\theta + \sqrt{\epsilon_r - \cos^2\theta}} \tag{2.2.6}$$

$$\rho_0^{\mathrm{V}} = \frac{\epsilon_r \sin\theta - \sqrt{\epsilon_r - \cos^2\theta}}{\epsilon_r \sin\theta + \sqrt{\epsilon_r - \cos^2\theta}} \tag{2.2.7}$$

The Ament and Miller-Brown approximations neglect the shadowing effect, i.e. not all points on the rough surface are illuminated. The Ament approximation assumes that the surface height has zero-mean Gaussian distribution, yet when considering the shadowing effect, the height of the illuminate points on a Gaussian surface surface does not follow a zero-mean Gaussian distribution any longer. When taking shadowing into account, the mean of the height distribution will increase and the root-mean-square (RMS) height will decrease. In order to calculate the new height distribution, the RMS slope of the surface is also taken into account. Originally, several works were carried out in [29–31]. More recent work is summarized in [26].

The challenge often lies in correct measurement or estimation of the RMS surface height and slope, which depends on the state of the sea. The parameters of the sea state could be calculated based on a sea surface model, e.g. [32], which is based on the wind speed at 10 m height above the surface. However, it could be more practical to estimate the sea surface parameters from the channel measurement data, which was done in Paper V. By modeling the sea surface

height with a Gaussian distribution with non-zero mean μ_z and variance σ_z^2, we can model the effect of the sea surface roughness including the shadowing effect and have the possibility to estimate them empirically, see Paper V. Then, the solution to (2.2.4) becomes

$$\rho(\theta) = \rho_0(\theta) \exp\left(-\mathrm{j}2k_0\mu_z - 2k_0\sigma_z^2\right) . \tag{2.2.8}$$

The second class of fast asymptotic methods is based on perturbation theory, which can be more suitable for slightly rough surfaces and lower grazing angles, and is known as small perturbation method (SPM), derived first in [33]. Although SPM is more sophisticated, it is not as intuitive and practical as geometric approaches. Approximating the coherent reflection coefficient using the geometric approaches as in (2.2.5) and accounting for the shadowing has been a popular approach for channel modeling and has been supported by measurements as shown in [20, 21, 24, 34].

2.2.3 Extension to round Earth

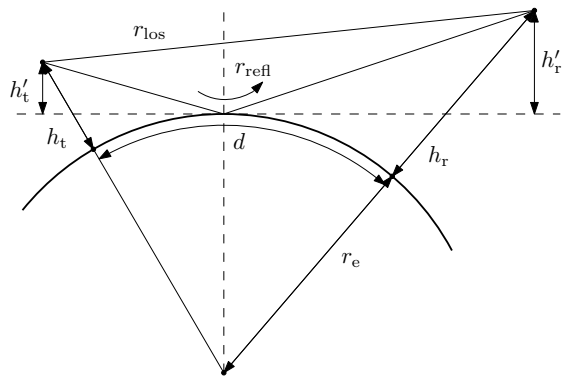

Figure 2.2: Visualization of the round-Earth two-ray model.

The planar two-ray model in Section 2.2.1 is valid when d is small enough so the curvature of the Earth and the atmospheric refraction are negligible. For larger d, they have to be taken into account. First of all, the curvature of the Earth is accounted for by applying the geometry as in Fig. 2.2. Note that r_{e} is not the physical radius of the Earth, but the "effective" radius. This originates from a method developed in [15] to account for atmospheric refraction. The method relies on changing the radius of the Earth to an "effective" radius so the rays can assumed to be straight, while keeping the same propagation distance.

In Fig. 2.2, one can observe that the antenna height has to be adjusted in order to account for the refractivity and the radius of the Earth. Solving the geometry for h'_{t} and h'_{r} given d, h_{t} and h_{r} cannot be done in closed form. Yet, closed-form *approximations* have been derived in the Appendix of Paper I:

$$h'_{\mathrm{t}} = h_{\mathrm{t}} - \frac{1}{2}\left(\frac{h_{\mathrm{t}}}{h_{\mathrm{t}} + h_{\mathrm{r}}}\right)^2 \frac{d^2}{r_{\mathrm{e}}} \tag{2.2.9}$$

$$h'_{\mathrm{r}} = h_{\mathrm{r}} - \frac{1}{2}\left(\frac{h_{\mathrm{r}}}{h_{\mathrm{t}} + h_{\mathrm{r}}}\right)^2 \frac{d^2}{r_{\mathrm{e}}} \tag{2.2.10}$$

From (2.2.9) and (2.2.10), we can notice that the modified antenna heights are approaching the true antenna heights as d gets small or r_{e} gets large. A typical value for r_{e} is 8500 km [15].

2.2.4 Diffraction loss

The general solution for calculating the propagation loss along a sphere consists of an infinite series with Airy functions [35]. The challenging part was computing this series numerically, at least back in the 50s. Therefore, many researchers have addressed the numerical challenges; an example is [36].

In the so-called "multipath region", where the distance is small, the two-ray model can provide an accurate approximation without high computational cost. In the diffraction region, far beyond the horizon distance, only a small number of terms are needed [36]. In the intermediate region, more terms are needed.

Several other diffraction loss models, such as [37–39], have been used in the recent literature for maritime channel modeling. The question that arises is when to use the "ray-based" two-ray model and the "wave-based" diffraction model. The distance where 60% of the First Fresnel Zone is occupied by the Earth is used in [21] to address this issue, while this method is a rule of thumb and could be subject to errors. This distance d_{60} can be expressed as [40]

$$d_{60} = \frac{159.49 f_{\mathrm{GHz}} h_{\mathrm{t}} h_{\mathrm{r}} (\sqrt{h_{\mathrm{t}}} + \sqrt{h_{\mathrm{r}}})}{0.0389 f_{\mathrm{GHz}} h_{\mathrm{t}} h_{\mathrm{r}} + 4.1(\sqrt{h_{\mathrm{t}}} + \sqrt{h_{\mathrm{r}}})}, \tag{2.2.11}$$

where f_{GHz} is the carrier frequency in GHz. Based on the original source of the diffraction model [37], the total reflection coefficient should also be set to zero to avoid mixing of the models, which is not clearly stated or considered in [21]. A decent fit with the measurements is still achieved because of the divergence factor and shadowing factor, which decreases the total reflection coefficient as the distance is increased, indirectly setting it to zero at large distances.

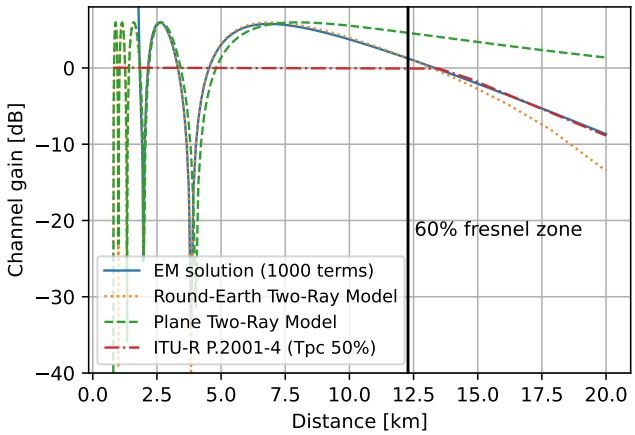

Figure 2.3: Different diffraction loss models and two-ray models at 6 GHz for $h_\mathrm{t} = h_\mathrm{r} = 10\,\mathrm{m}$ and $\rho = -0.99$. The channel gain is relative to free space propagation.

In Fig. 2.3, the EM solution is compared to the planar and round two-ray model and to the ITU-R P.2001-4 model [39]. On the left-hand side of the figure the deep fading dips of the two-ray model can be observed. Here, the EM solution does not have enough terms to model to the first interference lobes but agrees well with a round and planar two-ray model in the fourth interference lobe. The ITU-R model does not account for the two-ray interference lobes, while it does take the diffraction loss into account. One can see a discontinuity of the ITU-R model at 13 km. This is the point where the path loss drops below the free space loss. From the figure, we can also observe that the round-Earth two-ray model can also model the path loss reasonably well, even until a bit after the 60% Fresnel zone distance. At 20 km we can conclude that only the EM solution and the ITU-R model agree with each other. The planar two-ray model underestimates the path loss, while the round two-ray model overestimates it.

Note that in addition to diffraction, the ITU-R model also considers ducting, troposcatter, and sporadic-E. For the parameters in Fig. 2.3, the predicted path loss of these mechanisms is negligible compared to the path loss through diffraction.

2.2.5 Fading

The fading due to the coherent sea surface reflection could be interpreted as large-scale fading, as the fading changes very little when moving the transmitter or receiver over a few wavelengths. This is generally the case when changing the

position in the horizontal direction, while movement in the vertical direction can have significantly greater impact on the signal strength according to the two-ray model. Large-scale fading in a generic scenario and environment is caused by shadowing, where the signal is partially blocked by a large object, while still diffracting around the obstruction. As discussed before, this can also happen in a maritime scenario, as, for example, other vessels, islands, or buildings in the vicinity of the base station can block LoS between a vessel and the base station. In [41], a path loss model was developed for in-harbor LoS and non line-of-sight (NLoS) environments.

As discussed in a brief discussion above, small-scale fading can be caused by vertical movement of the antenna, hence the vertical movement of an antenna on a vessel due to the dynamic sea surface can cause fading [25]. The fading can also result from diffuse scattering from the sea surface or local scattering at the transmitter or receiver. The fading distribution has been investigated in several works by fitting well-known distributions in the literature [21, 24, 41, 42]. The results of these works show that a Rician distribution is a suitable fading distribution. A fading distribution was proposed in [25] taking into account both the transmitter height movement and geometry-based stochastic channel models (GSCMs) have also been developed for the maritime environments [20, 43–45].

Chapter 3

Channel Sounding

In the design and evaluation of wireless systems, real-world measurements of the wireless propagation channel are essential [12]. The process of measuring the wireless channel is commonly referred to as channel sounding. In this thesis, several measurements have been performed using the channel sounder of which the design is presented in Paper III. The motivation for creating this channel sounder was the absence of an existing solution that supported distributed antenna systems and was portable enough to be transported to the sea and take measurements in a single day. Furthermore, due to other ongoing research interests within the research group, the sounder was designed with 6G research in mind, supporting applications such as distributed MIMO (D-MIMO) and integrated sensing and communication (ISAC). This chapter is dedicated to channel sounding and, in particular, the design of the channel sounder, as a significant portion of the thesis work was devoted to its development.

3.1 Introduction

3.1.1 Sounding principle

The transmitter side of the channel sounder sends out a known waveform, which is then received at the receiver end of the channel sounder. By analyzing the changes of the received waveform compared to the transmitted waveform, the impulse response of the channel can be identified. In the time domain, the estimated channel impulse response can be mathematically expressed as [12]:

$$\hat{h}(t,\tau) = h(t,\tau) * g_{\mathrm{RX}}(\tau) * g_{\mathrm{TX}}(\tau) \tag{3.1.1}$$

where $h(t, \tau)$ is the time-variant impulse response of the propagation channel, $g_{\mathrm{RX}}(\tau)$ is the receiver filter impulse response, and $g_{\mathrm{TX}}(\tau)$ is the transmitted waveform. In a channel sounder, we have control over $g_{\mathrm{RX}}(\tau)$ and $g_{\mathrm{TX}}(\tau)$. In an ideal case, $g_{\mathrm{RX}}(\tau) * g_{\mathrm{TX}}(\tau)$ is a Dirac pulse, then $\hat{h}(t, \tau) = h(t, \tau)$, assuming that there is no noise in the system. However, a Dirac pulse does not exist in reality because the bandwidth of a channel sounder cannot be infinite.

3.1.2 What is "the channel"?

In measuring the channel, it is important to establish what is "the channel" to be characterized. Depending on the intended use of the channel measurement data, different channels can be defined. Without calibration, the measured channel contains contributions of the hardware components of the channel sounder, the response of the cables, and the response of the antennas. In the context of channel sounding, calibration is the process of removing an undesired effect on the channel measurement. For example, the response of the hardware components is often not desired and is removed through a process a calibration process, which will be described more in detail later on. However, removing the antenna response is more challenging because it depends on the angle-of-arrival (AoA) of the signal, which is often not known and has to be estimated. In some cases, the antennas are therefore considered part of the wireless propagation channel.

3.1.3 Dimensionality

The channel can be measured in three dimensions: time, frequency, and space. While time and frequency are non-ambiguous, the spatial dimension can be interpreted as the antenna domain in case of multiple antennas at the transmitter and/or receiver, i.e. a MIMO channel, or as the position of an antenna in space. Together with the sounding waveform, the type of antenna and their geometrical configuration fundamentally determine how the channel is excited and how accurate it can be measured and characterized in the respective domains. Typically, the channel sounder configuration and the measurement scenario resemble a real-world application of a wireless system. Naturally, as the targeted systems become more complex, e.g. higher bandwidth, higher frequency, more antennas, so do the channel sounders gain complexity.

3.1.4 Connection to channel modeling

On the other hand, the configuration and requirements of the channel sounder can be subject to the targeted channel models. One of the most popular ways of modeling a wideband channel is by a superposition of multipath components (MPCs). In its most basic format, each component has a delay and a complex amplitude. In channel modeling, the parameters of those MPCs can be characterized in various ways. The angle-of-departure (AoD) and the AoA of the MPC, and the Doppler frequency can also be included.

Estimating those parameters can be a daunting task, as it requires calibration and specialized high-resolution estimation algorithms. Nevertheless, the accuracy ultimately depends on the choice sounding waveform, the antenna design, and the spatial configuration of the antennas. Therefore, some channel sounders, e.g. [46], have a much higher number of antennas and a larger bandwidth than the targeted wireless system, since the goal is to get a better estimate of the parameters MPC, leading to a better characterization of the wireless channel.

3.1.5 Latest trends

Naturally, the latest research trends affect the requirements and design of new channel sounders [47]. At the time of writing, 6G research is ongoing and 6G standardization is starting. When 5G was being developed, there was an interest in increasing the number of antennas by an order of magnitude, i.e. massive MIMO, leading to the development of new channel sounders. Although for 5G the antennas were co-located, for 6G a huge number of distributed antennas is considered. Due to the distributed locations of the antennas, the channel in between the base station's own antennas also becomes interesting because it contains information about the environment. This information about the environment, also embedded in the classical base station user channel, can be used to to perform "sensing", which is referred to as ISAC or joint communication and sensing (JCAS). For example, one could detect a person in the room, without the person carrying any kind of transmitter. From a channel sounder point of view, the channel between all distributed antennas must be measured in order to test and develop multi-static sensing techniques, which is an aspect that has been addressed in the channel sounder design in Paper III.

Other trends driving new channel sounder developments are new frequency bands and higher bandwidth. Those two properties are often quite connected, as there is more bandwidth available in the higher frequency bands. For 6G, Fre-

quency Range 3 (FR3) is considered, which ranges from 7.125 GHz to 24.25 GHz.

3.2 Channel Sounder Requirements and Constraints

As in the design and implementation of any measurement instrument, there must be target specifications or requirements. For channel sounders, we can categorize the requirements in the same three domains as mentioned above: time, frequency, and space. We also introduce one additional domain: the "practical domain".

3.2.1 Time domain

The requirement in the time domain of the channel sounder relates to how often the channel needs to be measured over time. We refer to the "snapshot rate" or the "repetition period" as the corresponding system parameter. Its requirements depends on how fast the channel is changing. For example, in a channel measurement between two driving cars, the channel changes very quickly. Formally, the requirement for the snapshot rate can be formulated using the sampling theorem as a function of the maximum Doppler frequency $\nu_{\max}$ in the channel [12], which gives:

$$f_{\text{rep}} \geq 2\nu_{\max}. \tag{3.2.1}$$

The Doppler frequency can, in some cases, be estimated within a single snapshot if the waveform is long enough. Then, the maximum Doppler frequency the sounder can observe is much higher than given by (3.2.1). The maximum Doppler that can be observed in the channel can be predicted based on the moving speed of the antennas and objects in the environment. The f_{rep} of the channel sounder cannot be infinitely large as the repetition time $T_{\text{rep}} = 1/f_{\text{rep}}$ should be larger than excess delay of the channel to avoid aliasing [12].

From an MPC estimation point of view, the duration of the snapshot also matters because one has to assume that within this period of time the MPC parameters are constant. The snapshot rate can be derived on the basis of the rate at which the MPC parameters are expected to change. The Doppler could be integrated into the signal model and estimated [46]. Hence, the snapshot rate can be much lower than given in (3.2.1). However, if one wants to track the phase of the MPC over time without ambiguities, the snapshot rate must be more than twice the maximum Doppler frequency in the channel, as discussed in the first paragraph of this section.

3.2.2 Frequency and delay domain

In the frequency domain, there is only one requirement: the bandwidth. Considering that the channel is a superposition of MPCs, the bandwidth positively affects the accuracy and resolution of the MPC delay estimates. Intuitively, this could be understood from a system-theoretic perspective. When a bandwidth-limited system is excited with a Dirac pulse, and assuming that the individual responses of the MPCs are frequency flat, the received signal will be a superposition of scaled and time-shifted sinc pulses. The width of the pulses are inversely proportional to the bandwidth. The higher the bandwidth, the narrower the pulses, and the more sinc pulses that can be distinguished from each other. The accuracy is related to the second-order derivative, or the "roundness" at the peak of the received pulse. A typical rule-of-thumb is that it is possible to resolve multipath with a delay difference which is larger than inverse bandwidth. Note that with high-resolution parameter estimation, the resolution can be much higher. Higher bandwidth can also lead to better suppression of narrowband interference.

Channel sounders are typically limited in bandwidth due to spectrum regulations, i.e. the bandwidth is rather a constraint than a requirement. Often, the bandwidth of the channel sounder is the same as that of the targeted communication system, as spectrum licenses can be obtained for research purposes. From a research point of view, a higher bandwidth can give more insight in the performance of radio-based localization and sensing, addressing questions such as how much bandwidth we actually need. The channel sounder in Paper III is designed to operate in the license-free 5 GHz band as it is the only sub-6 GHz frequency band where it is allowed to transmit with a bandwidth of 400 MHz and with a transmit power of 14 dBm, which is much higher than the transmit power allowed in the ultrawideband (UWB) bands.

3.2.3 Space domain

The requirements in the spatial domain are the amount of transmit and/or receive antennas and the antenna pattern of the antennas or the antenna array as a whole. With a similar intuition as in the frequency domain, the angular resolution and accuracy will increase with the aperture of the antenna array, with is a combination of the number of antennas, the spacing in between them, and the design of the antennas. Note that high spatial resolution might not be needed as a high bandwidth can also provide sufficient resolution. In order to perform directional characterization of the channel, phase-synchronous reception and/or

transmission is also required.

3.2.4 Practical domain

A channel sounder can have many practical requirements and constraints. The first requirement for channel sounding is the (dynamic) range of the channel sounder. To calculate the range of the channel sounder, one already needs some sort of path loss model and an signal-to-noise ratio (SNR) that is required at that range in order to get a meaningful channel measurement. The simplest channel model would be the free space model, and a typical SNR would be 20 dB, according to the author.

The second practical requirement is the transportability of the channel sounder, which numerically translates into the weight and size of the channel sounder. On the one hand, this can be essential in conducting measurements outside the typical laboratory environment, reducing the amount of time and effort to transport and set up the channel sounder. On the other hand, the channel sounder might be installed on a vehicle, robot, or in this doctoral thesis: on a sailboat. The size and weight of the channel sounder can make the difference in the feasibility of the planned measurement and its scenario. Aspects such as vibration and precipitation should also be taken into account.

The third requirement is rather a constraint than a requirement: the rate of the data being produced by the channel sounder. A channel sounder generally saves the channel measurement to a solid state drive (SSD) and the rate of the data produced by the channel sounder is constrained by the sustained write speed of the SSD.

Time and frequency synchronization between the transmitter and receiver side of the channel sounder is essential for accurate channel measurements and correct operation of the channel sounder. For example, time or frequency offsets can mistakenly be interpreted as part of the channel, while they are originating from synchronization errors. With time synchronization, it is meant that the transmitter and the receiver have the same perception of time relative to a common reference. With frequency synchronization, both ends have the same rate at which the time changes. Since no synchronization solutions are perfect, it is essential to establish what kind of time and frequency accuracy can be allowed. Absolute phase synchronization of the transmitter and receiver is, while possible, often not a target. Phase synchronization or coherency between the antennas at either the transmitter or receiver side is required to do directional characterization of the propagation channel.

In the overall design and implementation of a channel sounder, the biggest constraint is the state-of-the-art of the hardware components. However, these components can be far out of the budget of a research project. Therefore, cost and development time are generally the biggest constraints. In the next section, it will become clear that many of the design strategies are related to cost.

3.3 Channel Sounder Design and Implementation

3.3.1 Hardware platforms

The first step in designing and implementing a channel sounder is to choose an appropriate hardware platform. This platform acts as the interface between the digital world, where sounding waveforms are generated and channel measurement data are collected, and the radio frequency (RF) domain, where signals are transmitted and receiver. The hardware platform is chosen on the basis of the targeted performance, available time, and budget. In the following, we introduce four main types of hardware platforms.

Vector network analyzer

A vector network analyzer (VNA) is a specialized instrument used to measure the electrical characteristics of RF networks, but it can also be employed to measure radio channels, e.g. [48]. Due to its design, it can easily span several GHz of bandwidth, while the achievable snapshot rate is much lower than other platforms because of its inherently different design. A VNA sweeps over the frequency domain, while other platforms directly sample the time domain. On the other hand, VNAs can deliver high accuracy because they are designed as measurement instruments and include well-developed calibration procedures.

Software-defined radio

Software-defined radios (SDRs) have become increasingly popular in recent years because RF hardware components have become smaller and more affordable. Numerous examples of channel sounders based on SDRs can be found in [49–54]. The principle behind SDR is that all signal processing is developed in software and executed on the central-processing unit (CPU) of a host computer. SDRs

typically contain an analog front-end, an up-and-down converter, a data converter, and an field-programmable gate array (FPGA) responsible for streaming the RF samples effectively to the host computer. SDRs are very popular for channel sounding as they offer full flexibility in a cost-effective package.

Wireless testbeds or cellular base stations

Wireless systems that were not originally designed for channel sounding, such as wireless testbeds or base stations, can also be used as a channel sounder or can be modified to output the channel response [55–57]. The major advantage of using testbeds or base stations is that they measure very representable propagation scenarios. However, these systems might not be able to perform directional characterization of the channel due to the lack of phase synchronization at the antenna ports, which is not strictly required for wireless communications.

Custom platforms

Custom-built platforms can offer ultimate flexibility for designing and implementing a channel sounder [58–61]. All components of the radio system, from the antenna to the data converter and the FPGA, can be tailored to the requirements. Nevertheless, this flexibility can come with a considerable cost, both in terms of development time and money.

Our channel sounder

The channel sounder presented in Paper III is based on the SDR platform, specifically the NI universal software radio peripheral (USRP). The X410 model was used in Paper III. The choice is motivated by the high flexibility and performance of the SDR and the available software packages that shorten the development time. The USRP platform comes with software packages, the USRP hardware driver (UHD) and the RF Network-on-Chip (RFNoC) [62], which makes it more convenient to build custom applications such as channel sounding. In Paper III, we have also shown that it is possible to do real-time averaging on the FPGA, lowering the data rate requirements for the interface between the SDR and the host computer while increasing the SNR.

3.3.2 Sounding waveform

The design of the sounding waveform is considered as part of the design of the channel sounder. First, the sounding waveform needs to have a large bandwidth

and a uniform power spectral density in order to equally excite the channel across the whole frequency range. In the time domain, the waveform can be long to achieve a high energy but cannot be longer than the repetition time, as discussed in the previous section. A good peak-to-average power ratio (PAPR) of the channel sounding waveform is also beneficial in terms of energy-efficient use of the power amplifier (PA) at the transmitter. Good autocorrelation properties are also desired as it makes it easier to distinguish the different multipath in the delay domain.

An approach that has been used in Paper III and [46] is to use a waveform similar to an orthogonal frequency-division multiplexing (OFDM) waveform. Such a waveform $x(n) \in \mathbb{C}$ with a length of L samples, can in discrete complex baseband be expressed as

$$x(n) = \frac{1}{L} \sum_{k=0}^{L-1} X(k) \exp\left(\mathrm{j}2\pi kn/L\right), \tag{3.3.1}$$

where $X(k)$ is the complex amplitude of the k-th frequency tone. This approach is more convenient in post-processing and computationally efficient due to fast Fourier transform (FFT). The sampled channel impulse response can be calculated with an :

$$h(n) = \mathrm{IDFT}\{\frac{Y(k)}{X(k)}\}. \tag{3.3.2}$$

where $Y(k)$ is the discrete Fourier transform (DFT) of $y(n)$. For (3.3.2) to be valid, $y(n)$ must be the result of a circular convolution of $h(n)$ and $x(n)$, unless $h(n)$ is a Dirac pulse. In OFDM-based systems, this is resolved by using a cyclic prefix. A similar solution has been used in Paper III, where multiple copies of $x(n)$ are sent and the receiver only starts after P samples, which could be regarded as removing the cyclic prefix. Then, the multiple copies of the sounding waveform are averaged on the FPGA of the USRP. For $X(k)$, a Zadoff-Chu sequence was chosen for a continuous block within $X(k)$ and zero-padded where necessary to adapt the bandwidth of the sounding waveform relative to the sample rate, which was larger than the supported RF bandwidth of the USRP. The choice for the Zadoff-Chu sequence is motivated by its excellent PAPR and autocorrelation properties, whether it is generated directly in the time domain or through a discrete Fourier transform as described above. The Zadoff-Chu sequence is a periodic continuous-phase signal, which keeps the PAPR low when stitching several waveforms together in the time domain.

3.3.3 Antenna system

Increasing the number of antennas in a channel sounder can be done in several ways as described in the following paragraphs.

Parallel

Parallel transceiver chains, i.e. there is one transmitter and/or receiver chain per antenna, are used in channel sounders that need to measure the channel very swiftly, e.g. in a couple of milliseconds [50–54, 59, 60, 63–66]. However, the cost of the channel sounder scales with the number of antennas. In addition, there is a risk that the channel sounder becomes impractical in size and energy consumption. It can also be challenging to perform phase calibration of transceiver chains, which is needed for AoA and AoD because it is based on the phase difference between antennas.

Switched

Channel sounders that employ RF switches to switch between different antenna elements in an array can address some of the drawbacks of parallel transceiver chains, such as cost and phase calibration [48, 59, 61, 67, 68]. Nevertheless, more time is required to switch through all antennas, making the channel sounder less suitable for highly dynamic channel measurements. Another disadvantage is that RF switches introduce losses, resulting in a lower SNR compared to an equivalent parallel antenna system.

Virtual

A virtual antenna array can also be used to measure the spatial dimension of the channel [48, 61, 67, 68] and follows the same principle as synthetic aperture radar (SAR). In this technique, an antenna or antenna array is moved every snapshot in order to measure the channel with a "virtual" antenna array, of which the number of antennas can be extremely large. Inherently, only static channels can be measured as it involves moving antennas every snapshot.

Hybrid

Parallel and switched methodologies can be combined to establish a trade-off between cost and dynamic capability. This approach was chosen in Paper III. Moreover, in this paper, an antenna array of 2×4 dual-polarized antennas were

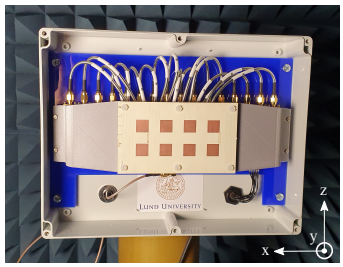

Figure 3.1: Photograph of one panel inside an anechoic chamber.

integrated with the RF switch in a "panel" as shown in Fig. 3.1. In this way, the antenna radiation pattern can be conveniently measured in an anechoic chamber. By measuring the antenna pattern together with the RF switch, the phase differences between the antenna elements induced by the RF switch are also measured, enabling angular estimation. In total, eight panels are used in the channel sounder, where each panel is connected to a separate RF chain. Compared with a fully switched channel sounder, the channel can be measured eight times faster.

3.3.4 Synchronization

As discussed in the previous section, time and frequency synchronization between the transmitter and receiver side of the channel sounder is essential. RF instruments such as VNAs, signal generators, and spectrum analyzers utilize two standardized signals, transmitted over coaxial cables, to synchronize several instruments in time and frequency: a pulse or trigger signal for time synchronization and a 10 MHz sinusoidal signal for frequency synchronization. The same "standard" has also been used for synchronization in channel sounders. The trigger signal can be used to trigger a measurement, while the 10 MHz signal ensures the synchronized sample and carrier frequencies. As mentioned before, the pulse and 10 MHz signals are transmitted over cables. For a channel sounding, this can be very impractical as the transmitter and/or receiver can be moved during a channel measurement. For outdoor measurements, a GNSS receiver can be employed for time and frequency synchronization. A GNSS receiver outputs two signals: a 10 MHz and a 1 pulse-per-second (1PPS) signal. The 1PPS signal is a pulse that repeats every second. The flank of the pulse is aligned with a whole second of the coordinated universal time (UTC). The 1PPS cannot be used directly to start a measurement as there is a one-second ambiguity. The 1PPS signal should be used together with the UTC timestamp received by the GNSS receiver to achieve absolute time synchronization. The transmitter and

the receiver can then be started at a pre-determined start time. Note that synchronization over GNSS has limitations in terms of time and frequency accuracy. For example, the Global Positioning System (GPS) receiver in USRP X410 has a timing accuracy of 8 ns RMS and a frequency accuracy of 1 ppb. For indoor measurements where the transmitter and receiver cannot be connected with cables, or for outdoor measurements where a higher level of synchronization is required, atomic clocks can be used, e.g. rubidium clocks. These clocks have an extremely high frequency stability. Commercial rubidium clocks such as the Stanford Research FS725 output a 10 MHz and 1PPS signal and have 1PPS input signal. An atomic clock can be deployed on both the transmitter and receiver side. Before a measurement, they are connected via a 1PPS signal and accurately synchronized in time and frequency. In practice, this process can take several hours before the clocks are sufficiently synchronized. The one-second ambiguity can be addressed by synchronizing the transmitter and receiver with UTC time via the local area network (LAN) to a network time protocol (NTP) sever. Hence, communication between the transmitter is necessary to communicate the start time.

The channel sounder in Paper III supports synchronization via 1PPS and 10 MHz signals, which are derived from an external rubidium clock or from the built-in GPS receiver of the USRP X410. For measurements at sea in Paper II, Paper IV and Paper V, a GPS-disciplined rubidium clock was used on the receiver side, while on the transmitter side only the built-in GPS receiver was used. In order for the transmitter and receiver to start at the same time, the start time must be communicated: there is a need for a wireless backhaul link. Nevertheless, such a link can interfere with the measurement or can be unreliable, definitely at a large distance such as at sea. To avoid any kind of communication between the transmitters, the total transmitted waveform during one second is always periodic with one second. This means that the transmitter sends signals based on the 1PPS signal but does not necessarily know the absolute time. At the receiver(s), the received waveforms are time-stamped with the absolute time.

Our channel sounder does not support phase synchronization or phase coherency, neither between the transmitter and the receiver, nor between different RF chains within one USRP. In this context, phase synchronization means that all RF chains in the sounder have the same phase reference. Phase coherency means that the RF chains in the channel sounder have a different phase reference, but this difference is constant over several channel measurements. The RF chains are phase-coherent within one channel measurement as the USRPs and RF chains have the same frequency reference. Phase coherency (over several

measurements) is achieved within one panel due to the RF switch, as discussed before. Phase coherency between RF chains in several measurements is very challenging and requires careful design of the hardware components of the channel sounder and specialized expertise in hardware design. As an alternative, phase references between the RF chains within one channel measurement can be estimated over-the-air (OTA), which has been done in Paper V.

3.3.5 Real-time processing

The data produced by the channel sounder can be very large. For example, a single RF chain that samples the baseband signal at a sample rate of 500 Msps with 32 bits per sample produces 2 GB/s of data. Saving all data continuously to a modern harddrive is very challenging. To address this issue, real-time processing was implemented on the channel sounder in Paper III. The real-time processing included selecting the right time slots to receive the sounding waveforms and averaging them to get a higher signal-to-noise ratio. The main drawback is that it limits the sounder in the maximum absolute Doppler frequency. The RFNoC framework was used to implement sample selection and waveform averaging on the FPGA.

3.4 Metadata

Channel sounding goes beyond simply measuring the propagation channel; it could also involve collecting valuable metadata that enhance the understanding of the measurement environment, such as the position and orientation of the antennas. In addition, the configuration of the channel sounder used, such as amplifier gain settings or software version, helps ensure reliable and reproducible measurements.

To capture the ground truth of the position and orientation of the antennas, several systems can be used. For outdoor measurements, GNSS is used and meter-level position accuracy can be achieved. If more accuracy is needed, real time kinematics (RTK) is used. RTK relies on the carrier phase information of the GNSS signals to obtain centimeter-level accuracy. The orientation of an antenna can be captured using an inertial measurement unit (IMU).

In indoor environments, the position could be determined with a camera-based ground truth system [69]. In these kinds of systems, multiple cameras are required and LoS connections between the antenna and the cameras are essential for reliable position estimates. An alternative positioning technique involves a

lidar that is installed on the same platform as one of the antennas. Using a simultaneous localization and mapping (SLAM) algorithm, the position of the lidar can be estimated within an environment and the surrounding structures can be captured [53]. Reflective tape can also be attached to objects in the environment that need tracking, such as other antennas in the system. This approach has been used in Paper III to localize the panels.

In our channel sounder, the measurement data are first stored in a raw binary format and the sounder metadata are stored in a JSON file. A customized script converts the raw measurement data and the sounder metadata together into the Zarr dataformat. The Zarr file can then be read and used for processing using the xarray Python package. Other metadata are also converted into the Zarr format and are synchronized with sounder data using UTC time stamps.

3.5 Calibration

Calibration is a central part of channel sounding since the measurement of "the channel" can contain undesired contributions of the hardware components of the sounder such as cables or amplifiers. To remove those contributions, they have to be known or measured. This is generally done through a process called "back-to-back" calibration. The transmitter and receiver antenna ports are connected to an attenuator of which the response H_{att} is measured using a VNA. If we represent the channel in complex baseband in the discrete frequency domain, then the calibrated channel response H_{cal} can be calculated by dividing the uncalibrated channel response H_{uncal} by the back-to-back channel response H_{b2b}:

$$H_{\text{cal}}(k) = \frac{H_{\text{uncal}}(k) H_{\text{att}}(k)}{H_{\text{b2b}}(k)}. \tag{3.5.1}$$

From the back-to-back measurement, potential synchronization problems can also be detected such as a carrier frequency offset (CFO) because the back-to-back channel is effectively static. An observed frequency offset during the back-to-back calibration can only come from the channel sounder and not from the channel.

If the goal is to estimate AoA or AoD, for example, as part of high-resolution multipath parameter estimation algorithms [70, 71], the radiation pattern of the antenna array must be measured in addition to the back-to-back channel response. In a switched-type channel sounder, the response of the array is measured together with the RF switch to also take the phase and amplitude difference between the antenna elements induced by the switch.

Chapter 4

Applications with Multiple Antennas at Sea

Introducing multiple antennas at the transmitter and/or receiver in a wireless communication system opens up a new dimension of the channel: the spatial dimension. Multiple antennas can be exploited for both communication and positioning purposes, which are introduced in the following sections, with a focus on fading mitigation (Paper I, Paper IV) and ranging (Paper V).

4.1 Maritime Communication Systems

4.1.1 Beamforming

One of the primary advantages of employing multiple antennas in wireless communication systems is the ability to perform beamforming. Beamforming enables dynamic steering of the transmitted or received signal in a specific direction, thereby increasing the directivity of the communication link. This technique can be applied at both the transmitter and the receiver and significantly improves the SNR, realizing array gain [72]. An enhanced SNR directly results in an increased channel capacity or improved energy efficiency, as radiated energy is focused where it is needed rather than being widely dispersed. This is particularly critical in maritime scenarios, where vessels are often located several kilometers offshore. In such environments, every decibel of gain is valuable. For example, an SNR improvement of 6 dB can potentially double the communication range. Beamforming also reduces the impact of interference from unwanted sources, particularly when the interferer lies outside the main lobe of the beam,

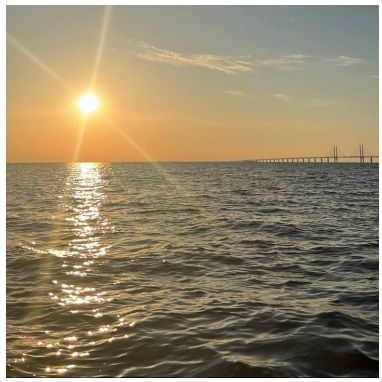

Figure 4.1: Narrow strip of sea surface scattering of sunlight.

as the array can spatially filter out signals arriving from other directions.

4.1.2 Fading mitigation

A second major benefit of using multiple antennas is the ability to mitigate fading. As described previously, fading caused by coherent sea surface reflections can be modeled using the two-ray propagation model. The distances at which deep fading occurs depend strongly on the heights of the transmitting and receiving antennas above sea level. Consequently, one antenna may experience a deep fade due to destructive interference, while an antenna at another height. The effectiveness of spatial diversity, therefore, hinges on the spacing between antennas. Closely spaced antennas will experience highly correlated fading. This was a central consideration in Paper I and Paper IV, which investigate antenna configuration, spacing and the required number of antennas to improve link reliability.

To assess the potential benefits of spatial diversity in broader terms, the angular power spectrum can be examined because it relates to spatial correlation. In the azimuth domain, open-sea environments tend to exhibit sparse scattering as a result of the limited number of surrounding objects. However, it is hypothesized that the elevation domain may show a larger angular spread, particularly due to scattering from the sea surface. This hypothesis is supported by observations of specular sea surface scattering during sunset, where a narrow vertical strip of reflected light becomes visible (see Fig. 4.1). The elevation domain is also critical when considering height-sensitive phenomena such as ducting and tropospheric scattering. For these reasons, in this thesis, particular emphasis is placed on exploring spatial correlation in the vertical domain, which is of unique

Figure 4.2: Vertical antenna array used during the experiments.

significance in maritime communication.

Several measurement campaigns were conducted to investigate vertical spatial correlation. Initial experiments involved fixed-height antenna measurements over the sea surface between two jetties. However, the temporal fading observed in this configuration was minimal, primarily due to low wave heights (2–3λ), and the diffuse component was approximately 40 dB weaker than the LoS component signal strength. In such cases, fading is negligible for typical wireless systems, where the required SNR is usually much lower. For this reason, these measurement data were not published. To observe more significant fading effects and their spatial correlation, measurements were later conducted in open water between a transmitter mounted on a sailboat and a large vertical antenna array on land with 64 dual-polarized antenna elements, which is depicted in Fig. 4.2. Although this approach introduced greater signal variation, it also presented new challenges. In particular, the vertical movement of the boat induced fading, as discussed in the previous section. Efforts were made to isolate the fading due to the transmit antenna height variations from fading due to diffuse scattering by estimating the transmitter's vertical position and subtracting the modeled response. In theory, such separation is feasible, but it requires highly accurate knowledge of both the antenna height and the sea surface reflection coefficient.

Ultimately, the fading caused by diffuse scattering was either too weak to be reliably measured or masked by dominant effects of the vertical movement. In the absence of usable measurement data to analyze the incoherent component and its spatial correlation, the quasi-deterministic nature of the maritime channel was instead exploited for ranging applications, as demonstrated and analyzed in Paper V.

4.1.3 Spatial multiplexing

A third major advantage of multiple antenna systems is the potential for spatial multiplexing. In a single-user multiple-input multiple-output (SU-MIMO) application, this capability depends on the number of independent propagation paths that the signal can travel from the transmitter to the receiver, with the possibility of increasing channel capacity proportionally to the number of available antennas. In a simplified open-sea environment without scatterers other than the sea surface, there are primarily two propagation paths: the LoS path and the sea surface reflection. Additionally, dual-polarized antennas could theoretically double the amount of spatial streams to four. However, in practice, the LoS and reflected components often cannot be separated at large distances. Nevertheless, it may still be feasible to achieve two spatial streams by exploiting the orthogonal polarizations, assuming minimal cross-polarization in the sea surface reflection.

In practical maritime scenarios, multi-user multiple-input multiple-output (MU-MIMO) may be more relevant than SU-MIMO. In such systems, multiple vessels within the base station coverage area can be served simultaneously, provided that they can be sufficiently spatially separated. The degree of separation required depends on the aperture and resolution of the antenna array of the base station. In these scenarios, spatial separation between users can be leveraged to enhance spectral efficiency, allowing for effective use of multiple antennas even in the absence of rich scattering environments.

4.2 Radio-based Positioning

Radio-based positioning refers to the use of wireless signals to determine the location of a device. This technology is widely applied in navigation, tracking systems and location-based services, with GNSS being a well-known example. The core principle involves measuring specific characteristics of radio signals, such as signal strength, time-of-arrival (ToA), or AoA, to estimate the position of a receiver or transmitter. Although GNSS is extremely popular and effective

for outdoor positioning, it has several limitations. It generally depends on a clear LoS to satellites, making it unreliable or unusable indoors. GNSS signals are also vulnerable to interference, jamming, and spoofing [7]. These drawbacks highlight the need for backup systems, especially as we move toward greater reliance on positioning technologies, for instance, in autonomous shipping. An attractive alternative is to leverage the existing communication infrastructure for positioning [73]. Prevalent radio-based positioning techniques include multilateration, triangulation, fingerprinting [74], multipath-based SLAM [75, 76]. In the following subsection, multilateration is introduced, as it is the positioning technique that is used together with the ranging technique developed in Paper V.

4.2.1 Multilateration

Multilateration is a technique to estimate the position of a device using distance measurements from at least three known reference points, commonly referred to as "anchors". A visual way to understand multilateration is by drawing virtual circles around each anchor. The point where all these circles intersect is then the estimated position of the device.

The process of obtaining these distance measurements is commonly known as ranging. Range estimates typically rely on time-based methods that measure signal propagation delay or time-of-flight (ToF), including one-way ToA, two-way ToA, and time-difference-of-arrival (TDoA) techniques [77]. One-way TOA demands precise time synchronization between user and base stations, which can be a significant technical challenge. In two-way ToA ranging, the distance is calculated based on the round-trip signal time. This eliminates the need for a common time reference, but is still limited by the relative drift of the oscillator frequency [77]. Two-ray ranging also needs at least two transmissions, one for the device and one for the base station, requiring more spectrum resources and therefore limiting scalability. TDoA removes the requirement for synchronization between the user and the base stations, but it still needs precise timing synchronization between the base stations themselves in order to correctly calculate the TDoA.

Multilateration is also the fundamental principle behind GNSS. The GNSS satellites continuously broadcast signals containing precise timestamps of the moment of transmission. A terrestrial GNSS receiver captures these signals and records their ToA. To estimate distances to satellites, the receiver calculates pseudoranges by multiplying the time of flight, the difference between the ToA and transmitted timestamps, by the speed of light. These measurements are called

"pseudoranges" because they include errors due to the clock offset between the GNSS receiver and the satellites. By collecting pseudorange measurements from at least four satellites, the GNSS receiver can simultaneously solve for its three-dimensional position and clock offset. This process enables accurate positioning despite the lack of a synchronized clock in the receiver.

One of the main limitations of multilateration, as well as triangulation, is that the underlying ranging methods typically require a LoS connection between the device and the reference points. When this LoS is obstructed, due to walls, buildings, or other objects, the resulting measurements can become inaccurate, leading to significant positioning errors. In environments where a sufficient number of reference points are available, the system can often compensate for these errors. Redundant measurements from multiple anchors increase the chances that at least some of the paths remain unobstructed, helping to maintain a reasonable level of accuracy even in challenging conditions.

4.2.2 Ranging using multiple antennas

As an alternative to conventional time-based ranging techniques, a novel ranging method is introduced for maritime applications in Paper V. This approach relies on amplitude and phase measurements captured by multiple vertically spaced antenna elements, exploiting the inherent range information present in the two-ray model. Unlike traditional one-way ToA ranging methods, the primary advantage of this technique lies in its independence from time synchronization between the base stations and between the base station and the vessel. This time independence makes the proposed positioning technique fully decoupled from GNSS, which is typically used for the time synchronization of the base stations in conventional systems. As a result, the method is particularly valuable as a redundant or backup positioning solution in scenarios where GNSS is unreliable.

Not being a time-based method, the ranging performance is not directly affected by the bandwidth. Hence, the proposed ranging method could be used for narrowband systems, e.g. $< 1\,\text{MHz}$. Note that having a higher bandwidth could make the ranging performance more resilient against narrowband interference.

Despite its advantages, the method presents its own set of challenges. Accurate phase calibration, precise knowledge of the antenna phase centers and their vertical positioning, and a detailed understanding of the reflections of the sea surface are all critical factors that influence performance. These challenges have been systematically addressed in Paper V through the development of an over-the-air calibration algorithm. This calibration process involves prior mea-

surements, which can be collected in real-world scenarios where GNSS is used as the primary positioning reference. By integrating these calibration procedures, the method becomes both practical and resilient for GNSS-independent ranging.

Chapter 5

Contributions and Conclusions

5.1 General Conclusions

Deploying multiple antennas in maritime radio channels provides significant advantages. The effective use of multiple antennas is achieved when they are vertically distributed over several meters because of dominant scattering in the elevation domain. Through both theoretical and experimental investigations, we concluded that the benefits of vertical antenna arrays are two-fold: fading mitigation and positioning. While it is well-known that multiple antennas can mitigate fading, this thesis provides closed-form expressions that quantify how many antennas are needed and the required spacing between them. These calculations are based on the classical two-ray ground reflection model. While being a simple model, measurements have shown that the two-ray model is suitable for analyzing fading mitigation with vertical antenna arrays in open-sea scenarios where the sea surface is the dominant scatterer. In addition, this thesis demonstrates that the two-ray model can be utilized as a basis to perform ranging between a vessel at sea and a base station on land with a vertical antenna array. Employing only eight antennas at 5.6 GHz, results demonstrate a ranging accuracy of 6.3 meters, making this approach suitable as a backup system for GNSS. This method does not require time synchronization between base stations for positioning, unlike techniques such as ToA. However, for good ranging performance, accurate modeling of the sea surface reflection coefficient, calibration of the position of the antenna phase centers, and calibration RF chain contributions are crucial. Nevertheless, additional measurements results have shown that in harbor envi-

ronments the two-ray model is not accurate for fading mitigation and ranging as there are more scatterers in this environment, giving rise to multipath propagation. The harbor measurement did, however, show clear multipath trajectories, which could potentially be used for positioning using the multipath-SLAM technique. Furthermore, the channel sounder presented in this thesis demonstrates that a hybrid architecture, combining parallel RF chains with RF switches, enables high-performance, scalable, and cost-effective distributed massive MIMO measurements, while custom FPGA programming of the USRP is essential to handle the high bandwidth and large amount of antennas.

5.2 Research Contributions

5.2.1 Paper I: Antenna Array Configuration for Reliable Communications in Maritime Environments

Understanding the impact of vertical antenna spacing in a two-ray environment is important to mitigate fading, but the precise spacing required and its performance prediction remained unclear. This work provides new theoretical insights by deriving closed-form expressions that define the bounds of the distance range where deep fading can be mitigated. These findings offer a systematic way to optimize antenna configuration. Using these insights, engineers can make informed decisions on antenna deployment, leading to more robust and reliable wireless communication networks. This paper reveals that fading mitigation occurs within a specific range, whose bounds can be calculated using closed-form expressions. The maximum distance is proportional to the total aperture of the antenna array, while increasing the number of antennas influences the minimum distance. Notably, the offset of the first antenna above the sea surface does not have an impact on the bounds, allowing flexible placement, such as on elevated terrain. Moreover, even a small number of antennas proves highly effective in practical scenarios, making this approach both efficient and feasible for real-world applications.

5.2.2 Paper II: Measurement-Based Wideband Maritime Channel Characterization

This paper addresses the need for a characterization of wideband maritime propagation channels, which is essential for optimizing modern maritime communication systems. While it is known that maritime environments present unique propagation challenges, there has been limited insight into the wideband characteristics of these channels, particularly their variations in different maritime scenarios. Existing studies have focused primarily on lower bandwidths, providing only a partial understanding of the channel behavior. To bridge this gap, we conducted high-resolution measurements at 5.6 GHz with a 250 MHz bandwidth in both harbor and open-sea environments. The novelty of this work is the enhanced insight gained from this higher bandwidth, allowing us to analyze the distinct wideband properties of maritime propagation channels in different scenarios. Our findings reveal that the harbor environment exhibits more complex multipath characteristics compared to open-sea scenario. Additionally, the distinct MPC trajectories observed in the harbor scenario suggest the potential for MPC-based localization techniques. These insights contribute to a better understanding of the maritime radio channel, supporting the design of robust and efficient maritime wireless systems. However, this study serves as an initial investigation rather than a comprehensive empirical modeling effort, and measurements were not conducted over very long distances, which limits the scope of the conclusions.

5.2.3 Paper III: A Wideband Distributed Massive MIMO Channel Sounder for Communication and Sensing

This work addresses the need for a high-performance channel sounder capable of meeting the stringent requirements of 6G research, particularly for distributed massive MIMO and sensing. Existing sounders struggle to simultaneously capture channel characteristics across time, frequency, and spatial domains, limiting their ability to provide realistic insights for next-generation wireless systems. To bridge this gap, we present a novel wideband distributed massive MIMO channel sounder operating at 5–6 GHz with a 400 MHz bandwidth, built on NI USRP X410 hardware. The system integrates parallel RF chains and RF switches, allowing for scalable, multi-node measurements with thousands of antenna combinations

in milliseconds. Through verification measurements in an indoor laboratory, we demonstrate the sounder's capability for both communication and sensing applications. The sounder's flexible architecture and open-source implementation contribute to the reproducibility of channel sounder and measurements within the scientific community, making it a valuable tool for advancing 6G system development. Its impact is already evident, having led to three journal papers and four conference papers within two years, highlighting its role in bridging the gap between theoretical advancements and real-world performance of wireless systems.

5.2.4 Paper IV: Mitigating Sea Surface Fading with D-MIMO: Experimental Validation

This paper investigates how D-MIMO systems can mitigate sea surface fading in maritime communication by addressing the need for experimental validation of theoretical findings in Paper I that predict fading mitigation for vertical antenna arrays. While previous studies have established the potential benefits of distributed antenna systems, measurement-based verification has been lacking. To address this limitation, we conducted a unique measurement campaign at 5.6 GHz using 64 dual-polarized antennas, analyzing the impact of co-located and distributed antenna configurations on fading reduction. The results confirm that strategically spacing antennas significantly mitigates deep fading dips caused by sea surface reflections, achieving up to a 15 dB improvement with only three antennas. The findings provide practical insights into optimal system design, demonstrating that a small number of well-placed antennas can enhance maritime communication reliability without requiring extensive infrastructure. The results validate theoretical predictions and offer guidance for deploying effective D-MIMO configurations in real-world maritime environments.

5.2.5 Paper V: Leveraging the Two-Ray Model for C-band Ranging in Maritime Applications

This paper introduces a novel maritime ranging method that leverages the two-ray model. This method eliminates the need for time synchronization and is suitable for narrowband systems, complementing other radio-based localization techniques. A theoretical analysis using the Cramér-Rao bound confirms that

ranging accuracy is strongly influenced by antenna spacing and the vessel's antenna height. The study further identifies four key practical challenges: RF chain calibration, antenna phase center alignment, antenna height estimation, and sea surface reflection characterization. To address these, a refined channel model and an estimation algorithm have been developed, incorporating over-the-air calibration techniques. Experimental validation shows that the proposed ranging method achieves an root mean square error (RMSE) of 6 meters for distances between 700 and 2800 meters, indicating that large-aperture vertical arrays are not only effective in mitigating sea surface fading but also are instrumental for ranging as part of a positioning system that complements GNSS. It has also been found that the height of the antenna on top of a sailboat describes a non-stationary process. The local mean of the antenna height was estimated based the heeling of the boat, which was estimated using IMU data. Utilizing the local mean estimates, a Kalman filter could be employed to filter out the ranging errors due to the local height variations. In addition, this paper also evaluates different sea surface reflection models, showing that existing theoretical models do not fully capture real-world conditions. Overall, the proposed approach offers a robust backup for GNSS-based positioning, particularly in situations where GNSS signals may be unreliable.

5.3 Future Work

The investigations in Paper I and Paper IV are limited to uniform linear antenna arrays. Future work could explore other antenna array configurations to enhance performance and enable more flexible deployment scenarios. The derivations were based on the planar two-ray model, and an attempt could be made to extend those to the round-Earth two-ray model. Furthermore, diffraction loss was assumed negligible within the calculated ranges. However, this assumption becomes less valid at larger distances, especially near the horizon. To improve performance predictions in such scenarios, diffraction loss should be incorporated. The neglect of diffraction loss is also tied to the specific formulation of the optimization problem used. An alternative approach might involve optimizing for the SNR at larger distances, allowing localized fading dips at closer ranges where the SNR is naturally higher.

In Paper III, the channel sounder employed a sequential antenna switching pattern, which is susceptible to ambiguity between Doppler frequency and AoA or AoD. A non-linear switching scheme could mitigate this ambiguity. Moreover,

equipping each panel with a PA, low-noise amplifier (LNA), and a time division duplexing (TDD) RF switch would improve the link budget.

Paper II revealed distinct MPC trajectories in a harbor environment. This insight opens up the possibility of exploring MPC-based SLAM as a backup positioning method in such settings, particularly valuable where the approach from Paper V is not applicable.

A key limitation of Paper V is the restricted distance range of the measurement-based model validation. A natural next step is to refine the channel model and evaluate its accuracy at larger distances. Discrepancies between measurements and the model suggest a degree of model mismatch. More accurate modeling could potentially improve positioning performance. Incorporating correct variance estimates or leveraging information about the likelihood distribution could enable effective the use of Bayesian filtering techniques, potentially improving accuracy by an order of magnitude or more. For instance, the results suggest that assuming equal antenna gain for LoS and reflected paths might be oversimplified, and a more accurate model could yield better performance. It could also be valuable to derive Bayesian bounds for ranging to better understand the fundamental limits. In addition, the accuracy of the local transmit antenna height was found to be a key factor limiting ranging performance. However, this limitation may be mitigated by using three base stations to estimate the position, as the transmit antenna height can theoretically be jointly estimated along with the position, but this has to be further investigated and verified.

Additional measurements in varied sea states and at extended ranges are essential. Establishing an empirical probabilistic model of sea state parameters, as presented in Paper V, would help in generalizing the findings and improving robustness.

5.4 Outlook

Looking ahead, vertically distributed antenna arrays hold great promise for future marine networks due to their fading mitigation benefits and positioning capabilities. One of the key challenges in realizing this lies in developing cost-effective and energy-efficient implementations suitable for large-scale deployment. Optimizing antenna design and intelligently grouping them to reduce the number of RF chains could for example save costs, though this must be carefully evaluated for its impact on ranging accuracy.

Larger communication ranges can be achieved by integrating TNs with NTNs.

User density is naturally higher near coastlines due to concentrated maritime activity, and TNs are well-suited to handle due to their higher capacity and lower latency. Farther from the coastline, user density naturally decreases, as fewer vessels operate in remote offshore areas compared to the busy, high-traffic zones near ports and coastal infrastructure. In these offshore regions, NTNs can provide essential wide-area coverage. Seamless integration between TNs and NTNs is crucial to ensure continuous, reliable communication across varying distances from shore.

Based on the ranging results in this thesis, the deployment of coastal antenna arrays could enable tracking of any signal source with a partly known waveform, regardless of bandwidth, provided the signal energy is sufficient. A complementary idea is to equip boats with vertical antenna arrays. While the effective aperture may be smaller than land-based installations, these arrays could still provide self-localization capabilities using existing signals in the environment, as long as the waveform is (at least partially) known, together with the location and height of its source.

References

[1] R. Simons, “Guglielmo Marconi and Early Systems of Wireless Communication,” *Gec Review*, vol. 11, no. 1, pp. 37–55, 1996.

[2] “Remote Pilotage – an Introduction.” [Online]. Available: https://remotepilotage.fi/remote-pilotage-intro

[3] International Maritime Organization, “Autonomous shipping.” [Online]. Available: https://www.imo.org/en/MediaCentre/HotTopics/Pages/Autonomous-shipping.aspx

[4] J. Hellekant, “Test och utvärdering av framdrivningssystem för drönare avsedd för sjöräddning,” 2020. [Online]. Available: https://hdl.handle.net/20.500.12380/301764

[5] 3GPP, “Technical Specification Group Services and System Aspects; Feasibility Study on Maritime Communication Servicesover 3GPP system; Stage 1 (Release 16),” 3rd Generation Partnership Project (3GPP), Technical Specification (TS) 22.819, Dec. 2018, version 16.2.0.

[6] “Integrated 6G TN and NTN Localization: Challenges, Opportunities, and Advancements,” Jan. 2025, arXiv:2501.13488 [eess]. [Online]. Available: http://arxiv.org/abs/2501.13488

[7] C. Günther, “A Survey of Spoofing and Counter-Measures,” *NAVIGATION*, vol. 61, no. 3, pp. 159–177, 2014.

[8] International Maritime Organization, “MSC.1/Circ.1575 Guidelines for shipborne position, navigation and timing (PNT) data processing,” June 2017. [Online]. Available: https://www.imo.org/en/OurWork/Safety/Pages/Docs-ShipborneRC-NavigationEquipment.aspx

[9] E. G. Larsson, O. Edfors, F. Tufvesson, and T. L. Marzetta, “Massive MIMO For Next Generation Wireless Systems,” *IEEE Communications Magazine*, vol. 52, no. 2, pp. 186–195, 2014.

[10] F. Rusek, D. Persson, B. K. Lau, E. G. Larsson, T. L. Marzetta, O. Edfors, and F. Tufvesson, “Scaling Up MIMO: Opportunities and Challenges with Very Large Arrays,” *IEEE Signal Processing Magazine*, vol. 30, no. 1, pp. 40–60, 2012.

[11] H. Q. Ngo, A. Ashikhmin, H. Yang, E. G. Larsson, and T. L. Marzetta, "Cell-Free Massive MIMO Versus Small Cells," *IEEE Transactions on Wireless Communications*, vol. 16, no. 3, pp. 1834–1850, Mar. 2017.

[12] A. F. Molisch, *Wireless Communications*, 2nd ed. Wiley-IEEE Press, 2011.

[13] H. Tataria, K. Haneda, A. F. Molisch, M. Shafi, and F. Tufvesson, "Standardization of Propagation Models for Terrestrial Cellular Systems: A Historical Perspective," *International Journal of Wireless Information Networks*, vol. 28, no. 1, pp. 20–44, Mar. 2021.

[14] C. Beard, I. Katz, and L. Spetner, "Phenomenological Vector Model Of Microwave Reflection From The Ocean," *IRE Transactions on Antennas and Propagation*, vol. 4, no. 2, pp. 162–167, Apr. 1956.

[15] J. C. Schelleng, C. R. Burrows, and E. B. Ferrell, "Ultra-Short Wave Propagation," *The Bell System Technical Journal*, vol. 12, no. 2, pp. 125–161, Apr. 1933.

[16] M. Katzin, R. Bauchman, and W. Binnian, "3- and 9-Centimeter Propagation in Low Ocean Ducts," *Proceedings of the IRE*, vol. 35, no. 9, pp. 891–905, Sep. 1947.

[17] H. Booker and W. Gordon, "A Theory of Radio Scattering in the Troposphere," *Proceedings of the IRE*, vol. 38, no. 4, pp. 401–412, Apr. 1950.

[18] Recommendation ITU-R P.530-18, "Propagation Data And Prediction Methods Required For The Design Of Terrestrial Line-Of-Sight Systems," Sep. 2021.

[19] K. Maliatsos, P. Loulis, M. Chronopoulos, P. Constantinou, P. Dallas, and M. Ikonomou, "Experimental Small Scale Fading Results for Mobile Channels Over the Sea," in *2006 IEEE 17th International Symposium on Personal, Indoor and Mobile Radio Communications*, Sep. 2006.

[20] R. Raulefs, M. Bellido-Manganell, A. Dammann, M. Walter, and W. Wang, "Verification and Modeling of the Maritime Channel for Maritime Communications and Navigation Networks," *Frontiers in Marine Science*, 2023.

[21] K. Yang, A. F. Molisch, T. Ekman, T. Røste, and M. Berbineau, "A Round Earth Loss Model and Small-Scale Channel Properties for Open-Sea Radio Propagation," *IEEE Transactions on Vehicular Technology*, vol. 68, no. 9, pp. 8449–8460, Sep. 2019.

[22] A. Goldsmith, *Wireless Communications*. Cambridge University Press, 2005.

[23] Y. Karasawa and T. Shiokawa, "Characteristics Of L-Band Multipath Fading Due To Sea Surface Reflection," *IEEE Transactions on Antennas and Propagation*, vol. 32, no. 6, pp. 618–623, Jun. 1984.

[24] W. Wang, R. Raulefs, and T. Jost, "Fading Characteristics Of Maritime Propagation Channel For Beyond Geometrical Horizon Communications In C-Band," *CEAS Space Journal*, vol. 11, no. 1, pp. 95–104, Mar. 2019.

[25] T. Ekman, "Fading Distribution Model for the Maritime Radio Channel," in *2024 18th European Conference on Antennas and Propagation (EuCAP)*, Mar. 2024.

[26] C. Bourlier, *Radar Propagation And Scattering In A Complex Maritime Environment*. Elsevier, Jul. 2018.

[27] W. S. Ament, "Toward a Theory of Reflection by a Rough Surface," *Proceedings of the IRE*, vol. 41, no. 1, pp. 142–146, Jan. 1953.

[28] A. R. Miller, R. M. Brown, and E. Vegh, "A New Derivation For The Rough Surface Reflection Coefficient And For The Distribution Of Sea Wave Elevations," *NASA STI/Recon Technical Report N*, vol. 84, Sep. 1983.

[29] B. Smith, "Geometrical Shadowing Of A Random Rough Surface," *IEEE Transactions on Antennas and Propagation*, vol. 15, no. 5, pp. 668–671, Sep. 1967.

[30] R. J. Wagner, "Shadowing Of Randomly Rough Surfaces," *J. Acoust. Soc. Am.*, vol. 41, pp. 138–147, 1967.

[31] P. Beckmann, "Shadowing Of Random Rough Surfaces," *IEEE Transactions on Antennas and Propagation*, vol. 13, no. 3, pp. 384–388, May 1965.

[32] T. Elfouhaily, B. Chapron, K. Katsaros, and D. Vandemark, "A Unified Directional Spectrum For Long And Short Wind-Driven Waves," *Journal of Geophysical Research: Oceans*, vol. 102, no. C7, pp. 15 781–15 796, 1997.

[33] S. O. Rice, "Reflection Of Electromagnetic Waves From Slightly Rough Surfaces," *Communications on Pure and Applied Mathematics*, vol. 4, no. 2-3, pp. 351–378, 1951.

[34] W. Wang, G. Hoerack, T. Jost, R. Raulefs, M. Walter, and U.-C. Fiebig, "Propagation Channel At 5.2 GHz In Baltic Sea With Focus On Scattering Phenomena," in *2015 9th European Conference on Antennas and Propagation (EuCAP)*, Apr. 2015.

[35] V. Fock, *Electromagnetic Diffraction And Propagation*. Oxford, England: Pergamon, 1965.

[36] M. Shatz and G. Polychronopoulos, "An Algorithm For The Evaluation Of Radar Propagation In The Spherical Earth Diffraction Region," *IEEE Transactions on Antennas and Propagation*, vol. 38, no. 8, pp. 1249–1252, Aug. 1990.

[37] K. Bullington, "Radio Propagation at Frequencies above 30 Megacycles," *Proceedings of the IRE*, vol. 35, no. 10, pp. 1122–1136, Oct. 1947.

[38] Recommendation ITU-R P.526-15, "Propagation By Diffraction," Oct. 2019.

[39] Recommendation ITU-R P.2001-3, "A General Purpose Wide-Range Terrestrial Propagation Model In The Frequency Range 30 Mhz To 50 Ghz," Aug. 2019.

[40] Recommendation ITU-R P.1546-6, "Method for point-to-area predictions for terrestrial services in the frequency range 30 MHz to 4 000 MHz ," Aug. 2019.

[41] W. Wang, R. Raulefs, and T. Jost, "Fading Characteristics Of Ship-To-Land Propagation Channel At 5.2 GHz," in *OCEANS 2016 - Shanghai*, Apr. 2016, pp. 1–7.

[42] M. Sandra, G. Tian, A. Fedorov, X. Cai, and A. J. Johansson, "Measurement-Based Wideband Maritime Channel Characterization," *The 17th European Conference on Antennas and Propagation (EuCAP 2023)*, 2023.

[43] Y. He, H. Chang, Y. Liu, W. Zhang, J. Sun, and C.-X. Wang, "A 3D GBSM For Ship-To-Land Communications," in *2019 IEEE/CIC International Conference on Communications in China (ICCC)*, Aug. 2019, pp. 967–972.

[44] Y. He, C.-X. Wang, H. Chang, J. Huang, J. Sun, W. Zhang, and E.-H. M. Aggoune, "A Novel 3D Non-Stationary Maritime Wireless Channel Model," *IEEE Transactions on Communications*, vol. 70, no. 3, pp. 2102–2116, Mar. 2022.

[45] Y. He, C.-X. Wang, H. Chang, R. Feng, J. Sun, W. Zhang, Y. Hao, and E.-H. M. Aggoune, "A Novel 3-D Beam Domain Channel Model For Maritime Massive MIMO Communication Systems Using Uniform Circular Arrays," *IEEE Transactions on Communications*, vol. 71, no. 4, pp. 2487–2502, Apr. 2023.

[46] X. Cai, E. L. Bengtsson, O. Edfors, and F. Tufvesson, "A Switched Array Sounder for Dynamic Millimeter-Wave Channel Characterization: Design, Implementation and Measurements," *IEEE Transactions on Antennas and Propagation*, 2023.

[47] W. Fan, H. Sun, Y. Lyu, X. Zhang, J. Borrill, J. Zhang, B. Derat, and F. Zhang, "6G Radio Channel Sounding: Challenges and Potential Solutions," *IEEE Wireless Communications*, vol. 32, no. 1, pp. 100–106, Feb. 2025.

[48] T. Choi, P. Luo, A. Ramesh, and A. F. Molisch, "Co-Located vs Distributed vs Semi-Distributed MIMO: Measurement-Based Evaluation," in *2020 54th Asilomar Conference on Signals, Systems, and Computers*, Nov. 2020, pp. 836–841.

[49] D. Stanko, G. Sommerkorn, A. Ihlow, and G. D. Galdo, "Enable SDRs for Real-Time MIMO Channel Sounding featuring Parallel Coherent Rx Channels," in *2022 IEEE 95th Vehicular Technology Conference: (VTC2022-Spring)*, Jun. 2022.

[50] S. Malkowsky, J. Vieira, L. Liu, P. Harris, K. Nieman, N. Kundargi, I. C. Wong, F. Tufvesson, V. Öwall, and O. Edfors, "The World's First Real-Time Testbed for Massive MIMO: Design, Implementation, and Validation," *IEEE Access*, vol. 5, pp. 9073–9088, 2017.

[51] D. Löschenbrand, M. Hofer, L. Bernadó, G. Humer, B. Schrenk, S. Zelenbaba, and T. Zemen, "Distributed Massive MIMO Channel Measurements in Urban Vehicular Scenario," in *2019 13th European Conference on Antennas and Propagation (EuCAP)*, Mar. 2019.

[52] A. P. Guevara, S. De Bast, and S. Pollin, "Weave and Conquer: A Measurement-based Analysis of Dense Antenna Deployments," in *ICC 2021 - IEEE International Conference on Communications*, Jun. 2021.

[53] C. Nelson, X. Li, A. Fedorov, B. Deutschmann, and F. Tufvesson, "Distributed MIMO Measurements for Integrated Communication and Sensing in an Industrial Environment," *Sensors*, vol. 24, no. 5, p. 1385, Jan. 2024.

[54] D. A. Wassie, I. Rodriguez, G. Berardinelli, F. M. L. Tavares, T. B. Sørensen, T. L. Hansen, and P. Mogensen, "An Agile Multi-Node Multi-Antenna Wireless Channel Sounding System," *IEEE Access*, vol. 7, pp. 17 503–17 516, 2019.

[55] J. Vieira, S. Malkowsky, K. Nieman, Z. Miers, N. Kundargi, L. Liu, I. Wong, V. Öwall, O. Edfors, and F. Tufvesson, "A flexible 100-antenna testbed for Massive MIMO," in *2014 IEEE Globecom Workshops (GC Wkshps)*, Dec. 2014, pp. 287–293.

[56] S. Willhammar, J. Flordelis, L. Van Der Perre, and F. Tufvesson, "Channel Hardening in Massive MIMO: Model Parameters and Experimental Assessment," *IEEE Open Journal of the Communications Society*, vol. 1, pp. 501–512, 2020.

[57] G. Tian, D. Pjanić, X. Cai, B. Bernhardsson, and F. Tufvesson, "Attention-Aided Outdoor Localization in Commercial 5G NR Systems," *IEEE Transactions on Machine Learning in Communications and Networking*, vol. 2, pp. 1678–1692, 2024.

[58] P. Laly, D. P. Gaillot, M. Lienard, P. Degauque, E. Tanghe, W. Joseph, and L. Martens, "Flexible Real-Time MIMO Channel Sounder For Multidimensional Polarimetric Parameter Estimation," in *2015 IEEE Conference on Antenna Measurements & Applications (CAMA)*, Nov. 2015.

[59] P. Laly, D. Gaillot, G. Delbarre, M. V. d. Bossche, G. Vermeeren, F. Challita, E. Tanghe, E. Simon, W. Joseph, L. Martens, and M. Liénard, "Massive Radio Channel Sounder Architecture for 5G Mobility Scenarios: MaMIMOSA," in *2020 14th European Conference on Antennas and Propagation (EuCAP)*, Mar. 2020.

[60] E. P. Simon, P. Laly, J. Farah, E. Tanghe, W. Joseph, and D. P. Gaillot, "Measurement of the V2I Channel in Cell-free Vehicular Networks with the Distributed MaMIMOSA Channel Sounder," in *2023 17th European Conference on Antennas and Propagation (EuCAP)*, Mar. 2023.

[61] J. Flordelis, G. Dahman, and F. Tufvesson, "Measurements Of Large-Scale Parameters Of A Distributed MIMO Antenna System In A Microcell Environment At 2.6 GHz," in *2013 7th European Conference on Antennas and Propagation (EuCAP)*, Apr. 2013, pp. 3026–3030.

[62] Ettus Research, "RFNoC (RF Network on Chip." [Online]. Available: https://www.ettus.com/sdr-software/rfnoc/

[63] S. Zelenbaba, D. Löschenbrand, M. Hofer, A. Dakić, B. Rainer, G. Humer, and T. Zemen, "A Scalable Mobile Multi-Node Channel Sounder," in *2020 IEEE Wireless Communications and Networking Conference (WCNC)*, May 2020.

[64] D. Stanko, M. Döbereiner, G. Sommerkorn, D. Czaniera, C. Andrich, C. Schneider, S. Semper, A. Ihlow, and M. Landmann, "Time Variant Directional Multi-Link Channel Sounding and Estimation for V2X," in *2023 IEEE 97th Vehicular Technology Conference (VTC2023-Spring)*, Jun. 2023.

[65] F. Euchner, M. Gauger, S. Doerner, and S. ten Brink, "A Distributed Massive MIMO Channel Sounder for "Big CSI Data"-driven Machine Learning," in *WSA 2021; 25th International ITG Workshop on Smart Antennas*, Nov. 2021.

[66] I. C. Sezgin, M. Dahlgren, T. Eriksson, M. Coldrey, C. Larsson, J. Gustavsson, and C. Fager, "A Low-Complexity Distributed-MIMO Testbed Based on High-Speed Sigma–Delta-Over-Fiber," *IEEE Transactions on Microwave Theory and Techniques*, vol. 67, no. 7, pp. 2861–2872, Jul. 2019.

[67] C. Nelson, X. Li, T. Wilding, B. Deutschmann, K. Witrisal, and F. Tufvesson, "Large Intelligent Surface Measurements for Joint Communication and Sensing," in *2023 Joint European Conference on Networks and Communications & 6G Summit (EuCNC/6G Summit)*, Jun. 2023, pp. 228–233.

[68] M. Alatossava, A. Taparugssanagorn, V.-M. Holappa, and J. Ylitalo, "Measurement Based Capacity of Distributed MIMO Antenna System in Urban Microcellular Environment at 5.25 GHz," in *VTC Spring 2008 - IEEE Vehicular Technology Conference*, May 2008, pp. 430–434.

[69] I. Yaman, G. Tian, M. Larsson, P. Persson, M. Sandra, A. Dürr, E. Tegler, N. Challa, H. Garde, F. Tufvesson, K. Åström, O. Edfors, S. Malkowsky, and L. Liu, "The LuViRA Dataset: Synchronized Vision, Radio, and Audio

Sensors for Indoor Localization," in *2024 IEEE International Conference on Robotics and Automation (ICRA)*, May 2024, pp. 11 920–11 926.

[70] B. Fleury, M. Tschudin, R. Heddergott, D. Dahlhaus, and K. Ingeman Pedersen, "Channel parameter estimation in mobile radio environments using the SAGE algorithm," *IEEE Journal on Selected Areas in Communications*, vol. 17, no. 3, pp. 434–450, Mar. 1999.

[71] A. Richter, "Estimation of Radio Channel Parameters: Models and Algorithms," Ph.D. dissertation, Ilmenau University of Technology, Germany, 2005.

[72] D. G. Arogyaswami Paulraj, Rohit Nabar, *Introduction To Space-Time Wireless Communications*. Cambridge University Press, 2003.

[73] J. A. del Peral-Rosado, R. Raulefs, J. A. López-Salcedo, and G. Seco-Granados, "Survey of Cellular Mobile Radio Localization Methods: From 1G to 5G," *IEEE Communications Surveys & Tutorials*, vol. 20, no. 2, pp. 1124–1148, 2018.

[74] G. Tian, I. Yaman, M. Sandra, X. Cai, L. Liu, and F. Tufvesson, "Deep-Learning-Based High-Precision Localization With Massive MIMO," *IEEE Transactions on Machine Learning in Communications and Networking*, vol. 2, pp. 19–33, 2024.

[75] C. Gentner, T. Jost, W. Wang, S. Zhang, A. Dammann, and U.-C. Fiebig, "Multipath Assisted Positioning with Simultaneous Localization and Mapping," *IEEE Transactions on Wireless Communications*, vol. 15, no. 9, pp. 6104–6117, Sep. 2016.

[76] X. Li, E. Leitinger, M. Oskarsson, K. Åström, and F. Tufvesson, "Massive MIMO-Based Localization and Mapping Exploiting Phase Information of Multipath Components," *IEEE Transactions on Wireless Communications*, vol. 18, no. 9, pp. 4254–4267, Sep. 2019.

[77] D. Dardari, A. Conti, U. Ferner, A. Giorgetti, and M. Z. Win, "Ranging With Ultrawide Bandwidth Signals in Multipath Environments," *Proceedings of the IEEE*, vol. 97, no. 2, pp. 404–426, Feb. 2009.

Part II: Included Papers

Antenna Array Configuration for Reliable Communications in Maritime Environments

Paper I

Michiel Sandra, Guoda Tian, Xuesong Cai, Anders J Johansson

Published as: M. Sandra, G. Tian, X. Cai, A. J. Johansson, "Antenna Array Configuration for Reliable Communications in Maritime Environments," *2022 IEEE 95th Vehicular Technology Conference (VTC Spring)*, Helsinki, Finland, 2022.

Abstract

The performance and reliability of wireless communications at sea are often limited by the deep fades caused by the coherent sea surface reflection. In this paper, we show that by employing multiple antennas at the base station, the deep fades can be mitigated within a large communication range if the antennas are carefully spaced in the vertical direction. We derive a bound for the range where mitigation of deep fading is guaranteed and evaluate this bound through numerical searching methods utilizing a realistic channel model that considers the curvature of the earth. The numerical results show that the proposed scheme leads to a better system performance compared with a free space scenario in terms of signal-to-noise ratio, if four or more antennas are employed at the base station.

1 Introduction

In a typical maritime environment, the strong coherent reflection from the sea surface leads to deep fades which limit the reliability and performance of wireless systems at sea. A promising remedy is to apply a multiple antenna system for its well-known capability to mitigate the fading effects. Fundamental to the analysis of multiple antenna system performance, it is essential to evaluate different spatial configurations of the antennas. Therefore, it is of great interest to study the effect of the spacing between the adjacent antennas specifically for the maritime environment.

According to literature, multiple antenna systems for the maritime environment have previously been considered in [1–4]. Moreover, the authors of [5, 6] showed that the deep fading in another dominant two-ray environment can be mitigated by employing a system with the antennas stacked in the vertical direction. Nevertheless, none of these works have, to the best of our knowledge, elaborated on how much the antennas should be spaced to mitigate the deep fading due to the coherent sea surface reflection. To fill this gap, the goal of this paper is to analyze the effect of the spacing between adjacent elements of a linear antenna array on the performance of mitigating the deep fading in typical maritime propagation scenarios. More specifically, we evaluate the extent of the range where deep fading is absent. In order to do this, we derived closed-form expressions for the bound of this range and provide an evaluation through numerical simulations. The outcome of this paper can serve as a guideline for systems designers to ensure reliable communication for various applications at sea such as high-speed internet on ferries, surveillance, search and rescue services, among others. The rest of this paper is structured as follows. In Section 2, we introduce a channel model for maritime communication. The coverage range under the

maritime channel condition is analyzed in Section 3, and a scheme of improving the coverage is also proposed. Section 4 evaluates the proposed scheme through numerical approaches. Conclusions are finalized in Section 5.

2 Channel Model

In a maritime environment, assuming there is a line-of-sight (LoS) path and considering the sea as the only scatterer, the total received field can typically be modelled as the sum of three components [7], namely

1. a direct component with constant amplitude and phase that represents the field corresponding to the LoS path,
2. a time-average coherent component with amplitude and phase determined by a certain geometry and sea state,
3. a random incoherent component whose statistical properties depend on the sea state.

Therefore, the propagation channel can be characterized as a two-ray model plus a random component. Based on this and considering all antennas to be omnidirectional with 0 dBi gain[1], the channel gain g can be expressed as

$$g = \frac{\lambda}{4\pi d}\left(1 + R\exp(j\theta)\right) + \nu, \tag{2.1}$$

where λ is the wavelength of the transmitted signal, d is the distance between the transmitter and the receiver, and R is the complex coherent reflection coefficient of the sea surface which can be obtained through measurement or theoretical models [8–10]. The complex random variable ν models the incoherent component and can be approximated by a complex Gaussian variable, i.e. $\nu \sim \mathcal{CN}(0, \sigma^2)$. Hence, the amplitude of g will follow a Rician distribution which has been validated with measurements in [11, 12]. The variable θ is the phase of the coherent component relative to the direct component due to their path difference, and can be expressed as [13]

$$\theta = \frac{4\pi h_{\mathrm{t}} h_{\mathrm{r}}}{\lambda d}, \tag{2.2}$$

where h_{r} and h_{t} are the receiver and transmitter antenna heights above sea level, respectively. However, (2.2) does not consider the curvature of the earth and the refraction effect in the air. To account for these effects, we introduce the

[1]This assumption does not affect the essence of the analysis in Section 3.

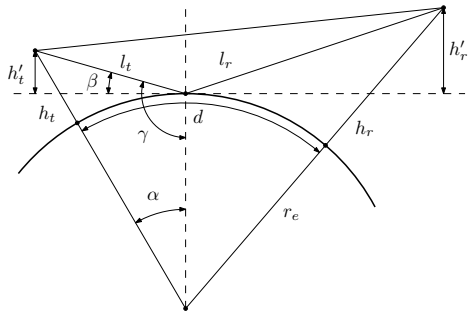

Figure 1: The two-ray model applied in the round earth geometry. h_t and h_r are the antenna heights, d is the great-circle distance between transmitter (Tx) and receiver (Rx), r_e is the effective earth's radius. h'_t and h'_r are the antenna height relative to the the imaginary plane tangent to the earth at the point of reflection.

effective radius of the earth r_e as an additional variable [14] and then modify the antenna heights stated in Eq. (2.2). For the sake of readability, we quote the final modifications as (2.3) and (2.4) while the full derivation can be found in the Appendix.

$$h'_\mathrm{t} = h_\mathrm{t} - \frac{1}{2}\left(\frac{h_\mathrm{t}}{h_\mathrm{t}+h_\mathrm{r}}\right)^2 \frac{d^2}{r_\mathrm{e}} \tag{2.3}$$

$$h'_\mathrm{r} = h_\mathrm{r} - \frac{1}{2}\left(\frac{h_\mathrm{r}}{h_\mathrm{t}+h_\mathrm{r}}\right)^2 \frac{d^2}{r_\mathrm{e}} \tag{2.4}$$

The model given by (2.1) and (2.2), including the modifications in (2.3) and (2.4), is valid for distances where diffraction loss is negligible. If diffraction loss has to be considered, readers are referred to the ITU-R 526 model [15] for the calculation of g. Furthermore, it has to be noted that propagation effects such as ducting and troposcatter are not considered in the model above.

Because the distances between a vessel and a base station in a maritime environment are large, the angle of incidence under which the radio waves approaches the sea surface can be approximated as $\pi/2$ and therefore $\angle R \approx \pi$. Hence, according to the model presented previously, g will experience deep fades when d approaches

$$d_k = \frac{2h'_\mathrm{t}h'_\mathrm{r}}{\lambda k}, k \in_0 . \tag{2.5}$$

From (2.5), it is clear that these distances with deep fades depend on the receive and transmit antenna heights, and the carrier frequency. By employing multiple antennas at the base station, the effect of a deep fade could potentially be mitigated since the simultaneous occurrence of a deep fade at two or more antenna

elements can be avoided. Moreover, it can be easily found from (2.5) that spacing the antennas in the vertical direction is a promising solution because d_k in (2.5) can be more easily altered in practice by changing h_r. This has also already been demonstrated by [5, 6].

3 Analysis

We consider a narrowband single-input multiple-output (SIMO) system in a typical maritime environment where the signals are transmitted by a vessel at sea equipped with a single antenna to a base station located close to the shore equipped with a uniform linear array (ULA) with N antennas. The received signal vector $\mathbf{y} \in \mathbb{C}^{N\times 1}$ can be written as

$$\mathbf{y} = \mathbf{g}s + \mathbf{n}, \tag{3.1}$$

where the complex vector $\mathbf{g} \in \mathbb{C}^{N\times 1}$ represents the uplink channel response of which each entry can be calculated by (2.1) with the corresponding value for θ, based on the heights of the different antennas. We furthermore assume that the values for the additive white noise term ν in (2.1) for each entry in $\mathbf{g}$ are uncorrelated, i.e., $\mathbb{E}[\nu_0\nu_1^*] = 0$. The scalar s represents the transmitted signal, and the complex vector $\mathbf{n} \in \mathbb{C}^N$ denotes the additive white Gaussian noise (AWGN) with zero mean and covariance matrix $\frac{N_0}{2}\mathbf{I}_N$ where $\mathbf{I}_N \in \mathbb{R}^{N\times N}$ represents the identity matrix. Following this definition, the maximum signal-to-noise ratio (SNR) achieved using maximum-ratio combining (MRC) can be expressed as $E_s||\mathbf{g}||_F^2/N_0$ where E_s represents the transmit signal energy.

As a first step to analyze the effect the spacing of the antennas, we propose a metric to investigate the performance of the system, which is the SNR gain relative to the free-space propagation scenario and can be calculated as

$$\gamma = \frac{E_s||\mathbf{g}||_F^2/N_0}{E_s N(\lambda/(4\pi d))^2/N_0} = \frac{||\mathbf{g}||_F^2}{N(\lambda/(4\pi d))^2}. \tag{3.2}$$

By taking this ratio, we can comprehensively evaluate the SNR gain brought by our methods over all distances in practice. Based on the model in (3.1), the expected value of γ can be written as

$$\mathbb{E}[\gamma] = 1 + |R|^2 + \sigma^2 + \frac{2|R|}{N}\sum_{n=0}^{N-1}\cos(\phi + \theta_n), \tag{3.3}$$

where ϕ is the phase of R and θ_n is the phase difference between the direct and coherent component corresponding to n-th receive antenna. From (3.3), it is clear

that a deep fade can occur when the sum in (3.3) approaches $-N$. To mitigate the deep fades, an intuitive attempt is to find a feasible antenna deployment scheme so that the lower bound of (3.3), i.e. $\sum_n \cos(\phi + \theta_n)$, is maximized for all distance d within a relevant range. However, this is a challenging task due to the presence of highly non-linear trigonometric functions. As an alternative approach, since the value of the sum depends on d through θ_n, we can propose a scheme so that the fades are mitigated within a certain range. In other words, sufficient received SNR gain at the vessel can always be achieved inside this range. To this end, we define an SNR threshold β for (3.3), i.e. $\mathbb{E}[\gamma] \geq \beta$. The exact value of β depends on the requirements of different applications. By rearranging the terms presented in the inequality $\mathbb{E}[\gamma] \geq \beta$, we yield

$$\sum_{n=0}^{N-1} \cos(\phi + \theta_n) \geq -N\alpha, \tag{3.4}$$

where scalar α equals $\frac{1+|R|^2+\sigma^2-\beta}{2|R|}$.

Furthermore, we constraint our scope to a vertically linear array for two reasons. *i)* A vertical array is more effective to harvest diversity in maritime scenarios compared to a horizontal array. *ii)* The performance of a linear array is mathematically tractable, which is helpful to gain useful insights. In terms of this specific type of array, it is necessary to analyze the influences of three important parameters, namely, the space between two adjacent antennas Δh, the height of lowest antenna inside the array $h_{r,0}$ above sea level and the number of antennas N. It is obvious that we should target a larger range by adjusting parameters Δh, $h_{r,0}$, N, so that a vessel is guaranteed to have a qualified received SNR. In the following paragraphs, we derive *closed-form* expressions for the bounds of this range. To increase readability, we first ignore the curvature of the earth in order to gain insight on the effects of parameters Δh, $h_{\mathrm{r},0}$ and N. Nevertheless, we will later evaluate the accuracy loss caused by the ignorance of earth curvature by numerical methods.

We now consider a vertical ULA at the base station with the height of the lowest antenna $h_{\mathrm{r},0}$ and spacing Δh. Based on this, θ_n equals to

$$\theta_n = \theta_0 + n\theta_\Delta,\ n = 0, \ldots, N-1 \tag{3.5}$$

where

$$\theta_0 = \frac{4\pi h_{\mathrm{t}} h_{\mathrm{r},0}}{\lambda d} - \phi \tag{3.6}$$

$$\theta_\Delta = \frac{4\pi h_{\mathrm{t}} \Delta h}{\lambda d} \tag{3.7}$$

Applying geometric summations, the left hand side of (3.4) can be simplified as

$$\sum_{n=0}^{N-1} \cos(\phi + \theta_n) = \frac{\cos\left(\theta_0 + (N-1)\,\frac{\theta_\Delta}{2}\right) \sin\frac{N\theta_\Delta}{2}}{\sin\frac{\theta_\Delta}{2}}. \tag{3.8}$$

Substituting (3.8) into (3.4) and rearranging the term yield

$$\frac{\cos\left(\theta_0 + (N-1)\,\frac{\theta_\Delta}{2}\right) \sin\frac{N\theta_\Delta}{2}}{N\sin\frac{\theta_\Delta}{2}} \leq \alpha. \tag{3.9}$$

However, finding the precise ranges of d which satisfy (3.9) is mathematically difficult. Therefore, we resort to a sufficient condition for (3.9) which is mathematically solvable, yet still provides insights. By setting the numerator of (3.9) to one and rearranging the equation, we can find the following sufficient condition:

$$\left|\sin\frac{\theta_\Delta}{2}\right|^{-1} \leq N\alpha. \tag{3.10}$$

Subsequently, we find a range for θ_Δ which is

$$2\arcsin\frac{1}{N\alpha} + 2k\pi \leq \theta_\Delta \leq 2\pi - 2\arcsin\frac{1}{N\alpha} + 2k\pi. \tag{3.11}$$

where $k \in \mathbb{N}$. It can be observed from (3.11) that multiple ranges of θ_Δ satisfy the inequality owing to the periodicity of sinusoidal functions. Similarly, leveraging the relationship between d and θ_Δ, we can rewrite the inequality in (3.11) as a variable of d as

$$d_{\mathrm{st},k} \leq d \leq d_{\mathrm{end},k}, \tag{3.12}$$

where $d_{\mathrm{st},k}$ and $d_{\mathrm{end},k}$ represent the starting and ending points of the k-th distance interval which satisfies (3.10), respectively. They are expressed as

$$d_{\mathrm{st},k} = \frac{2\pi h_\mathrm{t}\Delta h}{\lambda(\pi - \arcsin\frac{1}{N\alpha} + k\pi)}, \tag{3.13}$$

$$d_{\mathrm{end},k} = \frac{2\pi h_\mathrm{t}\Delta h}{\lambda(\arcsin\frac{1}{N\alpha} + k\pi)}. \tag{3.14}$$

According to equations (3.13) and (3.14), there exists multiple range of d that satisfy (3.9). It can be known that $d_{\mathrm{st},k}$ and $d_{\mathrm{end},k}$ attain the largest value when $k = 0$. To be specific, $d_{\mathrm{end},0}$ may reach 3.6 km according to the typical setup of Table 1. Since other integer k values result in much smaller $d_{\mathrm{st},k}$ and $d_{\mathrm{end},k}$, which

is inconsistent with the maritime communication scenario, we only consider the range for $k = 0$ in the sequel.

Equations (3.13) and (3.14) show that $d_{\mathrm{st},0}$ and $d_{\mathrm{end},0}$ are proportional to Δh and h_{t}, while independent on $h_{\mathrm{r},0}$. In practice, $h_{\mathrm{r},0}$ can vary due to water level changes and therefore hard to predict, i.e. it can be treated as a random variable. This means that irrespective of $h_{\mathrm{r},0}$, $d_{\mathrm{end},0}$ can be increased by enlarging the antenna spacing Δh. In reality, the value for Δh is limited because the size of the array is physically constrained. Considering a size-constrained vertical ULA with mimimum and maximum heights above sea level as $h_{\mathrm{r,min}}$ and $h_{\mathrm{r,max}}$, respectively, we propose the following antenna spacing scheme, called maximal spacing scheme:

$$\Delta h = \frac{h_{\mathrm{r,max}} - h_{\mathrm{r,min}}}{N-1}. \tag{3.15}$$

Substituting (3.15) into (3.13) and (3.14), $d_{\mathrm{st},0}$ and $d_{\mathrm{end},0}$ can be expressed as:

$$d_{\mathrm{st},0} = \frac{2\pi h_{\mathrm{t}}(h_{\mathrm{r,max}} - h_{\mathrm{r,min}})}{\lambda(N-1)(\pi - \arcsin\frac{1}{N\alpha})}, \tag{3.16}$$

$$d_{\mathrm{end},0} = \frac{2\pi h_{\mathrm{t}}(h_{\mathrm{r,max}} - h_{\mathrm{r,min}})}{\lambda(N-1)(\arcsin\frac{1}{N\alpha})}. \tag{3.17}$$

Bear in mind that since we make an approximation at (3.10), both $d_{\mathrm{st},0}$ and $d_{\mathrm{end},0}$ are rather conservative. In other words, there may exist $d'_{\mathrm{st},0} < d_{\mathrm{st},0}$ and $d'_{\mathrm{end},0} > d_{\mathrm{end},0}$ that still fulfill (14). In the next section, we apply numerical search to find the minimal of $d'_{\mathrm{st},0}$ as well as the maximal $d'_{\mathrm{end},0}$ at the neighbourhoods of $d_{\mathrm{st},0}$ and $d_{\mathrm{end},0}$, respectively.

4 Results and Discussion

In this section, we evaluate the bounds of the communication range limits derived previously. In order to do this, we numerically find the values for $d'_{\mathrm{st},0}$ and $d'_{\mathrm{end},0}$ as a function of Δh utilizing the model presented in Section 2, *with the curvature of the earth being considered*. The parameters are chosen in such a way that we evaluate the worst channel conditions. Under this propagation scenario, the direct and coherent component are similar in magnitude and the incoherent component is negligible, i.e. $R \approx -1$ and $\sigma \approx 0$. However, $R = -1$ gives rise to deep fades and therefore reduces the readability of the graphs, hence we choose $R = -0.9$. Furthermore, we take $\beta = 1$ because this means that the SNR will be higher than in a free space scenario within the communication range. The

Table 1: Parameter settings applied in the numerical simulations.

Default parameters			
h_{t}	15 m	$h_{\mathrm{r,max}}$	20 m
$h_{\mathrm{r,min}}$	1 m	f	6 GHz
R	-0.9	σ	0
β	1	r_{e}	8500 km
N	4	-	-

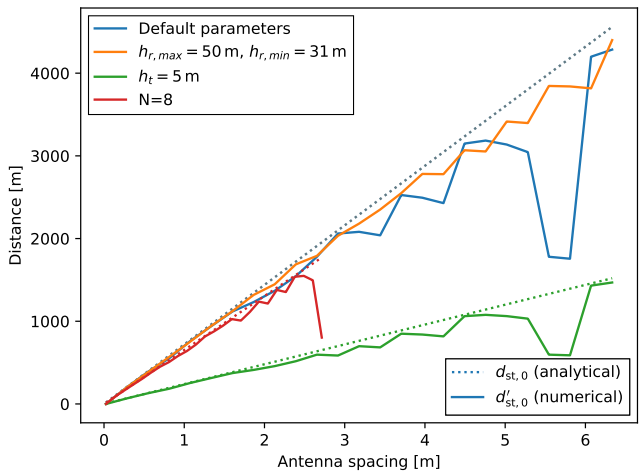

Figure 2: Comparison between $d_{\mathrm{st},0}$ and $d'_{\mathrm{st},0}$ as a function of Δh. Note that the dotted blue and orange lines overlap.

other typical parameter values used in simulations and calculations can be found in Table 1 unless specified otherwise.

The numerical values ($d'_{\mathrm{st},0}$ and $d'_{\mathrm{end},0}$) and the analytical approximations ($d_{\mathrm{st},0}$ and $d_{\mathrm{end},0}$) are plotted as function of Δh in Figs. 2 and 3, respectively. Regarding to our numerical search, we set the received antenna heights as follows

$$h_{\mathrm{r},n} = h_{\mathrm{r,max}} - n\Delta h\,, \quad n = 0, \ldots, N-1. \tag{4.1}$$

It can be observed from Fig. 2 and Fig. 3 that the analytical values are a good approximation of the numerical values when the antenna spacing is small. When the spacing increases, the discrepancy of the approximation becomes larger. However, both the corresponding numerical and analytical curves follow the same trend. It can also be observed from Fig. 2 that the analytical value for $d_{\mathrm{st},0}$ acts as an upper bound for $d_{\mathrm{st},0}$. Likewise, Fig. 3 shows that the analytical values appears to be a valid lower bound if antenna spacing is relatively small. However, if d'_{end} exceeds the distance where the effect of earth curvature cannot be

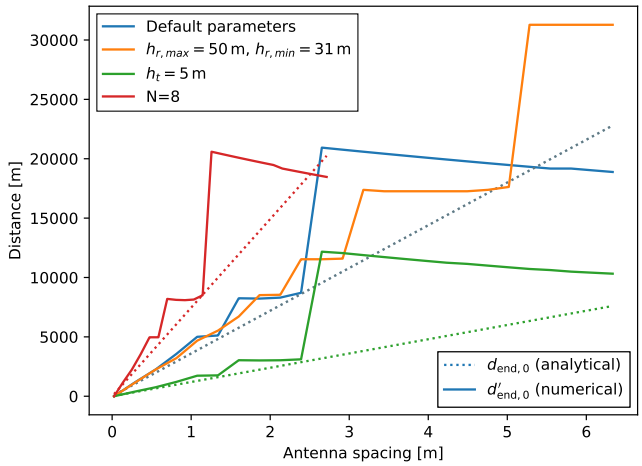

Figure 3: Comparison between $d_{\mathrm{end},0}$ and $d'_{\mathrm{end},0}$ as a function of Δh. Note that the dotted blue and orange lines overlap.

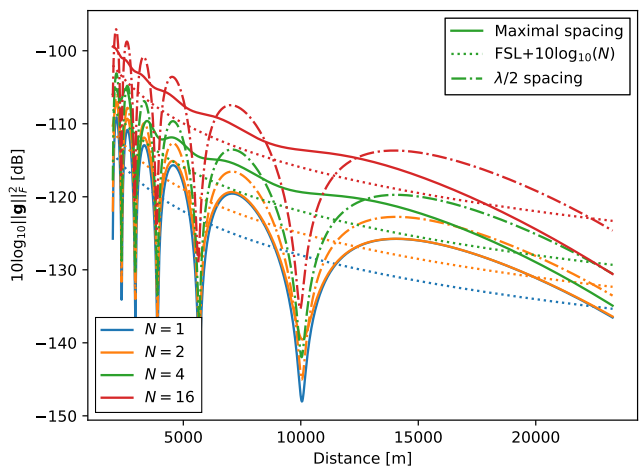

Figure 4: Performance comparison of maximally spaced array with an $\lambda/2$ spaced array.

ignored, the analytical bound may lose some accuracy. That is why solid lines may cross the dotted line at Fig. 3. In addition, jumps of numerical values in Figs. 2 and 3 can also be noticed as Δh increases. We can interpret those jumps as one more fading dip has been sufficiently mitigated, so that the range gets a further extension until next fading dip. The jumps will get larger as the antenna spacing increases because the gap between two consecutive fading dips grows as well as the distance d increases, which can also be observed in Fig. 4.

We calculate and plot the total channel gain $||\mathbf{g}||_F^2$ regarding two different antenna configurations (maximal spacing and $\lambda/2$ spacing) in Fig. 4 and compare with the free-space propagation scenario. It can be observed from Fig. 4 that a deep fading occurs under both configurations if just two antennas are equipped at the BS side. However, if the BS has four or even more antennas, our proposed maximal spacing configuration clearly outperforms the traditional $\lambda/2$ spacing antenna deployment scheme. As illustrated in Fig. 4, fading dips are well mitigated with maximal antenna spacing while a 20 dB fading dip still occurs if the antenna spacing is set as half wavelength. Even though there exists a deep fade at around 3000 m if four antennas with maximal spacing scheme are utilized, this should not be considered as a drawback since the distance lies outside the communication range because $d_{\mathrm{st},0} \approx 4500\,\mathrm{m}$. Moreover, if the antenna number is further increased to 16, the fading dip vanishes and $d_{\mathrm{st},0}$ decreases as well. Finally, note that the solid line is always above the dotted line, except for one deep fade mentioned before. *This means that the proposed maximal antenna spacing scheme results in a better system performance than a system in a free space scenario as we manage to leverage the constructive interference from the sea surface reflection while mitigating the destructive interference.*

5 Conclusion

In this paper, we have investigated how a vertical linear array at a base station in a maritime environment should be configured to mitigate deep fades caused by the coherent sea surface reflection. We assessed the extent of the range wherein the deep fades are sufficiently mitigated. Specifically, we derived closed-form expressions for the bounds of the start and end distance of this range, and provided an evaluation through numerical simulations. We found that the farthest end of the range extends significantly as the space between the antennas increases, irrespective of the offset of the array above sea level. Considering the physically constrained size of the base station array, we propose to maximize the spacing

between antennas. Employing this scheme, we found that four antennas are sufficient to obtain greater performance within a large range compared to a free space communication scenario. Moreover, further increasing the number of antennas in this scheme also reduces the starting-point distance of the communication range.

Acknowledgment

The authors gratefully acknowledge the support of Ericsson AB for partially funding this work.

Appendix

In accordance with the geometry in Fig. 1, h'_{t} can be expressed as

$$h'_{\mathrm{t}} = \sin\beta\sqrt{h_{\mathrm{t}}^2 + l_{\mathrm{t}}^2}. \tag{5.1}$$

Utilizing the *law of cosines* we can obtain that

$$\cos\gamma = \frac{2h_{\mathrm{t}}r_e - l_{\mathrm{t}}^2}{-r_e\sqrt{h_{\mathrm{t}}^2 + l_{\mathrm{t}}^2}}. \tag{5.2}$$

Since $\beta = \gamma - \frac{\pi}{2}$, $\sin\beta = -\cos\gamma$, we can further rearrange (5.1) as

$$h'_{\mathrm{t}} = h_{\mathrm{t}} - \frac{l_{\mathrm{t}}^2}{2r_e} \tag{5.3}$$

Furthermore, we assume that $\dfrac{l_{\mathrm{t}}}{h_{\mathrm{t}}} \approx \dfrac{l_{\mathrm{r}}}{h_{\mathrm{r}}}$ and $l_{\mathrm{t}} + l_{\mathrm{r}} \approx d$, therefore l_{t} can be approximated as

$$l_{\mathrm{t}} \approx \frac{h_{\mathrm{t}}d}{h_{\mathrm{r}} + h_{\mathrm{t}}} \tag{5.4}$$

Considering this approximation, we can reach the final result for h'_{t} and h'_{r} in (2.3) and (2.4).

References

[1] Y. Karasawa and T. Shiokawa, "Space and frequency correlation characteristics of L-band multipath fading due to sea surface reflection," *Electronics and Communications in Japan (Part I: Communications)*, vol. 68, no. 12, pp. 66–75, 1985.

[2] Y.-M. Le Roux, J. Ménard, C. Toquin, J.-P. Jolivet, and F. Nicolas, "Experimental measurements of propagation characteristics for maritime radio links," in *2009 9th International Conference on Intelligent Transport Systems Telecommunications, (ITST)*, Oct. 2009, pp. 364–369.

[3] F. Dong and Y. H. Lee, "Experiment results of a two-by-two diverse antenna system over sea surface in NLOS scenario," in *Proceedings of the 2012 IEEE International Symposium on Antennas and Propagation*, Jul. 2012, pp. 1–2.

[4] I. Ahmad and K. Chang, "Analysis on MIMO transmit diversity and multiplexing techniques for ship ad-hoc networks under a maritime channel model in coastline areas," in *2017 International Conference on Information and Communication Technology Convergence (ICTC)*, Oct. 2017, pp. 945–947.

[5] K. Karlsson, J. Carlsson, M. Olbäck, T. Vukusic, R. Whiton, S. Wickström, G. Ledfelt, and J. Rogö, "Utilizing two-ray interference in vehicle-to-vehicle communications," in *The 8th European Conference on Antennas and Propagation (EuCAP 2014)*, Apr. 2014, pp. 2544–2547.

[6] J. Naganawa, K. Morioka, J. Honda, N. Kanada, N. Yonemoto, and Y. Sumiya, "Antenna configuration mitigating ground reflection fading on airport surface for AeroMACS," in *2017 IEEE Conference on Antenna Measurements Applications (CAMA)*, Dec. 2017, pp. 91–94.

[7] C. Beard, "Coherent and incoherent scattering of microwaves from the ocean," *IRE Transactions on Antennas and Propagation*, vol. 9, no. 5, pp. 470–483, Sep. 1961.

[8] A. R. Miller, R. M. Brown, and E. Vegh, "A new derivation for the rough surface reflection coefficient and for the distribution of sea wave elevations," *NASA STI/Recon Technical Report N*, vol. 84, p. 17453, Sep. 1983.

[9] D. Freund, N. Woods, H.-C. Ku, and R. Awadallah, "Forward Radar propagation over a rough sea surface: a numerical assessment of the Miller-brown approximation using a horizontally polarized 3-GHz line source," *IEEE Transactions on Antennas and Propagation*, vol. 54, no. 4, pp. 1292–1304, Apr. 2006.

[10] K. Yang, A. F. Molisch, T. Ekman, and T. Roste, "A deterministic round earth loss model for open-sea radio propagation," in *2013 IEEE 77th Vehicular Technology Conference (VTC Spring)*. IEEE, Jun. 2013.

[11] K. Yang, A. F. Molisch, T. Ekman, T. Røste, and M. Berbineau, "A Round Earth Loss Model and Small-Scale Channel Properties for Open-Sea Radio Propagation," *IEEE Transactions on Vehicular Technology*, vol. 68, no. 9, pp. 8449–8460, Sep. 2019.

[12] W. Wang, G. Hoerack, T. Jost, R. Raulefs, M. Walter, and U.-C. Fiebig, "Propagation channel at 5.2 GHz in baltic sea with focus on scattering phenomena," in *2015 9th European Conference on Antennas and Propagation (EuCAP)*, Apr. 2015, pp. 1–5.

[13] A. Goldsmith, *Wireless Communications*. Cambridge University Press, 2005.

[14] J. C. Schelleng, C. R. Burrows, and E. B. Ferrell, "Ultra-short wave propagation," *The Bell System Technical Journal*, vol. 12, no. 2, pp. 125–161, Apr. 1933.

[15] ITU-R Recommendation P.526-15, "Propagation by diffraction," Oct. 2019.

Measurement-Based Wideband Maritime Channel Characterization

Paper II

Michiel Sandra, Guoda Tian, Aleskei Fedorov, Xuesong Cai, Anders J Johansson

Published as: M. Sandra, G. Tian, A. Fedorov, X. Cai, A. J. Johansson, "Measurement-Based Wideband Maritime Channel Characterization," *2023 17th European Conference on Antennas and Propagation (EuCAP)*, Florence, Italy, 2023.

Abstract

Maritime communication is one of the 5G vertical domains and is attracting more attention. Advanced channel models that accurately characterize the wideband maritime propagation channels are essential for the development of modern maritime communication technologies. To this end, we measured the propagation channel at 5.6 GHz with a sailing boat, capturing the channel with a bandwidth of 250 MHz, both in the harbor and the open sea. Based on the measurement results, we evaluated the Rician K-factor, coherence bandwidth and path loss. We concluded that in the maritime environment various types of power delay profiles can occur, and that the Rician K-factor and coherence bandwidth can vary significantly within a short period of time.

1 Introduction

Maritime radio systems such as Very High Frequency (VHF) and satellite communications have been playing a vital role in maritime activities in the last hundred years, especially for navigation and safety purposes. Nevertheless, those radio system are limited in capacity due to the limited total bandwidth of each satellite to share between users, and the very narrow bandwidth for VHF systems. Hence, there is a great interest to provide wireless services through land-based base stations for vessels in the coastal area. However, modern wireless systems are not optimized for the maritime environment. Therefore, maritime communication has been selected as one of the 5G vertical domains since 3GPP Release 16 [1]. The 3GPP standardization team aims at optimizing 3GPP systems to cover the maritime environment, which could enable a large number of novel maritime wireless applications such as high-speed internet on vessels, surveillance, video streaming, improved search and rescue services, pilotage service, modern safety equipment, smart buoys, etc. Those applications require robust wireless technology with high data rates and high reliability. To fulfill those requirements, it is of necessity to measure maritime propagation channel to first attain a good knowledge of maritime channel properties and then establish an accurate and realistic channel model.

A large number of measurements of the maritime propagation channel can be found in radar literature, see [2] and the references therein. From [2], it is clear that propagation modeling at sea is still an active research area. However, only few measurements and investigations have been conducted under maritime scenarios with modern wireless communications in mind. For example, [3] and [4] investigated the path loss and small-scale fading statistics at 2 GHz with a 20 MHz bandwidth. In addition, [5, 6] conducted channel measurements with 100 MHz

bandwidth, and also investigated the small-scale fading statistics. Those measurements concluded that a two-ray model considering the curvature of Earth can be used to model the path loss, and that the small-scale fading is mainly Rician distributed. With the aim of gaining additional insight into the propagation channel at sea, we conducted a measurement at 5.6 GHz with 250 MHz bandwidth, where we recorded User Equipment (UE) positions and their corresponding propagation channels over one hour. The trajectory of UE covered both harbor and open-sea environment, which enables us to compare different channel propagation scenarios. The rest of this paper is organized as follows. In Section II, we introduce the measurement campaign and setup. The processing procedure of the measurement data is presented in Section III. Section IV describes the measurement results, followed by interpretations and discussions. Section V concludes the paper.

2 Measurement campaign and setup

The measurement campaign took place in September 2022 in Klagshamn, Sweden (N 55.523° E 12.895°). The transmit antenna was mounted on top of a 22-foot sailing boat which acted as UE. The UE transmitted a sounding signal every 5 ms, occupying 250 MHz bandwidth at 5.6 GHz. On the base station (BS) side, we installed another antenna, which had a clear view toward the sea, at the balcony of a small house located on the shore, as shown in Fig. 1. Both transmit and receive antennas are omni-directional, with a height of approximately 10 m and 7 m, respectively. We sailed the boat for slightly over one hour, which started and ended both at the harbor of Klagshamn. As shown in Fig. 2, the sailing trajectory covered both harbor and open-sea scenarios, with the largest distance from the boat to the seashore equal to approximately 3 km.

During the measurement campaign, we utilized the channel sounder presented in [7], which is based on the NI USRP X410, with the configuration of the parameters as summarized in Table 1. To enlarge the dynamic range of the sounding system, the channel sounder was equipped with an external power amplifier at the transmitter and an external low-noise amplifier at the receiver. During the measurement a Zadoff-Chu sounding signal was sent in the frequency domain and covered 4095 tones with a tone spacing of 61 kHz. The transmitter and receiver were synchronized through Global Navigation System (GPS), and the position of the transmitter was recorded with a Swift Navigation Duro GNSS receiver.

Figure 1: Base station antenna (Rx) with a clear view on the sea, and a sailing boat in the background which acts as UE (Tx).

Figure 2: Trajectory during the measurement campaign.

Table 1: Overview of the parameters of the channel sounder

Parameter	Value	Description
L	8192 samples	Sound signal length
P	49152 samples	Skipped samples due to propagation
M	64 signals	Average quantity
K	2 bits	Bit shift in averager
R	1975712 samples	Skipped samples until next snapshot
f	5.6 GHz	Center frequency
P_{Tx}	33 dBm	Output power
T_{rep}	5 ms	Channel measurement repetition
T_s	2 ns	Sample period

3 Data processing

Let us denote the time-varying channel transfer function as $H(n;t)$, where $n \in [1, \cdots, 4095]$ indicates the index of the subcarriers/tones. H is measured as

$$H(n;t) = \frac{Y(n;t)}{X(n)} \tag{3.1}$$

where Y and X denote the received and transmitted signals respectively in the frequency domain. The time-varying channel impulse response (CIR) $h(\tau;t)$ is then calculated by performing inverse Fourier transform to $H(n;t)$.

The underlying signal model of $h(\tau;t)$ is expressed as

$$h(\tau;t) = \sum_{\ell=1}^{L(t)} \alpha_\ell(t)\delta(\tau - \tau_\ell(t)), \tag{3.2}$$

where $\alpha_\ell(t)$ and $\tau_\ell(t)$ indicate the time-varying complex amplitude and delay of the ℓ-th multipath component (MPC), respectively, and $L(t)$ is the number of the MPCs observed for the snapshot at time instant t. The channel parameters to be estimates are $\mathbf{\Theta} = [\alpha_\ell(t), \tau_\ell(t); \ell = 1, \cdots, L(t), t = t_1, \cdots, t_M]$ with M being the number of measurement snapshots in the measurement. We apply the space-alternating generalized expectation-maximization (SAGE) algorithm to estimating $\mathbf{\Theta}$ in this work. Readers are referred to [8] for more details about the SAGE principle.

4 Results and discussion

4.1 Power delay profiles and frequency selectivity

We present the measured time-varying power delay profiles (PDP) during the whole measurement campaign in Fig. 3. To visualize the PDP more clearly, we also select three positions along the trajectory and plot the corresponding PDPs in Fig. 4. With the aid of SAGE estimation algorithms, the 30 most dominant MPCs are identified, after which the MPCs with a relative power greater than -50 dB are selected. As shown in Fig 3, many MPCs with strong powers were presented up to 300 seconds, where there are many other boats and small houses acting as scatterers that contribute to the multipath propagation. When the boat leaves the harbor, a considerable number of multipaths can still be observed,

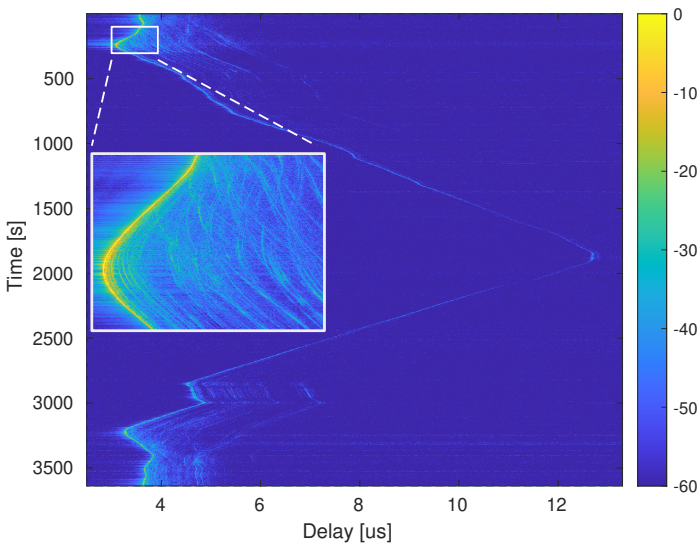

Figure 3: Power delay profile during the measurement.

resulting in around two clusters plus several strong discrete MPCs. For the open-sea scenario presented in Fig. 4, it can be observed that the number of MPCs and the delay spreads are significantly reduced. Nevertheless, owing to the large measurement bandwidth, approximately 10 MPCs could still be observed. We postulate that this is due to the local scatterers around the transmitter and/or receiver and scattering from the sea surface.

To gain insight into the frequency selectivity of the channel, we reconstruct the channel frequency responses utilizing the MPCs identified by the SAGE algorithm in the three scenarios, which are shown in Fig. 5. It can be observed from Fig. 5 that the channel response varies only approximately 6 dB across more than 100 MHz inside the harbor. In comparison, clear frequency selectivity appears when the UE is leaving the harbor due to the contribution of the second cluster as well as strong MPCs approximately after 2000 ns. When we sail further away from the harbor and enter the open sea, the propagation channel still shows frequency selectivity. Due to the absence of the second cluster and strong isolated components, a smoother response across the frequency spectrum is observed compared to the second scenario. Additionally, the coherence bandwidth is calculated for the first 900 seconds of the measurement, and is illustrated in Fig. 6. We can observe a wide coherence bandwidth during the first 300 seconds, which resembles the harbor scenario. While UE moves away from the harbor, wide and narrow coherence bandwidths appeared alternately from 300 to 900 seconds.

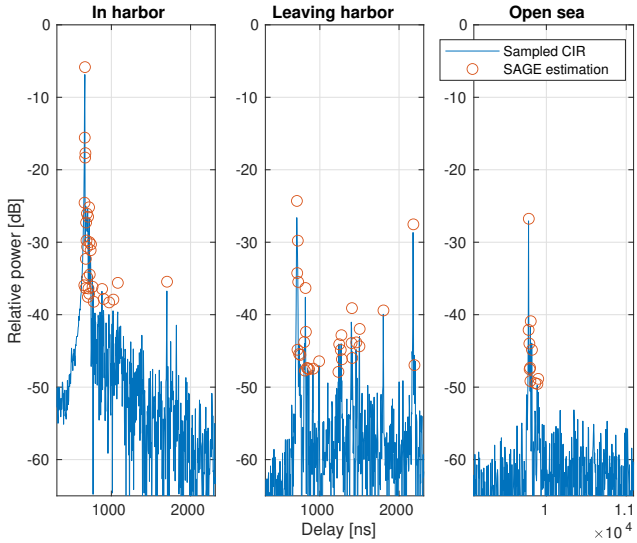

Figure 4: Examples of the power delay profiles.

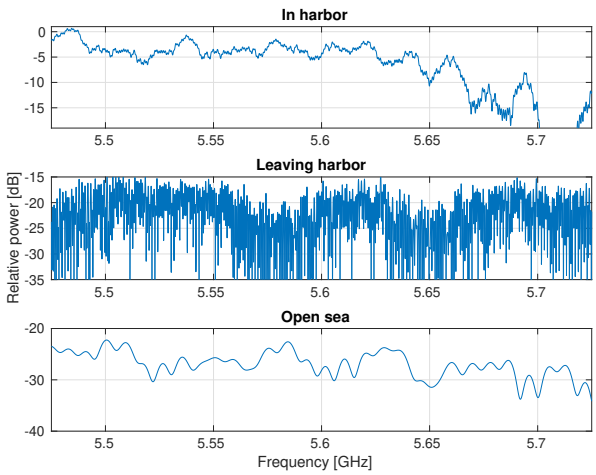

Figure 5: Examples of the channel frequency responses.

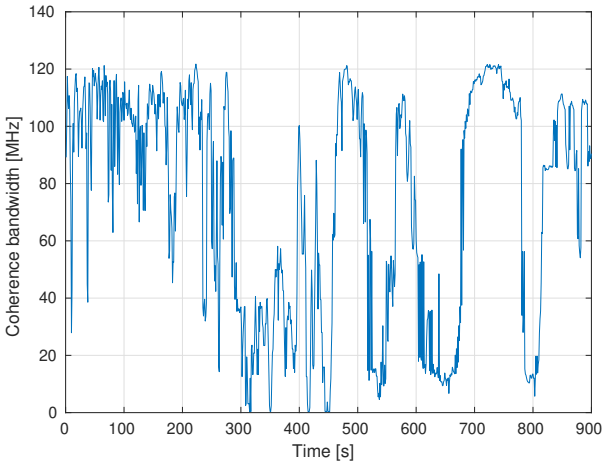

Figure 6: Coherence bandwidth.

4.2 Received power and path loss

In Fig. 7, the relative receiver power and the compass heading of the sailing boat are depicted as a function of the measurement time. Throughout the measurement, one can observe significant reduction of received power as the distance between UE and BS increases. The boat's heading strongly influences the received power, which is presented at 2000 seconds. The boat's body and mast likely had a large impact on the radiation pattern of the antenna.

We plot the measured and theoretical two-ray model path loss, see [4, 6, 9], as a function of distance in Fig. 8. According to Fig. 8, they agree well with each other on larger distances, i.e. in the open sea. Note that we have calculated the path loss using the relative power. In addition, we have not taken the antenna gain into account because we could not obtain a reliable measure of the antenna gain due to the effect of the boat on the radiation pattern antenna, as described above. This could also be an explanation for the outliers at 500 m and 3000 m, where the boat changed direction.

4.3 Small-scale fading

The Rician K-factors are calculated using the moment-based method [10] according to the measured channel powers within time windows of two seconds and shown in Fig. 9. It can be observed that the K factor can change rapidly over time. Note that the Rician K-factor at 1500 seconds is quite small, which is

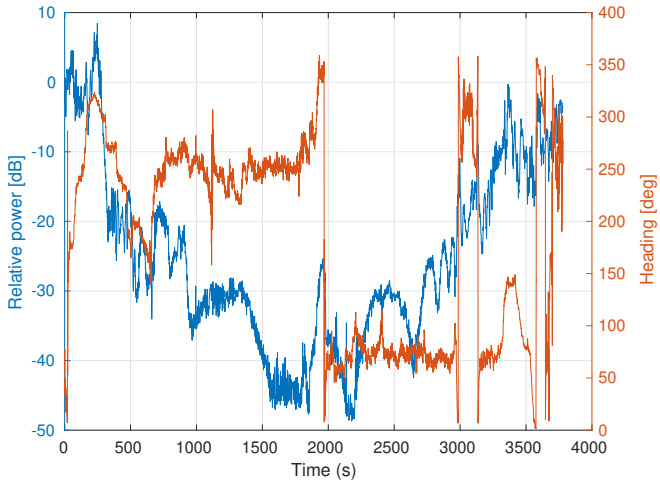

Figure 7: Receiver power variation and heading of the boat throughout the measurement.

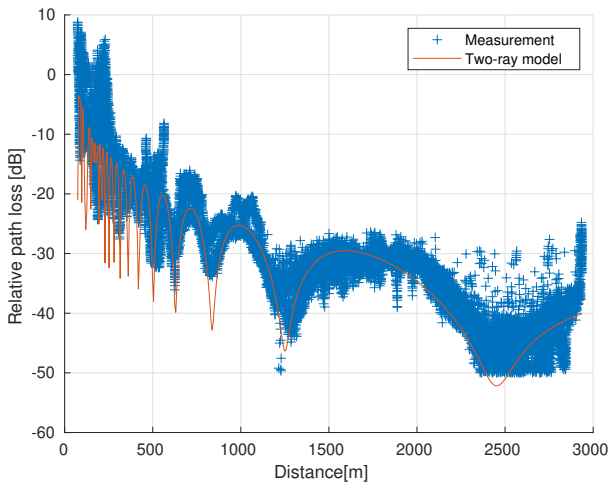

Figure 8: Path loss.

due to the destructive interference between the line-of-sight component and the reflection from the sea surface.

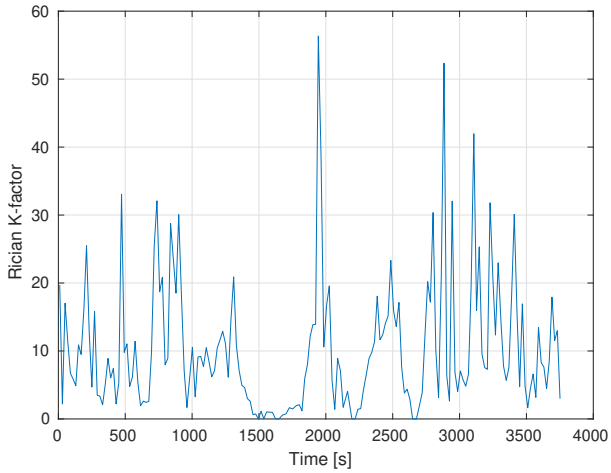

Figure 9: Rician K-factor.

5 Conclusion

We have conducted a measurement campaign at 5.6 GHz in a maritime environment, capturing the propagation channel in a harbor as well as in an open sea, with a bandwidth of 250 MHz. Our results show that within the maritime environment, various types of delay profiles can occur. We found that characteristics such as the Rician K-factor and coherence bandwidth can vary greatly over tens of seconds. This poses challenges for the wireless system design, and therefore further modeling of the effects shown by this measurement is necessary. Future work includes a thorough investigation of the dynamic properties of the channel. In addition, measurements will be conducted with multiple antennas to further characterize the channel in the spatial domain.

6 Acknowledgment

The authors would like thank Junshi Chen for the support during the measurement campaign. Additionally, the authors gratefully acknowledge the support of Ericsson. The work of Xuesong Cai is also supported by the Horizon Europe

Framework Programme under the Marie Skłodowska Curie grant agreement No. 101059091.

References

[1] 3GPP, "Technical Specification Group Services and System Aspects; Feasibility Study on Maritime Communication Servicesover 3GPP system; Stage 1 (Release 16)," 3rd Generation Partnership Project (3GPP), Technical Specification (TS) 22.819, Dec. 2018, version 16.2.0.

[2] A. Danklmayer, J. Förster, V. Fabbro, G. Biegel, T. Brehm, P. Colditz, L. Castanet, and Y. Hurtaud, "Radar Propagation Experiment in the North Sea: The Sylt Campaign," *IEEE Transactions on Geoscience and Remote Sensing*, vol. 56, no. 2, pp. 835–846, Feb. 2018.

[3] K. Yang, T. Roste, F. Bekkadal, K. Husby, and O. Trandem, "Long-Distance Propagation Measurements of Mobile Radio Channel over Sea at 2 GHz," in *2011 IEEE Vehicular Technology Conference (VTC Fall)*, Sep. 2011, pp. 1–5, iSSN: 1090-3038.

[4] K. Yang, A. F. Molisch, T. Ekman, T. Røste, and M. Berbineau, "A Round Earth Loss Model and Small-Scale Channel Properties for Open-Sea Radio Propagation," *IEEE Transactions on Vehicular Technology*, vol. 68, no. 9, pp. 8449–8460, Sep. 2019.

[5] W. Wang, R. Raulefs, T. Jost, A. Dammann, C. Gentner, and S. Zhang, "Ship-to-land broadband channel measurement campaign at 5.2 GHz," in *2014 Oceans - St. John's*, Sep. 2014, pp. 1–8, iSSN: 0197-7385.

[6] W. Wang, G. Hoerack, T. Jost, R. Raulefs, M. Walter, and U.-C. Fiebig, "Propagation channel at 5.2 GHz in baltic sea with focus on scattering phenomena," in *2015 9th European Conference on Antennas and Propagation (EuCAP)*, Apr. 2015, pp. 1–5.

[7] M. Sandra, C. Nelson, and A. J. Johansson, "Ultrawideband usrp-based channel sounding utilizing the rfnoc framework," in *2022 IEEE Conference on Antenna Measurements and Applications (CAMA)*, 2022.

[8] B. Fleury, M. Tschudin, R. Heddergott, D. Dahlhaus, and K. Ingeman Pedersen, "Channel parameter estimation in mobile radio environments using

the SAGE algorithm," *IEEE Journal on Selected Areas in Communications*, vol. 17, no. 3, pp. 434–450, Mar. 1999.

[9] M. Sandra, G. Tian, X. Cai, and A. J. Johansson, "Antenna Array Configuration for Reliable Communications in Maritime Environments," in *2022 IEEE 95th Vehicular Technology Conference: (VTC2022-Spring)*, Jun. 2022, pp. 1–5, iSSN: 2577-2465.

[10] L. Greenstein, D. Michelson, and V. Erceg, "Moment-method estimation of the ricean K-factor," *IEEE Communications Letters*, vol. 3, no. 6, pp. 175–176, 1999.

A Wideband Distributed Massive MIMO Channel Sounder for Communication and Sensing

Paper III

Michiel Sandra, Christian Nelson, Xuhong Li, Xuesong Cai,
Anders J Johansson

Published as: M. Sandra, C. Nelson, X. Li, X. Cai, A. J. Johansson, "A Wideband Distributed Massive MIMO Channel Sounder for Communication and Sensing," *IEEE Transactions on Antennas and Propagation*, 2025.

Abstract

Channel sounding is a vital step in the design and deployment of wireless communication systems. In this paper, we present the design and implementation of a coherent distributed massive MIMO channel sounder operating at 5-6 GHz with a bandwidth of 400 MHz based on the NI USRP X410. Through the integration of multiple transceiver chains and RF switches, the design facilitates the use of a larger number of antennas without significant compromise in dynamic capability. Our current implementation is capable of measuring thousands of antenna combinations in tens of milliseconds. Every radio frequency switch is seamlessly integrated with a 16-element antenna array, allowing phase-coherent multi-node dual-polarized double-directional dynamic channel measurements for multistatic integrated sensing and communication (ISAC) applications. In addition, the channel sounder features real-time processing to reduce the data stream to the host computer and increase the signal-to-noise ratio. The correct operation of the sounder is demonstrated through two measurements in an indoor laboratory environment. The first measurement entails a single antenna robot as transmitter and 128 distributed receiving antennas. The second measurement demonstrates a passive sensing scenario with a walking person. We evaluate the results of both measurements using the super-resolution algorithm SAGE. The results demonstrate the great potential of the presented sounding system for providing high-quality radio channel measurements, contributing to high-resolution channel estimation, characterization, and active and passive sensing in realistic and dynamic scenarios.

1 Introduction

Coherent transmission and reception with a massive number of distributed antennas is the foundation of emerging technologies such as distributed massive multiple-input multiple-output (MIMO) and cell-free massive MIMO [1–8]. These technologies have the potential to enhance capacity, reliability, localization accuracy, and sensing capability. Expanding the number of antennas raises the upper limit on the spatial degrees of freedom of the channel, which could lead to a significant increase in capacity and to higher diversity orders. Compared to conventional MIMO with antennas in a compact area, separating or distributing the antennas also makes the system less prone to large-scale fading effects. The distributed nature of the antennas also opens up more opportunities to use the multi-static channel information for ISAC applications, which is one of the six use cases in 6G [9].

In order to propose practical solutions and evaluate the system's performance, it is essential to attain a thorough understanding of the distributed massive MIMO channels. Consequently, a channel sounder needs to be designed that can capture the real-world propagation characteristics. The channel sounder should

Table 1: State-of-the-art sub-6 GHz channel sounders for distributed MIMO

Reference	Type	Multi-node	Antenna comb.	Snapshot time (ms)	Bandwidth (MHz)
[12]	parallel	✓	3	0.5	150
[13]	parallel	✓	2112	1350	40
[14]	parallel		64	710	50
[15]	parallel		32	510	80
[16]	parallel		36	unknown	2.5
[11]	parallel	✓	78	5	40
[17]	parallel		64	1	115
[18]	parallel		768	1	20
[19]	switched		832	85	40
[20]	switched/virtual		4096	N/A	400
[21]	switched/virtual		64	N/A	100
Our work	**parallel/switched**	✓	**7168**	**71**	**400**

have a large number of antennas that can be flexibly distributed, a large bandwidth to obtain high delay resolution, and a high snapshot rate to characterize dynamic scenarios. It is also imperative that a channel sounder is cost-effective in its implementation and easy to deploy in various scenarios. While these requirements are generally applicable to most channel sounders, with the advent of ISAC and D-MIMO, the propagation channels among different base station (BS) antennas, besides the traditional BS-user links, has become increasingly important to be understood. For example, in distributed MIMO systems, channel state information between distributed BS antennas can facilitate calibration procedures that allow coherent transmission and reception [10]. Similarly, in ISAC, such channel information can be used to detect changes in the environment without a user, i.e. passive sensing. Therefore, the channel sounder must be capable of measuring the channels between all combinations of antennas in the system, also known as multi-node channel sounding [11–13]. This feature enables *multistatic* sensing applications.

The existing landscape of channel sounders in the sub-6 GHz band for distributed MIMO is given in Table 1. They can be categorized according to the way they employ multiple antennas: *i)* parallel transceiver chains, *ii)* employing radio frequency (RF) switches or *iii)* through the virtual array principle. The channel sounders presented in [12–18,22–25] feature one transmitter and/or receiver chain per antenna. This strategy allows to measure channels on the order of a millisecond; however, the cost scales linearly with the number antennas, data handling issues can arise from the substantial data generated by the RF chains and there is a risk that the sounder becomes cumbersome and unwieldy. In addition, it can be challenging to perform phase calibration of transceiver chains, which is needed for angle-of-departure (AoD) and angle-of-arrival (AoA) estimation. However, a solution was presented in [17] utilizing a custom-made calibration unit. Channel sounders employing the switched array principle, e.g. [11, 19–21, 25], can address

these drawbacks. However, they must compromise on the dynamic capability. Furthermore, the integration of parallel RF channels with RF switches, as shown in [25], presents a viable trade-off solution. Channel sounders that employ the virtual array principle [19–21] – a convenient and cost-effective method to measure the channel with an immense number of antennas lack dynamic capability. In addition to the three categories mentioned above, another approach for channel sounding is beam switching, as described in [26, 27]. This technique, like RF switches, allows for rapid selection between different antenna states and shares similar advantages. However, unlike RF switches, where the beams correspond to the radiation pattern of individual antenna elements, beam switching generates beams through a linear combination of the patterns of all antenna elements in the phased array. To the best of our knowledge, beam switching has not yet been applied in sub-6 GHz channel sounders.

The bandwidth of a channel sounder is limited by the underlying RF equipment. Channel sounders based on a vector network analyzer (VNA) [20] can have a bandwidth of the order of several GHz. However, VNAs measure the channel much slower than other solutions, and hence limit the dynamic capability. Therefore, many channel sounders are based on software-defined radios (SDRs) [13, 17, 18, 23, 24, 28] such as the USRP series from NI, and custom designs [15, 19, 25, 29]. In contrast to custom-designed channel sounders [25, 29], SDRs can offer a complete radio system without a high development cost. Naturally, the bandwidth of the channel sounder is limited by the specifications of commercially available state-of-the-art SDRs. One also has to consider the data rate between an SDR and the host computer, which can easily become several gigabytes per second in (ultra)wideband setups. When bandwidth is increased, real-time processing on the SDR might be needed to reduce the data rate between the SDR and the host computer.

To the best of our knowledge, a dynamic channel sounder that combines multi-node capability with a large number of antennas and a very large bandwidth has not previously been presented in the literature. Such a channel sounder opens up opportunities to enhance distributed MIMO channel models, phase calibration techniques, localization techniques, or multistatic ISAC algorithms. To fill this gap, we present the design, implementation, and verification of a scalable multi-node distributed massive MIMO channel sounder operating in the 5−6 GHz range with an instantaneous bandwidth up to 400 MHz based on the NI USRP X410. By operating in the unlicensed 5-GHz band, we are able to utilize a large bandwidth with a higher allowed transmit power than the unlicensed UWB

bands. The larger bandwidth and higher signal-to-noise ratio (SNR) are crucial for high-resolution channel estimation, which leads to a better ability to model and understand the propagation channel for communication and sensing. The main contributions of this work are:

- We achieve state-of-the-art performance in the time, frequency and spatial domains *simultaneously*. A performance comparison of our channel sounder with the state-of-the-art is given in Table 1.
- Through the integration of both parallel RF chains and RF switches, we facilitate the utilization of a larger number of antennas without significant compromise in dynamic capability. Every RF switch is seamlessly integrated with a dual-polarized 2×4 antenna array within a single panel. This enables dynamic phase-coherent *multi-node* dual-polarized double-directional channel measurements, which is the unique feature of our channel sounder over the state-of-the-art and key-enabler for *multistatic* radar or ISAC measurements. This integration also streamlines the calibration process in an anechoic chamber, guaranteeing phase coherency among the co-located antennas.
- The correct operation of the channel sounder is demonstrated by two sample measurements in an indoor laboratory environment. The two measurements are tailored for a communication application and a sensing application, respectively, where the potential of distributed MIMO for the two cases is also well demonstrated.

In order to achieve the state-of-the-art performance, we have addressed the high data rate problem, due to the 400 MHz bandwidth, with real-time processing on the field-programmable gate array (FPGA) by selecting and averaging sounding frames. As a result, we realize high processing gains without increasing the data rate between the USRP and the host computer. Besides that, custom FPGA design is also required for correct time division duplex (TDD) and RF switch control, ensuring phase-coherent operation. We provide a comprehensive description of the implementation of the channel sounder, which is based on the open-source RFNoC framework. The codes are made available on GitHub [30]. Our comprehensive description contributes towards the *reproducibility* of channel sounders and channel measurements within the scientific community, and can save a significant amount of time for those who want to build a similar system. An early version of the channel sounder, which could only measure a simple single-input single-output link, has been presented in [31].

The remainder of the paper is organized as follows. Sect. 2 discusses design and implementation of the channel sounder. Sect. 3 elaborates on the post-processing and calibration aspects. In Sect. 4, the two sample measurements and the results that demonstrate the capability of the sounder and the potential of distributed MIMO in communication and sensing are included. Finally, conclusive remarks are summarized in Sect. 5.

Notations: Throughout this paper, italic letters are used to represent scalars. Bold lowercase letters are for vectors and bold uppercase letters for matrices or tensors. The vector denoted as $\mathbf{1}$ consists of elements that are all equal to one and has proper length. $(\cdot)^{\mathrm{T}}$ indicates matrix transposition, $\mathrm{j} = \sqrt{-1}$, $\mathrm{Tr}(\cdot)$ denotes the trace operator, and $\otimes$ represents Kronecker product. $|\cdot|$ and $\angle$ denote the absolute value and the argument of a complex number, respectively. In addition, $\max\{\cdot\}$ and $\mathrm{sum}\{\cdot\}$ denote the maximum value and the sum of all the elements in a vector, respectively.

2 Design and Implementation

2.1 High-level Design

Fig. 1 presents a basic block diagram of the channel sounder. The core components include one or more NI USRP X410 and a host computer. Optionally, a Rubidium clock, Global Positioning System (GPS) antenna, and an RF switch can be integrated into the setup. The NI USRP X410 is a four-channel full-duplex SDR. It has a tunable center frequency ranging from 1 MHz to 7.2 GHz and supports instantaneous bandwidths up to 400 MHz. This device uses the Xilinx Ultrascale+ RFSoC ZU28DR FPGA, for which we developed custom code. We implemented channel sounding functions using a custom signal processing block within the RF network on chip (RFNoC) open source framework that manages the streaming and processing of RF data on the FPGA. It also allows for the design of custom applications with RFNoC blocks. Our processing block can selectively average received samples, optimizing the data stream to the host computer and improving the SNR.

The Rx and Tx chains are connected to the same port through an internal RF switch which is controlled in real time by our custom block. This means that the respective port can transmit or receive, but not both at the same time. The following principle applies: when one transmits, all the other transceiver chains in the channel sounder are receiving. Then, each port in the channel sounder

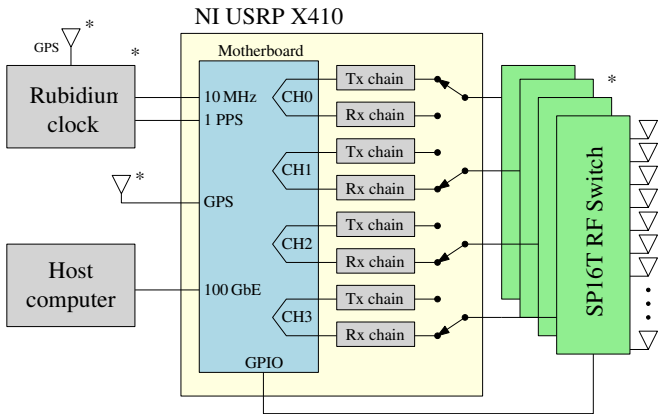

Figure 1: Simplified block diagram of the channel sounder. Components indicated with * are optional.

transmits after one another in a pre-configured order.

The USRP is connected to a host computer via an Ethernet interface. Depending on the data rate requirements between the host and the USRP, the 100 GbE interface or the 1 GbE interface can be utilized. Note that multiple USRPs can be connected to one host computer. Apart from the appropriate Ethernet interface, there is no strict hardware requirement for the host computer. However, the host computer must be fast enough to handle and store the stream of data from the USRP, which can vary from about 1 MB/s to hundreds of MB/s, depending on the configuration.

Rubidium clocks provide a stable time and frequency synchronization between two or more USRPs without the need for any cabling between them during the measurement, allowing for mobile measurements. However, note that the rubidium clocks have to be synchronized via a cable a few hours before the actual measurements. A rubidium clock can provide a level of frequency synchronization so that the phase difference between two clocks is stable throughout the measurement. If phase stability is not critical, sufficient synchronization can also be achieved with the built-in GPS disciplined oscillator in the sense that the sounder still works correctly, e.g. timing of the time division multiplexing (TDM) scheme. A center frequency offset (CFO) of several Hertz could occur and should be taken into account, if necessary.

The external RF switches allow for a cost-effective extension of the number of channels that can be measured, enhancing the spatial resolution of the propagation measurements. Their states are real-time and independently controlled by our custom RFNoC block through the general-purpose input/output (GPIO)

ports of the USRP. We have implemented the following TDM scheme to control the state of the switches. There are in total N_{RF} RF chains in the system, with $\mathbf{n}_{\mathrm{T}} \in \mathbb{N}^{N_{\mathrm{RF}} \times 1}$ containing the number of (switched) antennas connected to the RF chains in the transmission mode, and $\mathbf{n}_{\mathrm{R}} \in \mathbb{N}^{N_{\mathrm{RF}} \times 1}$ containing the number of switched channels for different RF chains in the receiving mode. Only one antenna is transmitting at a time. While one antenna is transmitting, the other antennas, except those connected to the same USRP port, are receiving and the RF switches are being switched until all channels have been measured. After that, the next antenna transmits, etc. The total number of channels that can be measured is

$$\mathbf{1}^{\mathrm{T}}(\mathbf{n}_{\mathrm{T}} \otimes \mathbf{n}_{\mathrm{R}}) - \mathrm{Tr}(\mathbf{n}_{\mathrm{T}}\mathbf{n}_{\mathrm{R}}^{\mathrm{T}}) \tag{2.1}$$

including reciprocal channels. The total *unique* number of channels is

$$\frac{1}{2}\,\mathbf{1}^{\mathrm{T}}(\mathbf{n}_{\mathrm{T}} \otimes \mathbf{n}_{\mathrm{R}}) - \frac{1}{2}\,\mathrm{Tr}(\mathbf{n}_{\mathrm{T}}\mathbf{n}_{\mathrm{R}}^{\mathrm{T}}). \tag{2.2}$$

Because of the simultaneous reception on different RF chains, the amount of time slots needed to measure all the antenna combinations is less than the amount of combinations. In our implementation, the total number of time slots it takes to measure the configured channels is $\max\{\mathbf{n}_{\mathrm{R}}\}\,\mathrm{sum}\{\mathbf{n}_{\mathrm{T}}\}$. At the time of writing, our implementation of the channel sounder contains three USRP X410, three host computers, three Rubidium clocks, and eight Mini-Circuits USB-1SP16T-83H SP16T RF switches. This makes it possible to measure to measure 7686 unique channels.

2.2 Elementary Sounding Frame

The principle of channel sounding is as follows: a known waveform is transmitted at the desired carrier frequency. On the receiver side, the received waveform is processed to obtain the channel transfer function and impulse response. This could be done for all antenna combinations to recover the directional properties of the channel. For the design of the channel sounding waveform, it is important that the waveform has a large bandwidth, a uniform power-spectral density, and high energy [32]. A large bandwidth allows us to achieve a high delay resolution, while the uniform power-spectral density allows us to estimate the channel across the whole bandwidth with the same quality. Higher power means a higher SNR. Since the peak power of the transmit power amplifier is limited, a high power implies that a low peak-to-average-power ratio (PAPR) of the sounding waveform

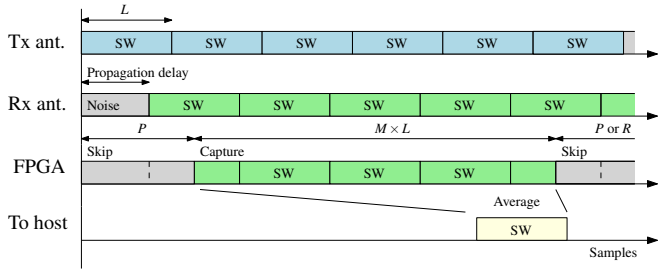

Figure 2: RFNoC processing block functionality for one channel snapshot. SW stands for sounding waveform.

should be used. It is convenient to resort to the frequency domain to design the sounding waveform as a multi-tone signal. Such a waveform, $\mathbf{s} \in \mathbb{C}^{L\times 1}$ with a length of L samples, can in discrete complex baseband be expressed as

$$\mathbf{s}(n) = \frac{1}{L}\sum_{k=0}^{L-1} \mathbf{x}(k)\exp\left(\mathrm{j}2\pi kn/L\right), \tag{2.3}$$

where $\mathbf{x} \in \mathbb{C}^{L\times 1}$ contains the complex amplitudes for all the tones. The entries of $\mathbf{x}$ can now be chosen so that $|\mathbf{x}(k)| = 1$ for the bandwidth of interest and $\angle\mathbf{x}(k)$ optimizes the PAPR. For our channel sounder, we choose a Zadoff-Chu sequence for $\mathbf{x}(k)$ since $|\mathbf{x}(k)| = 1$ and its (inverse) Fourier transform, if the sequence length is a prime number, is also a Zadoff-Chu sequence, which has good time-continuous PAPR and autocorrelation properties [33, 34].

During a single-channel snapshot, the respective transmitter sends multiple repetitions of the same sounding waveform $\mathbf{s}$ with a length of L samples, as illustrated in Fig. 2. Note that, to avoid aliasing, L should be longer than

$$L \geq \frac{\Delta\tau_{\max}}{T_{\mathrm{s}}}, \tag{2.4}$$

where $\Delta\tau_{\max}$ is the maximum delay difference between the first and last received multipath component, and T_{s} is the sample period. These signals then propagate through the radio channel and arrive at the receiver with an unknown propagation delay. Therefore, samples have to be discarded according to this propagation delay. Otherwise, a couple of samples will be averaged with noise, which reduces the signal-to-noise ratio. In addition, another $\frac{\Delta\tau_{\max}}{T_{\mathrm{s}}}$ samples have to be discarded, so the received sounding signals are the result of a circular convolution between the channel impulse response and the original sounding signal. In general, this is not a strict requirement, yet quite convenient for post-processing. At the beginning of each elementary sounding frame, the RF switches are also

configured for the respective antenna; this means that we also have to take into account the switching time of the RF switch. We define P as the total number of samples that are discarded and its value should be higher than

$$P \geq \frac{\tau_{0,\max} + \Delta\tau_{\max} + T_{\mathrm{sw}}}{T_{\mathrm{s}}}, \tag{2.5}$$

where $\tau_{0,\max}$ the maximum delay of the first multipath component, and T_{sw} is the maximum time it takes for RF switch to switch channel. The switching time also takes into account the delay of the cable from the GPIO output of the USRP to the RF switch. If RF switches are only used for receiving, then the requirement for P could be reduced,

$$P \geq \max\left(\frac{\tau_{0,\max} + \Delta\tau_{\max}}{T_{\mathrm{s}}}, \frac{T_{\mathrm{sw}}}{T_{\mathrm{s}}}\right). \tag{2.6}$$

In practice, P can be set higher than required to account for possible time synchronization errors between receiver and transmitter. After disregarding P samples, M waveforms of length L are captured and averaged, as illustrated in Fig. 2. Averaging is done by averaging each i^{th} sample of each received sounding signal. Let us represent the m^{th} received waveform as $\mathbf{y}_m \in \mathbb{C}^{L\times 1}$, where $m \in [1, M]$. Then the processed received waveform $\mathbf{y} \in \mathbb{C}^{L\times 1}$ becomes

$$\mathbf{y}(i) = \frac{1}{2^K} \sum_{m=1}^{M} \mathbf{y}_m(i), \tag{2.7}$$

where i indicates the i^{th} element of the vectors, and $K \in \mathbb{N}$ is the parameter for the division factor in the averager. This division is a power of two by design because this simplifies the logic design. The processed signal is then sent to the host for channel estimation and storage. In the meantime, the RFNoC blocks skips P or R samples until it starts to capture the signal of the next channel. P samples are skipped if the next received signal comes directly after the previous signal. R can be used to adjust the interval T_{rep} at which the entire channel is measured. R can be calculated as:

$$R = \left\lceil \frac{T_{\mathrm{rep}}}{T_{\mathrm{s}}} \right\rceil - \max\{\mathbf{n}_{\mathrm{R}}\}\,\mathrm{sum}\{\mathbf{n}_{\mathrm{T}}\}(P + ML) + P. \tag{2.8}$$

The parameters P and R play a critical role in ensuring full flexibility for the channel sounder, enabling seamless adaptation to diverse scenarios and achieving optimal performance. Typical values for these parameters are provided in Table 3. In Scenario 1, the parameter P is set to be nine times the value of L, effectively corresponding to nine guard frames. This large disparity between P and L is attributed to the RF switch transition time T_{sw}.

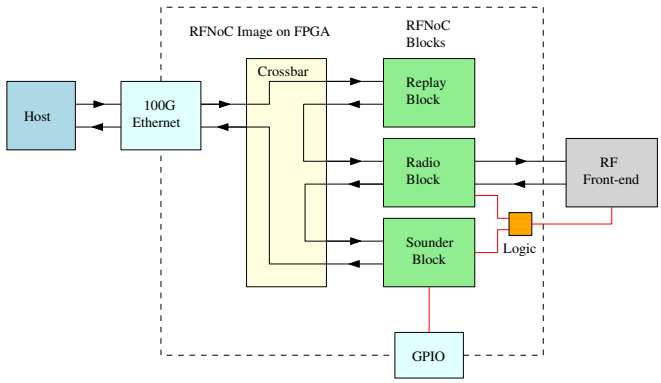

Figure 3: RFNoC image on the FPGA of the USRP X410.

2.3 Implementation

The functionality introduced in the previous subsection has been implemented by custom logic design on the FPGA of the X410 and a C++ application on the host computers. These were developed within the open-source RFNoC framework provided by Ettus Research. This framework allows for time-efficient development through the so-called RFNoC blocks, similar to the GNU Radio structure. The framework takes care of synchronization, clock generation, data streaming, and analog front-end configuration. By default, each block has an input and output port for both data and control packets. The interface is based on the AXI-Stream protocol. Detailed discussion of the RFNoC framework is beyond the scope of this manuscript and can be found in the USRP Hardware Driver and USRP Manual [35]. The complete FPGA implementation, including all the RFNoC blocks, is called an image. Our image is based on the “X4_400" image flavor (UHD v4.2.0.1) and includes two radio blocks, one replay block, and our custom channel sounding block. The radio block is the source and destination block for the RF data and is connected to both the replay block and the channel sounding block. The replay block is an existing block from the RFNoC library and is used to transmit the sounding waveform. With the replay block, we can download our sounding waveform to the X410 DRAM and then start transmitting it at the appropriate time. When the on-board DRAM is used to transmit the sounding signal, there is no transfer of sample data between the host computer and the USRP. Hence, the 1 GbE Ethernet interface could be used to connect the USRP and the host computer if the USRP would only be used as a transmitter or if the receiver data rate is low.

The channel sounding block is responsible for discarding samples, block-

averaging the received waveforms, and controlling the RF switches. The respective samples are discarded by a logic circuit based on a set of counters that can override the valid signal of the AXI-Stream protocol. The non-discarded samples are then transferred to the block averager. Since the data type is complex short, the averaging can be performed efficiently by bit-wise right shifting each real and imaginary sample K times, and then adding the i^{th} sample of each sounding signal. The simplified circuit diagram of the averager is shown in Fig. 4. The averager consists of an arithmetic shifter, block RAM (BRAM), and an adder. Multiplexers are controlled by a counter for $m = \{1, 2, \ldots, M\}$. 1) If $m = 1$: The samples are added with zero and saved in the BRAM. 2) $1 < m < M$: The i-th sample comes in and the i-th sample is fetched out of the memory, and their sum is stored in the memory. 3) $m = M$: The i-th sample comes in, and the i-th sample is fetched from the memory. The sum of those samples is presented at the output of the block averager. In the special case of $m = M = 1$, the i-th sample is presented directly on the output of the averager.

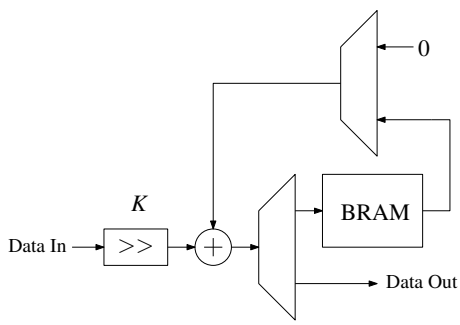

Figure 4: Simplified circuit diagram of the averager within the SounderRx block.

Due to the high sample rate, four samples are being processed per clock cycle, resulting in a memory width of 128 bits. While the sample counter for the averager is enabled by the valid signal of the incoming samples, the counters and logic that control the RF switches (both for the external and internal Tx/Rx switches) are enabled by the `rx_running` or `tx_running` logic signal to ensure the correct timing. These signals are the main on/off signals for the transmitter and receiver chain. The clock driving this RFNoC block is `clk_radio`, of which the frequency is equal to 125 MHz.

To store sample data and configure the USRP, a C++ application has been developed that utilizes the UHD library (Release v4.2.0.1), containing all the essential software to control the USRPs. An additional C++ library was also developed to set the parameters (L, P, K, M, R, $\mathbf{n}_{\text{T}}$, $\mathbf{n}_{\text{R}}$) belonging to the

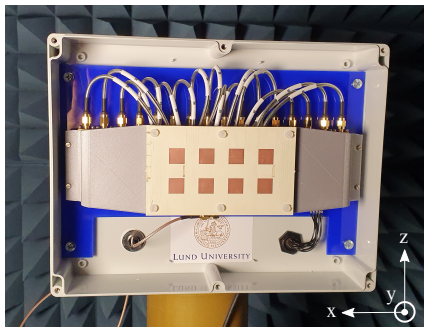

Figure 5: Photograph of one antenna panel in the anechoic chamber.

RFNoC block.

2.4 Synchronization

The USRPs are synchronized via a 1 pulse per second (1PPS) signal for time synchronization and a 10 MHz reference signal for frequency synchronization. Through the main application on the host computer, the synchronization source can be set to either a GPS disciplined oscillator or an external clock (e.g., a Rubidium clock). The channel sounder is designed to start on the positive flank of a 1PPS. To eliminate the requirement that two or more USRPs start at the same 1PPS flank, the repetition time T_{rep} must be chosen so that the TDM scheme has a periodicity of 1, s, so $1/T_{\text{rep}}$ should be a natural number. In this way, multiple USRPs can start at different 1PPS flanks; hence, no communication is needed between them. However, USRPs can also start on the same 1PPS flank via the GPS time when the system is synchronized with GPS.

2.5 Antenna Design

Our implementation comprises eight mini-circuit USB-1SP16T-83H RF switches. For each RF switch, we designed a rectangular 2×4 antenna array with each element having two ports for horizontal and vertical polarization. The geometric centers of the antennas are separated by $26.7\,\text{mm} \approx 0.5\lambda$. Other dimensions can be found in Fig. 6. Each element of the array is a proximity-coupled stacked patch antenna and is designed to operate in the 5.0-6.0 GHz frequency range (S11 $< -10\,\text{dB}$). The antenna is made with Rogers Corp. RO4350B laminate. The antennas are mounted on top of the RF switch inside a plastic box, forming one antenna panel. A photograph of one antenna panel is shown in Fig. 5. All panels

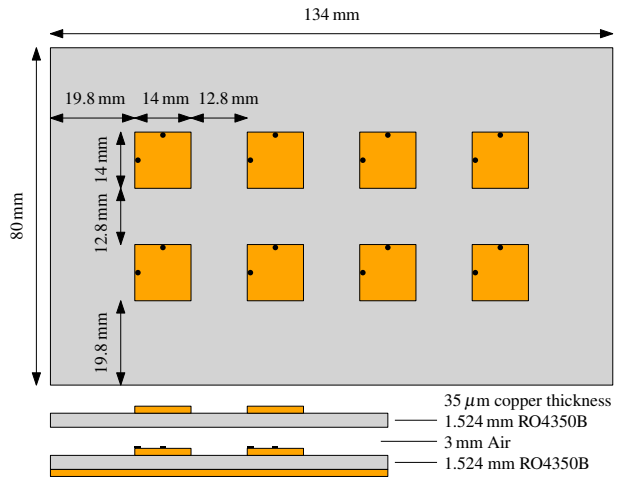

Figure 6: Dimensions of the 16-element antenna array.

have been characterized in an anechoic chamber, which is also needed to perform high-resolution angular estimation of multipath components. Fig. 7 presents the complete radiation pattern for antenna element 7 of a panel at 5.675 GHz for both polarizations, showing a typical pattern of a patch antenna. It should be noted that the gain given in the figures includes switch losses and internal cable losses.

2.6 Final Specifications, Performance and Link Budget

We summarize the channel sounder parameters, possible configurations, and the corresponding performance in Table 2. The upper section of Table 2 collects all the main configuration parameters of the channel sounder with some example values for several measurement scenarios. The lower section of Table 2 includes the equations for important performance metrics and their value for the different scenarios. While Scenarios 1 and 2 are further discussed in Section 4, more information about Scenario 3 can be found in [36]. As demonstrated by the table with the parameters, the channel sounder offers great flexibility in its configuration, allowing the parameters to be adjusted for different application requirements. Beyond parameter configuration, the arrangement of the panels can also be tailored; for example, distributed panels can be used to measure multi-static sensing channels, while co-located panels can be used to measure monostatic sensing channels. Note that monostatic channels cannot be measurement with one panel due to the

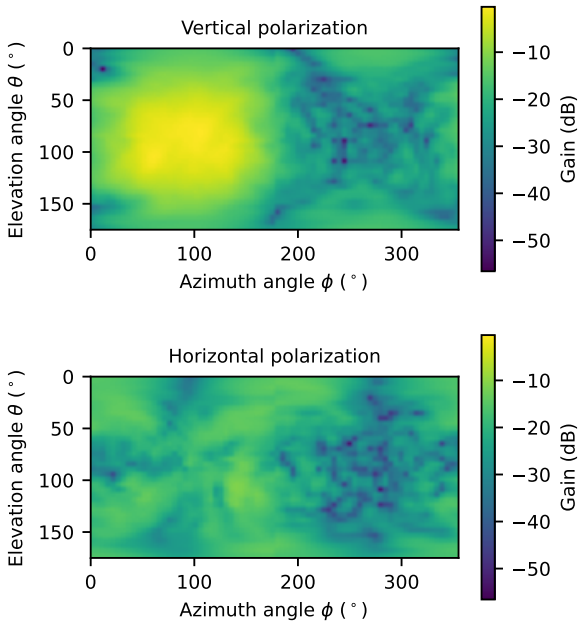

Figure 7: Full measured radiation pattern of vertically-polarized antenna element 7 on panel 0 at 5.675 GHz. The plot shows a typical pattern for a patch antenna. The peak gain value, *including* cable and RF switch losses is -0.4 dBi.

RF switch, as explained in Section 2.

Although most of the calculations in 3 are straightforward, special attention should be paid to the calculation of the maximum Doppler frequency. From the sampling theorem it is known that the sampling frequency should be at least twice the maximum of the absolute value of the Doppler frequency. In our channel sounder three frequencies could be considered as the sampling frequency: *i)* the snapshot rate or the repetition frequency, which has historically been used for the calculation of the maximum Doppler frequency for channel sounders [32], *ii)* the frequency at which each antenna combination is measured [34], applied in systems with a large number of switched antennas, *iii)* the baseband sampling frequency f_s, the fundamental limit. For cases *ii)* and *iii)* the channel is not continuously measured but rather in bursts. If the Doppler frequency is much lower than the sampling frequencies, it might not be possible to estimate the Doppler frequency because the phase difference between the samples is much smaller than the noise component of the signal. Hence, the maximum Doppler frequency should be carefully calculated on the basis of the configuration of the channel sounder and the application scenario. In addition, the average functionality of our channel sounder poses an extra limitation on the Doppler frequency. If we repeat the same waveform $\mathbf{s} \in \mathbb{C}^{L\times 1}$ M times and virtually introduce a Doppler frequency offset ν, the averaged waveform $\mathbf{y} \in \mathbb{C}^{L\times 1}$ becomes:

$$\begin{aligned}\mathbf{y}(i) &= \frac{1}{2^K}\sum_{m=1}^{M}\mathbf{s}(i)\exp(\mathrm{j}2\pi\nu(mLT_\mathrm{s}+iT_\mathrm{s})) \\ &= \frac{1}{2^K}\,\mathbf{s}(i)\exp(\mathrm{j}2\pi\nu iT_\mathrm{s})\sum_{m=1}^{M}\exp(\mathrm{j}2\pi\nu mLT_\mathrm{s}).\end{aligned} \tag{2.9}$$

The summation in (2.9) is a sum of phasors. If the phases of these phasors do not align well, e.g. due to a high Doppler frequency, this sum can drastically attenuate the signal. We consider

$$\nu_\mathrm{max} \leq \frac{0.1 f_\mathrm{s}}{ML} \tag{2.10}$$

to be an acceptable limit. When configuring the channel sounder, it is essential to account for the maximum absolute Doppler frequency that may occur during the measurement. This frequency depends not only on the maximum speed of the transmitter or receiver but also on the velocity of scatterers present in the environment.

A link budget analysis is presented in Fig. 8 of a single antenna as transmitter and a panel as receiver. Note that the noise figure depends on the receiver gain

Table 2: Final specifications of the channel sounder

Specification	**Value**
Type	parallel/switched
Center frequency	5.2−5.8 GHz
Bandwidth	400 MHz
Number of antenna panels	8
Panel array configuration	2×4 dual polarized
Panel azimuth/elevation 10 dB beamwidths	120/120 degrees
Number of standalone antennas	4
Maximum number of antenna combinations	7656
Maximum RF switch frequency	50 kHz
Typical snapshot rate	10−200 Hz
Typical output power	18 dBm
ADC/DAC depth	12/14 bits

Table 3: Typical configuration of the channel sounder and corresponding performance metrics

Description	**Parameter**	**Scenario 1**	**Scenario 2**	**Scenario 3**
Center frequency	f_c	5.675 GHz	5.675 GHz	5.6 GHz
Sample frequency	f_s	500 Msps	500 Msps	500 Msps
Sounding waveform length	L	1024	1024	8192
Number of tones	F	819	819	4095
Number of waveforms to sum in averager	M	8	8	64
Division of 2^K in averager	K	3	3	2
Skipped samples	P	9216	9216	49152
Skipped samples	R	2221472	14348416	1975712
Number of RF chains	N_{RF}	9	8	2
Total number of transmit antennas	$\mathrm{sum}\{\mathbf{n}_\mathrm{T}\}$	1	128	1
Maximum amount of panel antennas	$\max\{\mathbf{n}_\mathrm{R}\}$	16	16	1
Metric	**Equation**			
Bandwidth	$f_s F/L$	400 MHz	400 MHz	250 MHz
Snapshot rate $f_{\mathrm{rep}} = 1/T_{\mathrm{rep}}$	$f_s/(\mathrm{sum}\{\mathbf{n}_\mathrm{T}\}\max\{\mathbf{n}_\mathrm{R}\}(P+ML)+R)$	200 Hz	10 Hz	200 Hz
Coherence time	$\mathrm{sum}\{\mathbf{n}_\mathrm{T}\}\max\{\mathbf{n}_\mathrm{R}\}(P+ML)/f_s$	557 μs	71 ms	2 ms
Antenna combinations	see (2.2)	128	7168	1
Max. delay spread	L/f_s	2 μs	2 μs	16 μs
Max. absolute Doppler frequency	$\min\left(\frac{f_{\mathrm{rep}}}{2} \text{ or } \frac{f_s/2}{P+ML}, \frac{0.1 f_s}{ML}\right)$	29 kHz	29 kHz	100 Hz
Processing gain (w/o beamforming gain)	$10\log_{10}(ML)$	39 dB	39 dB	57 dB
Sensitivity level (20 dB SNR)[1]	$-147.5 + 10\log_{10}(f_s F M)$	-100 dBm	-100 dBm	-118 dBm
Data rate USRP to host (w/o overhead)	$\frac{4 f_s L\,\mathrm{sum}\{\mathbf{n}_\mathrm{T}\}\max\{\mathbf{n}_\mathrm{R}\} N_{\mathrm{RF,USRP}}}{\mathrm{sum}\{\mathbf{n}_\mathrm{T}\}\max\{\mathbf{n}_\mathrm{R}\}(P+ML)+R}$	236 MB/s	671 MB/s	3.2 MB/s

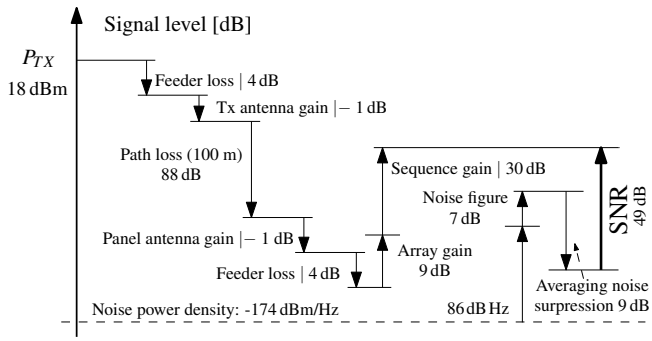

Figure 8: Link-budget analysis of a standalone antenna as transmitter to one antenna panel as receiver. Note that the antenna gains are actually losses and therefore indicated with a downward arrow.

setting on the USRP and is temperature-variant. The noise figure given in the figure is a typical value under maximum gain configuration. In addition, note that antenna gains and array gain depend on AoA and AoD. The antenna gain value given in Fig. 8 is a rounded value of the average broadside antenna gain of all the elements in one panel, including the RF switch losses. For the array gain, a value of 9 dB, corresponding to 8 antenna elements, is considered because the transmitting antenna is vertically polarized. The averaging noise suppression originates from the averaging of the sounding waveforms in the FPGA. The final SNR is 49 dB and is given for a path loss equal to the free space loss at 100 m.

3 Post-processing and calibration

The output data of the channel data can be represented as a six-dimensional tensor $\mathbf{D}(s, p_\mathrm{T}, p_\mathrm{R}, m_\mathrm{T}, m_\mathrm{R}, i)$, where s is the snapshot index, p_T the transmit chain index, p_R the receive chain index, m_T the transmit antenna index, m_R the receive antenna index, and i the sample index. Further data processing is performed by performing a Discrete Fourier Transform on i to obtain $\mathbf{Y}(s, p_\mathrm{T}, p_\mathrm{R}, m_\mathrm{T}, m_\mathrm{R}, k)$ where k is the frequency index. In the following, the frequency indices are selected where a signal was transmitted, i.e. $\mathbf{x}(k) \neq 0$. The complete channel response $\mathbf{H}$ is then calculated by diving $\mathbf{Y}$ by $\mathbf{x}$ in the frequency domain:

$$\mathbf{H}(s, p_\mathrm{T}, p_\mathrm{R}, m_\mathrm{T}, m_\mathrm{R}, k) = \frac{\mathbf{Y}(s, p_\mathrm{T}, p_\mathrm{R}, m_\mathrm{T}, m_\mathrm{R}, k)}{\mathbf{x}(k)}. \tag{3.1}$$

Note that $\mathbf{H}$ includes the response of the RF chains and the antennas, which is not part of the propagation channel. Although this result could already be

used for some simulations, our ultimate goal is to obtain the true propagation characteristics. This can be done by modeling the propagation channel as a superposition of specular multipath components (MPCs), which each have the following parameters: delay (τ), Doppler frequency (ν), azimuth and elevation AoD (ϕ_{T}, θ_{T}), azimuth and elevation AoA (ϕ_{R}, θ_{R}), and complex polarimetric path gains ($\boldsymbol{\gamma}$). In addition, it is assumed that these geometrical propagation parameters of MPCs are unchanged during the observation time of S snapshots. Analytically,

$$\begin{aligned}
&\mathbf{H}(s, p_{\mathrm{T}}, p_{\mathrm{R}}, m_{\mathrm{T}}, m_{\mathrm{R}}, k) \\
&= \sum_{l=1}^{L} \mathbf{a}^{\mathrm{T}}_{m_{\mathrm{R}}, p_{\mathrm{R}}}(\phi_{\mathrm{R},l}, \theta_{\mathrm{R},l}, f_k) \begin{pmatrix} \gamma_{\mathrm{HH},l} & \gamma_{\mathrm{HV},l} \\ \gamma_{\mathrm{VH},l} & \gamma_{\mathrm{VV},l} \end{pmatrix} \\
&\quad \mathbf{a}_{m_{\mathrm{T}}, p_{\mathrm{T}},}(\phi_{\mathrm{T},l}, \theta_{\mathrm{T},l}, f_k) \mathbf{b}_{p_{\mathrm{T}}, m_{\mathrm{R}}}(k) \exp(-\mathrm{j}2\pi f_k \tau_l) \\
&\quad \exp(\mathrm{j}2\pi \nu_l t_{s, p_{\mathrm{T}}, p_{\mathrm{R}}, m_{\mathrm{T}}, m_{\mathrm{R}}}) + \mathbf{N}(s, p_{\mathrm{T}}, p_{\mathrm{R}}, m_{\mathrm{T}}, m_{\mathrm{R}}, f_k),
\end{aligned} \tag{3.2}$$

where f_k is the absolute frequency value that corresponds with frequency index k, l is the index of the MPC, $t_{s, p_{\mathrm{T}}, p_{\mathrm{R}}, m_{\mathrm{T}}, m_{\mathrm{R}}}$ gives the time in seconds when the channel between the respective antenna elements was measured, $\mathbf{N}$ gives the measurement noise. The parameters $\gamma_{\mathrm{HH},l}, \gamma_{\mathrm{HV},l}, \gamma_{\mathrm{VH},l}, \gamma_{\mathrm{VV},l}$ denote the horizontal-to-horizontal, horizontal-to-vertical, vertical-to-horizontal, and vertical-to-vertical polarization gains of the l-th MPC. Moreover, $\mathbf{a}_{m_{\mathrm{T}}, p_{\mathrm{T}}} \in \mathbb{C}^{2\times 1}$ and $\mathbf{a}_{m_{\mathrm{R}}, p_{\mathrm{R}}} \in \mathbb{C}^{2\times 1}$ denote the polarimetric antenna responses. These antenna responses are obtained through the effective aperture distribution function (EADF) [37,38] based on the antenna panel calibration data. Furthermore, $\mathbf{b}_{p_{\mathrm{T}}, p_{\mathrm{R}}}$ contains the frequency response of the sounder without antennas, which can be obtained from a back-to-back measurement with an attenuator. Hence,

$$\mathbf{b}_{p_{\mathrm{T}}, p_{\mathrm{R}}}(k) = \frac{\mathbf{Y}(0, p_{\mathrm{T}}, p_{\mathrm{R}}, 0, 0, k)}{\mathbf{x}(k)\mathbf{s}_{21,\mathrm{att}}(k)}, \tag{3.3}$$

where $\mathbf{s}_{21,\mathrm{att}} \in \mathbb{C}^{F\times 1}$ is the frequency response of the attenuator measured with a VNA. Note that due to the design of the channel sounder, it is not possible to measure the response between the transmit and receive chains on the same channel, i.e. $p_{\mathrm{T}} \neq p_{\mathrm{R}}$. Measurement of all RF channel combinations can be cumbersome and time consuming. $N_{\mathrm{RF}}(N_{\mathrm{RF}}-1)/2$ connections have to be made. To decrease this amount, it is possible to obtain all combinations $\mathbf{b}_{p_{\mathrm{T}}, p_{\mathrm{R}}}$ by measuring only a set of combinations, which needs $2(N_{\mathrm{RF}}-2)+1$ back-to-back

connections. Analytically,

$$\mathbf{b}_{p_\mathrm{T},p_\mathrm{R}}(k) = \frac{\mathbf{b}_{0,p_\mathrm{R}}(k)\mathbf{b}_{p_\mathrm{T},1}(k)}{\mathbf{b}_{0,1}(k)}. \tag{3.4}$$

Several approaches exist to estimate the MPC parameters $(\tau, \nu, \phi_\mathrm{T}, \theta_\mathrm{T}, \phi_\mathrm{R}, \theta_\mathrm{R}, \boldsymbol{\gamma})$ such as expectation-maximization (EM) [39], space-alternating generalized expectation maximization (SAGE) [40, 41], and RIMAX [37]. To process our verification measurements in Section 4, we have implemented and applied the SAGE algorithm.

4 Verification and Measurements

4.1 Scenario 1: Uplink Measurement

In order to verify the functionality of the channel sounder, we have performed a measurement of the propagation channel at 5.675 GHz between a single antenna robot and eight distributed panels in an indoor laboratory environment with a bandwidth of 400 MHz. The laboratory room, depicted in Fig. 9, measures approximately 5 meters by 12 meters, of which an area of 5 meters by 6 meters was used for measurements. Eight panels were distributed in the room in groups of two, as illustrated in Fig. 10. Each group of two panels was vertically stacked at heights of 0.92 m and 1.84 m. Then each group of four panels was connected to a USRP X410 through 10 m long LMR400 RF cables and custom-made cables for switch control. The two USRPs were connected to an industrial computer through a link 100 GbE and are synchronized through one Rubidium clock.

The robot is equipped with a USRP X410, a wideband dipole antenna, two regular laptops, a Rubidium reference clock, an uninterruptible power supply (UPS), a light detection and ranging (lidar) sensor and an inertial measurement unit (IMU). A laptop was responsible for controlling the USRP and the movement of the robot. The other laptop was used to collect data from the lidar and IMU, which provide ground-truth information on the location of the robot and the panels in the room using a simultaneous localization and mapping (SLAM) algorithm. Reflective tape was applied to the panels to enhance their visibility in the lidar scan. The robot is an in-house design based on a hoverboard and is controlled via a game controller over Bluetooth. A detailed list of primary equipment can be found in Table 4.

During the measurements, the robot followed a round trajectory, maintaining a line-of-sight (LoS) connection to all panels, as illustrated in Fig. 10. The

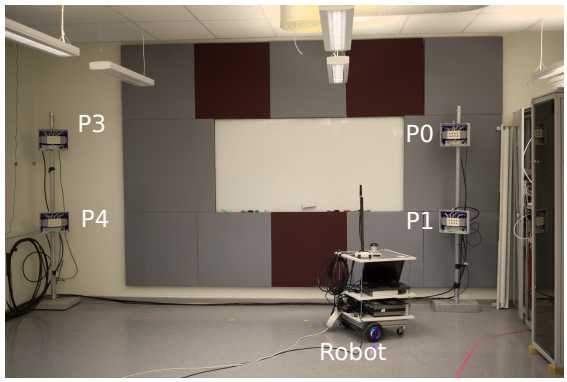

Figure 9: Photograph of the measurement setup and environment. Four of the eight panels (P3, P4, P0, P1) are visible: two on the left and two on the right. The robot is located in front of the panels.

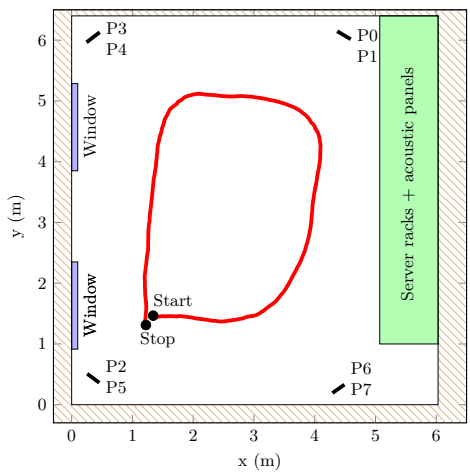

Figure 10: Floor plan of the measurement environment and the trajectory for the uplink measurement given in red.

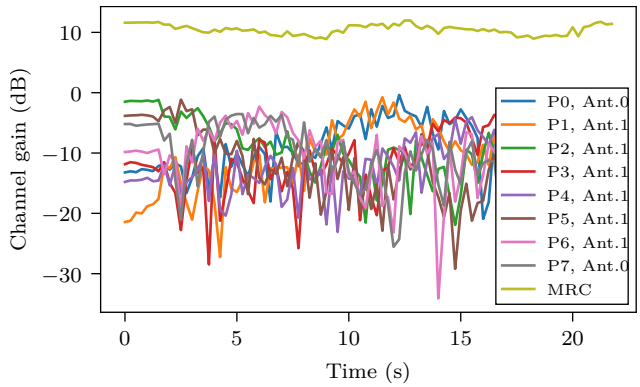

Figure 11: Narrowband channel gain at 5.675 GHz for a single vertically-polarized antenna per panel and the result after performing maximum ratio combining (MRC) of all 128 channels.

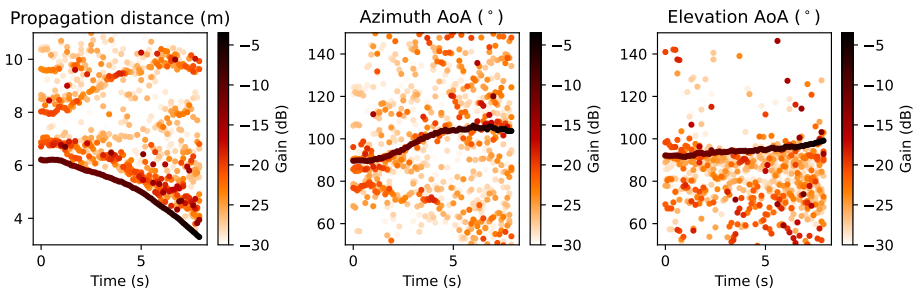

Figure 12: High-resolution parameter estimates of the MPCs seen from P0 using the SAGE algorithm for the first eight seconds of the uplink channel measurement. From left to right: propagation distance, azimuth AoA, elevation AoA. The LoS component can be recognized by the dark red dots due to its higher gain.

channel sounder configuration during this measurement can be found in Table 3.

Fig. 11 presents the narrowband channel gains during the measurement for several vertically polarized antenna elements at different panels, and the channel gain after applying maximum ratio combining (MRC) for all 128 antennas. It can be observed that with MRC the overall channel gain increased. The deep small-scale fading experienced by every single antenna has also been effectively mitigated. This demonstrates the potential for an increase in reliability with distributed massive MIMO systems. Furthermore, the SAGE algorithm is applied to extract the parameters of the MPCs observed by panel 0 are depicted in Fig. 12 for the initial eight seconds of measurement. The LoS component is readily apparent. In the propagation distance plot, we discern two additional tracks of MPCs. The path closest to the LoS emanates from reflections from the ceiling and the ground. The other track, which exhibits increasing propagation distance, is most likely a reflection off one of the side walls of the room. In the azimuth plot, we also observe these two MPC tracks in addition to the LoS. One of these tracks aligns closest to the LoS azimuth angle, while the other track ranges from around 80 degrees to about 70 degrees. Examining the elevation plot, we observe that MPCs originate primarily from the ceiling, which is attributed to the lighting infrastructure that causes significant scattering.

4.2 Scenario 2: Sensing Measurement

To demonstrate the sensing capability of our channel sounder, we have performed an additional measurement in the same environment as in Section 4.1. In contrast to the previous measurement, all eight panels are now configured both to transmit and receive. This configuration allows us to estimate the AoD from each panel, which can be useful for sensing purposes. The channel sounder configuration can be found in Tab. 3 under Scenario 2. The purpose of this measurement was to test the capability of sensing a person with our channel sounder, based

Table 4: Primary equipment

Device	Amount	Model
Software-defined radio	3	NI USRP X410
Industrial computer	1	Advanctech MIC-770 V2
Dipole antenna	1	Taoglas TU.60.3H31
Rubidium clock	2	SRS FS725 & SRS FS740
Lidar	1	Ouster OSDome (128 lines)
IMU	1	Microstrain 3DM-GX5-25 (AHRS)
RF switches (panel)	8	Mini-Circuits USB-1SP16T-83H

on the estimated parameters MPCs parameters. During the measurement, a member of the research group walked on the red line shown in Fig. 13 in a time of approximately 10 seconds. Hence, the person had an average speed of 0.3 m/s. The person stood still at the beginning and in the middle of the walk. The SAGE estimation results of the propagation delay (τ), azimuth AoD (ϕ_{T}) and AoA (ϕ_{R}) are presented in Fig. 14. The figures show that most of the estimates are not time dependent because the panels and the environment are static, except for the walking person. However, we are interested in the MPCs that change over time because these could be related to the moving person. At 5 seconds in the AoD plot, a change in AoD can be observed. To get a better observation of the dynamic MPCs, we need to track the MPCs and associate one or more MPC tracks with the moving person. However, tracking multipath components is a complex and active area of research, and addressing it thoroughly goes beyond the focus of this work. The interested readers are referred to [42, 43] and references therein. Instead, we have manually selected a region where we, according to the somewhat known position of the person, expected scattering from the walking person. This selected region is $\{\tau = [29\,\mathrm{ns}, 32\,\mathrm{ns}], \phi_{\mathrm{R}} = [65^\circ, 110^\circ], \theta_{\mathrm{T}} = [70^\circ, 180^\circ]\}$. The MPCs in this subspace are marked with the blue line in Fig. 14. To verify that the MPCs in this subspace are linked to the moving person, we calculated the intersection between the AoD and the AoA, indicated with the blue crosses in Fig. 13. Because intersection points are in close proximity of the red line, we can confident that the MPCs are connected to the movement of the person.

5 Conclusions

In this paper we have presented the design, implementation and verification of a channel sounder for distributed massive MIMO based on open-source software and off-the-shelf electronic components. Our design uses multiple NI-USRP X410 and radio frequency switches as core components. Using a flexible design, customized FPGA code, and the integration of multiple parallel transceiver chains and RF switches, we were able to scale up the number of antennas in a cost-efficient way and without significant compromise in dynamic capability. The combination of the high number of antennas, wide bandwidth and multi-node capability makes this design a valuable asset for conducting cutting-edge research within areas such as distributed massive MIMO and integrated sensing and communication. This potential was demonstrated through two measurement campaigns in our laboratory, one distributed massive MIMO uplink measurement

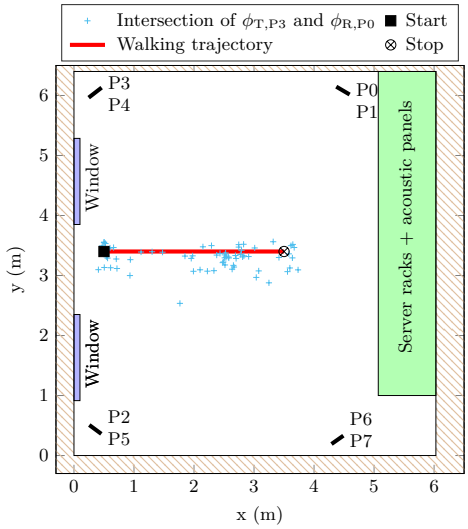

Figure 13: Floor plan of the measurement environment. The walking trajectory of a person is given by the red line. The blue crosses are the intersections of the AoD from P3 and AoA of P1, after selecting a parameter subspace.

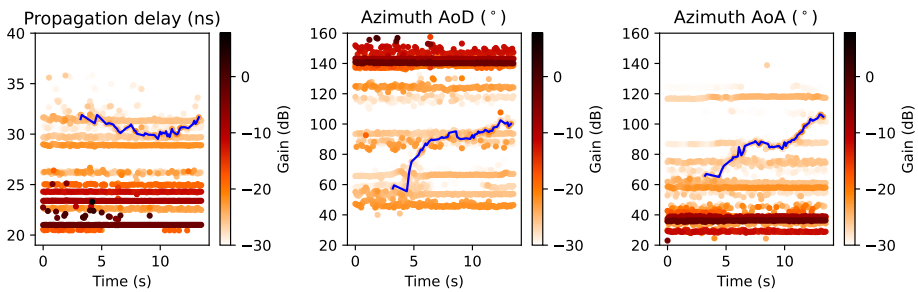

Figure 14: High-resolution parameter estimates of the MPCs between P1 (Rx) and P3 (Tx) using the SAGE algorithm during measurement scenario 2. From left to right: propagation delay, azimuth AoD, azimuth AoA. The blue line highlights the selected multipath components within the region $\{\tau = [29\,\text{ns}, 32\,\text{ns}], \phi_R = [65°, 110°], \theta_T = [70°, 180°]\}$. We believe that these MPCs are caused by scattering from the walking person.

and one passive sensing measurement.

Acknowledgement

The authors thank Yingjie Xu for his assistance during the measurements and Guoda Tian for proofreading the manuscript.

References

[1] H. Q. Ngo, A. Ashikhmin, H. Yang, E. G. Larsson, and T. L. Marzetta, "Cell-Free Massive MIMO Versus Small Cells," *IEEE Transactions on Wireless Communications*, vol. 16, no. 3, pp. 1834–1850, Mar. 2017.

[2] Özlem Tugfe Demir, E. Björnson, and L. Sanguinetti, "Foundations of user-centric cell-free massive MIMO," *Foundations and Trends in Signal Processing*, vol. 14, no. 3-4, pp. 162–472, 2021.

[3] H. Q. Ngo, L.-N. Tran, T. Q. Duong, M. Matthaiou, and E. G. Larsson, "On the Total Energy Efficiency of Cell-Free Massive MIMO," *IEEE Transactions on Green Communications and Networking*, vol. 2, no. 1, pp. 25–39, Mar. 2018.

[4] E. Björnson and L. Sanguinetti, "Making Cell-Free Massive MIMO Competitive With MMSE Processing and Centralized Implementation," *IEEE Transactions on Wireless Communications*, vol. 19, no. 1, pp. 77–90, Jan. 2020.

[5] E. Björnson, L. Sanguinetti, H. Wymeersch, J. Hoydis, and T. L. Marzetta, "Massive MIMO is a reality—What is next?: Five promising research directions for antenna arrays," *Digital Signal Processing*, vol. 94, pp. 3–20, Nov. 2019.

[6] S. Hu, F. Rusek, and O. Edfors, "Beyond Massive MIMO: The Potential of Data Transmission With Large Intelligent Surfaces," *IEEE Transactions on Signal Processing*, vol. 66, no. 10, pp. 2746–2758, May 2018.

[7] G. Interdonato, E. Björnson, H. Quoc Ngo, P. Frenger, and E. G. Larsson, "Ubiquitous cell-free Massive MIMO communications," *EURASIP Journal on Wireless Communications and Networking*, vol. 2019, no. 1, p. 197, Aug. 2019.

[8] L. Van der Perre, E. G. Larsson, F. Tufvesson, L. D. Strycker, E. Björnson, and O. Edfors, "RadioWeaves for efficient connectivity: analysis and impact of constraints in actual deployments," in *2019 53rd Asilomar Conference on Signals, Systems, and Computers*, Nov. 2019, pp. 15–22, iSSN: 2576-2303.

[9] Recommendation M.2160-0, "Framework and overall objectives of the future development of imt for 2030 and beyond," Nov. 2023.

[10] E. G. Larsson and J. Vieira, "Phase Calibration of Distributed Antenna Arrays," *IEEE Communications Letters*, vol. 27, no. 6, pp. 1619–1623, Jun. 2023.

[11] C. Nelson, X. Li, T. Wilding, B. Deutschmann, K. Witrisal, and F. Tufvesson, "Large Intelligent Surface Measurements for Joint Communication and Sensing," in *2023 Joint European Conference on Networks and Communications & 6G Summit (EuCNC/6G Summit)*, Jun. 2023, pp. 228–233.

[12] S. Zelenbaba, D. Löschenbrand, M. Hofer, A. Dakić, B. Rainer, G. Humer, and T. Zemen, "A Scalable Mobile Multi-Node Channel Sounder," in *2020 IEEE Wireless Communications and Networking Conference (WCNC)*, May 2020.

[13] D. A. Wassie, I. Rodriguez, G. Berardinelli, F. M. L. Tavares, T. B. Sørensen, T. L. Hansen, and P. Mogensen, "An Agile Multi-Node Multi-Antenna Wireless Channel Sounding System," *IEEE Access*, vol. 7, pp. 17 503–17 516, 2019.

[14] F. Euchner, M. Gauger, S. Doerner, and S. ten Brink, "A Distributed Massive MIMO Channel Sounder for "Big CSI Data"-driven Machine Learning," in *WSA 2021; 25th International ITG Workshop on Smart Antennas*, Nov. 2021.

[15] E. P. Simon, P. Laly, J. Farah, E. Tanghe, W. Joseph, and D. P. Gaillot, "Measurement of the V2I Channel in Cell-free Vehicular Networks with the Distributed MaMIMOSA Channel Sounder," in *2023 17th European Conference on Antennas and Propagation (EuCAP)*, Mar. 2023, pp. 1–5.

[16] I. C. Sezgin, M. Dahlgren, T. Eriksson, M. Coldrey, C. Larsson, J. Gustavsson, and C. Fager, "A Low-Complexity Distributed-MIMO Testbed Based on High-Speed Sigma–Delta-Over-Fiber," *IEEE Transactions on Microwave Theory and Techniques*, vol. 67, no. 7, pp. 2861–2872, Jul. 2019.

[17] D. Löschenbrand, M. Hofer, L. Bernadó, G. Humer, B. Schrenk, S. Zelenbaba, and T. Zemen, "Distributed Massive MIMO Channel Measurements in Urban Vehicular Scenario," in *2019 13th European Conference on Antennas and Propagation (EuCAP)*, Mar. 2019.

[18] A. P. Guevara, S. De Bast, and S. Pollin, "Weave and Conquer: A Measurement-based Analysis of Dense Antenna Deployments," in *ICC 2021 - IEEE International Conference on Communications*, Jun. 2021, pp. 1–6.

[19] J. Flordelis, G. Dahman, and F. Tufvesson, "Measurements of large-scale parameters of a distributed MIMO antenna system in a microcell environment At 2.6 GHz," in *2013 7th European Conference on Antennas and Propagation (EuCAP)*, Apr. 2013, pp. 3026–3030.

[20] T. Choi, P. Luo, A. Ramesh, and A. F. Molisch, "Co-Located vs Distributed vs Semi-Distributed MIMO: Measurement-Based Evaluation," in *2020 54th Asilomar Conference on Signals, Systems, and Computers*, Nov. 2020, pp. 836–841.

[21] M. Alatossava, A. Taparugssanagorn, V.-M. Holappa, and J. Ylitalo, "Measurement Based Capacity of Distributed MIMO Antenna System in Urban Microcellular Environment at 5.25 GHz," in *VTC Spring 2008 - IEEE Vehicular Technology Conference*, May 2008, pp. 430–434.

[22] D. Stanko, M. Döbereiner, G. Sommerkorn, D. Czaniera, C. Andrich, C. Schneider, S. Semper, A. Ihlow, and M. Landmann, "Time Variant Directional Multi-Link Channel Sounding and Estimation for V2X," in *2023 IEEE 97th Vehicular Technology Conference (VTC2023-Spring)*, Jun. 2023, pp. 1–5, iSSN: 2577-2465.

[23] C. Nelson, X. Li, A. Fedorov, B. Deutschmann, and F. Tufvesson, "Distributed MIMO Measurements for Integrated Communication and Sensing in an Industrial Environment," *Sensors*, vol. 24, no. 5, p. 1385, Jan. 2024.

[24] S. Malkowsky, J. Vieira, L. Liu, P. Harris, K. Nieman, N. Kundargi, I. C. Wong, F. Tufvesson, V. Öwall, and O. Edfors, "The World's First Real-Time Testbed for Massive MIMO: Design, Implementation, and Validation," *IEEE Access*, vol. 5, pp. 9073–9088, 2017.

[25] P. Laly, D. Gaillot, G. Delbarre, M. V. d. Bossche, G. Vermeeren, F. Challita, E. Tanghe, E. Simon, W. Joseph, L. Martens, and M. Liénard, "Massive Radio Channel Sounder Architecture for 5G Mobility Scenarios: MaMIMOSA,"

in *2020 14th European Conference on Antennas and Propagation (EuCAP)*, Mar. 2020.

[26] D. Caudill, J. Chuang, S. Y. Jun, C. Gentile, and N. Golmie, "Real-Time mmWave Channel Sounding Through Switched Beamforming With 3-D Dual-Polarized Phased-Array Antennas," *IEEE Transactions on Microwave Theory and Techniques*, vol. 69, no. 11, pp. 5021–5032, Nov. 2021. [Online]. Available: https://ieeexplore.ieee.org/document/9527393

[27] M. Kim, H. Tsukada, K. Kumakura, R. Takahashi, N. Suzuki, H. Sawada, and T. Matsumura, "A 24/60-GHz Dual-Band Double-Directional Channel Sounder Using COTS Phased Arrays," in *2022 IEEE International Conference on Communications Workshops (ICC Workshops)*, May 2022, pp. 1113–1117, iSSN: 2694-2941.

[28] D. Stanko, G. Sommerkorn, A. Ihlow, and G. D. Galdo, "Enable SDRs for Real-Time MIMO Channel Sounding featuring Parallel Coherent Rx Channels," in *2022 IEEE 95th Vehicular Technology Conference: (VTC2022-Spring)*, Jun. 2022.

[29] P. Laly, D. P. Gaillot, M. Lienard, P. Degauque, E. Tanghe, W. Joseph, and L. Martens, "Flexible real-time MIMO channel sounder for multidimensional polarimetric parameter estimation," in *2015 IEEE Conference on Antenna Measurements & Applications (CAMA)*, Nov. 2015, pp. 1–3.

[30] "Open USRP Channel Sounder." [Online]. Available: https://github.com/michielsandra/openucs

[31] M. Sandra, C. Nelson, and A. J. Johansson, "Ultrawideband USRP-Based Channel Sounding Utilizing the RFNoC Framework," in *2022 IEEE Conference on Antenna Measurements and Applications (CAMA)*, Dec. 2022.

[32] A. F. Molisch, *Wireless Communications*, 2nd ed. Wiley Publishing, 2011.

[33] D. Chu, "Polyphase codes with good periodic correlation properties (Corresp.)," *IEEE Transactions on Information Theory*, vol. 18, no. 4, pp. 531–532, Jul. 1972.

[34] X. Cai, E. L. Bengtsson, O. Edfors, and F. Tufvesson, "A Switched Array Sounder for Dynamic Millimeter-Wave Channel Characterization: Design, Implementation and Measurements," *IEEE Transactions on Antennas and Propagation*, 2023.

[35] Ettus Research, "USRP Hardware Driver and USRP Manual." [Online]. Available: https://files.ettus.com/manual/

[36] M. Sandra, G. Tian, A. Fedorov, X. Cai, and A. J. Johansson, "Measurement-Based Wideband Maritime Channel Characterization," *The 17th European Conference on Antennas and Propagation (EuCAP 2023)*, 2023.

[37] A. Richter, "Estimation of Radio Channel Parameters: Models and Algorithms," Ph.D. dissertation, Ilmenau University of Technology, Germany, 2005.

[38] X. Cai, M. Zhu, A. Fedorov, and F. Tufvesson, "Enhanced Effective Aperture Distribution Function for Characterizing Large-Scale Antenna Arrays," *IEEE Transactions on Antennas and Propagation*, vol. 71, no. 8, pp. 6869–6877, Aug. 2023.

[39] M. Feder and E. Weinstein, "Parameter estimation of superimposed signals using the EM algorithm," *IEEE Transactions on Acoustics, Speech, and Signal Processing*, vol. 36, no. 4, pp. 477–489, Apr. 1988.

[40] J. Fessler and A. Hero, "Space-alternating generalized expectation-maximization algorithm," *IEEE Transactions on Signal Processing*, vol. 42, no. 10, pp. 2664–2677, Oct. 1994.

[41] B. Fleury, M. Tschudin, R. Heddergott, D. Dahlhaus, and K. Ingeman Pedersen, "Channel parameter estimation in mobile radio environments using the SAGE algorithm," *IEEE Journal on Selected Areas in Communications*, vol. 17, no. 3, pp. 434–450, Mar. 1999.

[42] T. Jost, W. Wang, U.-C. Fiebig, and F. Perez-Fontan, "Detection and Tracking of Mobile Propagation Channel Paths," *IEEE Transactions on Antennas and Propagation*, vol. 60, no. 10, pp. 4875–4883, Oct. 2012.

[43] X. Li, E. Leitinger, A. Venus, and F. Tufvesson, "Sequential Detection and Estimation of Multipath Channel Parameters Using Belief Propagation," *IEEE Transactions on Wireless Communications*, vol. 21, no. 10, pp. 8385–8402, Oct. 2022.

Mitigating Sea Surface Fading with D-MIMO: Experimental Validation

Michiel Sandra, Sara Willhammer, Anders J Johansson

Paper IV

Published as: M. Sandra, S. Willhammar, A. J. Johansson, "Mitigating Sea Surface Fading with D-MIMO: Experimental Validation," *2025 19th European Conference on Antennas and Propagation (EuCAP)*, Stockholm, Sweden, 2025.

Abstract

The performance of wireless communications at sea are often limited by fading caused by reflections at the sea surface. The reliability could potentially be improved by employing multiple antennas. We have conducted massive multiple-input multiple-output (MIMO) measurements at sea in order to evaluate the performance. The measurements were conducted at 5.6 GHz with 64 dual-polarized antennas, which were distributed vertically in groups of eight antennas. We evaluated the CDF of the maximum-ratio combined channel gain for different number of antennas, and compared distributed and co-located antenna configurations. We conclude that having distributed antennas is key to reduce the channel fading by a significant amount. Additionally, optimizing antenna spacing can significantly minimize fading without requiring a large number of antennas. In our scenario, the channel fading could be reduced by 15 dB by employing only three distributed antennas, showing the potential of distributed MIMO systems to improve reliability in maritime communications.

1 Introduction

Maritime radio systems have been playing a crucial role in maritime activities during the last hundred years, in particular for navigation and safety purposes. There is a great interest to provide wireless services through land-based base stations for vessels in the coastal area. In today's cellular infrastructure, typically only one sector antenna is used at the base station. Having more, and widely spread, antennas at the base station could greatly improve the reliability, which is often critical for maritime applications.

The reliability improves with an increasing number of antennas, as a consequence of coherent combining of the signal, resulting in an array gain and a channel hardening effect. The latter meaning that the channel becomes more stable in both time and frequency. This effect has been experimentally validated and showed to be more or less prominent depending on the propagation environment [1, 2]. The underlying massive multiple-input multiple-output (MIMO) channel can be modeled as independent and identically distributed (i.i.d) complex Gaussian; this has previously been assumed in literature, and would result in a significant channel hardening effect [3] However, this rarely holds in real propagation channels [4].

The propagation environment at sea is known to be different from typical indoor and outdoor scenarios and it has been well established in literature that the propagation loss at sea in general can be modeled as a two-ray model, resulting in deep fading dips over the distance [5–7]. To combat these fading dips, theoretical

results were presented in [8] where the use of multiple antennas in an uniform linear array was proposed as a solution and bounds were derived.

The theoretical results in [8] need verification, which has until now been lacking. With a unique measurement campaign conducted at sea, we present and analyze the effect of deploying multiple antennas for maritime communication with both co-located and more spread distributions. We evaluate the reliability improvement in terms of increased channel hardening effects and relate this to the antenna spacing at the base station side, providing insights into maritime channels and proposing strategies for system deployment at sea.

The remaining article is structured as follows. In Section 2, we elaborate on fading mitigation at sea, providing the necessary background. Section 3 explains the measurement equipment and campaign before the signal model and data processing is outlined in Section 4. The results are are presented and discussed in Section 5 before concluding in Section 6.

2 Fading Mitigation at Sea

The propagation loss as sea can, as previously mentioned, typically be modeled as a two-ray model for propagation distances short enough such that the diffraction loss due to the earth's curvature and other propagation phenomena can be neglected [5]. This model, normalized to the free space loss, can be expressed as

$$g = 1 + \rho \exp \frac{-\mathrm{j}4\pi h_t h_r}{\lambda d} \tag{2.1}$$

where λ is the wavelength, d is the great-circle distance between the transmitter and the receiver, ρ is the reflection coefficient, and h_t and h_r are the transmitter and receiver height above the sea level, respectively. In a typical scenario, e.g. $d = 10\,\mathrm{km}$ and $h_t = 10\,\mathrm{m}$, the angle of incidence of the sea surface reflection approaches $\pi/2$ and therefore $\angle\rho \approx \pi$. As a result, g can experience deep fades when d approaches $\frac{2h_t h_r}{\lambda k}$ where $k \in \mathbb{N}_0$. The deep fades could be mitigated by employing multiple antennas at the base station, as this reduces the risk of a deep fade occurring simultaneously across two or more antenna elements. The outcome of the theoretical analysis in [8] consist of a set of equations that are giving the boundaries for a range $d \in [d_{\mathrm{st}}, d_{\mathrm{end}}]$ where the signal-to-noise ratio (SNR) gain relative to the free-space propagation scenario is larger than a desired threshold β. With some slight simplifications ($k = 0$ and $|\rho| = 1$), the expressions for d_{st} and d_{end} are noted as

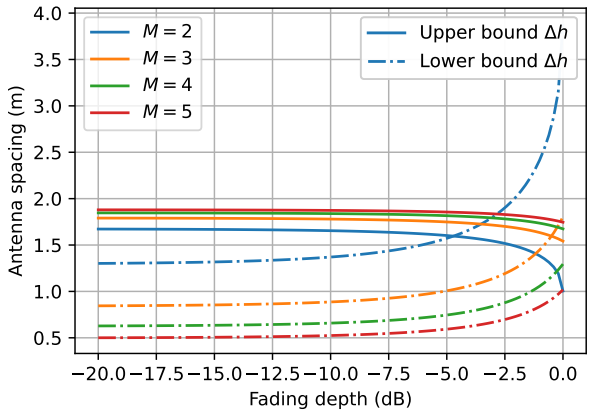

Figure 1: Visualization of (2.4), with the parameters configured as in the measurement campaign.

$$d_{\text{st}} = \frac{2\pi h_t \Delta h}{\lambda(\pi - \arcsin \frac{1}{M(1-\beta/2)})}, \tag{2.2}$$

$$d_{\text{end}} = \frac{2\pi h_t \Delta h}{\lambda \arcsin \frac{1}{M(1-\beta/2)}}, \tag{2.3}$$

where Δh is the spacing between the antennas and M is the total number of antennas. We can also utilize (2.2) and (2.3) to calculate the antenna spacing Δh needed in order to achieve a desired performance within a region of interest, resulting in

$$\frac{d_{\text{end}}\lambda \arcsin \frac{1}{M(1-\beta/2)}}{2\pi h_t} \leq \Delta h \leq \frac{d_{\text{st}}\lambda(\pi - \arcsin \frac{1}{M(1-\beta/2)})}{2\pi h_t}. \tag{2.4}$$

Note that the right-hand side of (2.4) is not always larger than the left-hand side, e.g. when d_{st} is very small. In such cases, it can not be guaranteed that fading can be mitigated and a suitable value for Δh does not exist. Whether fading can be mitigated depends on the intended application scenario and corresponding parameters: h_t, d_{st}, and d_{end}.

In Fig. 1, the upper and lower bounds from (2.4) are plotted using the parameters used in our measurement scenario. For e.g. $M = 2$, it can be observed that the range for Δh decrease as the fading depth requirement increases. The point which minimizes the experienced fading is the point where the upper and lower bound intersect, i.e. $\Delta h = 1.6\,\text{m}$; then the fading is is not worse than -5 dB.

Figure 2: Photographs of the sailboat (Tx) and the vertical array (Rx) ashore.

For larger number of antennas, this intersection moves to the right in the figure, meaning that the fading is even more effectively mitigated.

3 Measurement campaign and setup

The measurement campaign took place in September 2023 in Klagshamn, Sweden (N 55.523° E 12.895°). The measurement setup comprised of a single-antenna transmitter on top of a sailboat at around 10 m height above sea level. On the receiver side, a 64-element dual-polarized antenna array was installed ashore, as depicted in Fig. 2. The array comprises of eight vertically distributed panels with a spacing of 0.5 m, with the top panel being positioned at 8 m above sea level. Each panel consists of a 4×2 dual-polarized antennas, i.e. 16 channels in total. A sounding signal was transmitted every 5 ms and occupied a bandwidth of 250 MHz at 5.6 GHz. We sailed for around two hours in open sea and reached a maximum distance of 5 km between transmitter and receiver.

During the measurement campaign, we utilized the channel sounder presented in [9], which is based on the NI USRP X410. The configuration of the parameters is summarized in Table I. The channel sounder is of a hybrid-switched type, in which radio-frequency (RF) switches are used in combination with several RF chains. In our setup, the eight RF chains were connected to the panels, each consisting of an SP16T RF switch and an low-noise amplifier (LNA). We also utilized a power amplifier at the transmitter to enlarge the dynamic range of the sounding system. In addition, we utilized an RTK GNSS receiver (SwiftNav DURO) as positioning system.

Table 1: Overview of the configuration parameters and performance metrics of the channel sounder

Description	**Parameter**	**Value**
Center frequency	f_c	5.6 GHz
Sample frequency	f_s	500 Msps
Sounding waveform length	L	4096
Number of tones	F	2048
Number of waveforms to sum in averager	M	16
Division of 2^K in averager	K	4
Skipped samples	P	12288
Skipped samples	R	1254816
Number of RF chains	N_{RF}	9
Total number of transmit antennas	$\mathrm{sum}\{\mathbf{n}_{\mathrm{T}}\}$	1
Maximum amount of panel antennas	$\max\{\mathbf{n}_{\mathrm{R}}\}$	16
Transmit power at the antenna	P_{tx}	20 dBm
Metric		**Value**
Bandwidth		250 MHz
Snapshot rate		200 Hz
Coherence time		2.5 ms
Antenna combinations		8
Max. delay spread		8 μs
Max. Doppler frequency		100 Hz
Processing gain (w/o beamforming gain)		48 dB
Sensitivity level (20 dB SNR)		-105 dBm
Data rate USRP to host (w/o overhead)		419 MB/s

4 Signal model and data processing

The time-varying measured channel transfer function in the frequency domain is denoted as $h_m(k,n)$, where $k \in [1, \cdots, 2048]$ indexes the subcarriers/tones, m is the antenna index, and n is the snapshot index. The underlying signal model of $h_m(k,n)$ can then be expressed as

$$h_m(k,n) = \sum_{\ell=1}^{L(n)} \alpha_{\ell m}(n) \exp(-\mathrm{j}2\pi f_k \tau_{\ell m}(n)), \tag{4.1}$$

where $\alpha_{\ell m}(n)$ and $\tau_{\ell m}(n)$ indicate the time-varying complex amplitude and delay of the ℓ-th multipath component (MPC), respectively. The scalar f_k is the absolute frequency of the k-th subcarrier and $L(n)$ is the number of MPCs observed at snapshot n. In order to reduce complexity and keep the focus on the spatial characteristics of the channel, we choose to only study the narrowband channel, i.e. the propagation channel at a single frequency. The narrowband channel is estimated through the following steps. First the parameters $\alpha_{\ell m}(n)$ and $\tau_{\ell m}(n)$ are estimated, and then the narrowband channel is reconstructed as

$$h_m(n) = h_m(0,n) = \sum_{\ell=1}^{L(n)} \hat{\alpha}_{\ell m}(n) \exp(-\mathrm{j}2\pi f_0 \hat{\tau}_{\ell m}(n)), \tag{4.2}$$

where we choose $f_0 = 5.6\,\text{GHz}$. The space-alternating generalized expectation-maximization (SAGE) algorithm is applied in order to estimate $\alpha_{\ell m}(n)$ and $\tau_{\ell m}(n)$. For more details about the SAGE principle, see [10]. Next, the channel is normalized as

$$\tilde{h}_m(n) = \frac{h_m(n) \cdot d_n}{\sqrt{\frac{1}{NM}\sum_{n=1}^{N}\sum_{m=1}^{M}|h_m(n) \cdot d_n|^2}}. \tag{4.3}$$

where M and N are the total number of antennas and snapshots, respectively, and d_n is the great-circle distance between the transmitter and the receiver. The normalized channel gain for the p selected antennas is then computed as

$$G_p(n) = \frac{1}{p}\sum_{m \in S_p}|\tilde{h}_m(n)|^2. \tag{4.4}$$

where S_p is the set containing the p selected antenna indices.

5 Results and Analysis

Starting the results and analysis with a high-level inspection of the data for visualisation purposes; Fig. 3 depicts an overview of the general measurement result. Due to the large size of the data set, only one percent of the measurement points is shown, yet all measurement points are used in the data processing. The strongest antenna in each panel is selected. With strongest, it means that $\|\tilde{\boldsymbol{h}}_m\|^2 = \sum_{n=1}^{N}|\tilde{h}_m(n)|^2$ has the highest value within that panel. As a start, for each subset of antennas, the antennas are selected sequentially, beginning with the top panel and moving towards the bottom panel. In the figure, one can observe the typical two-ray behavior with deep fading dips occuring along the route. As the number of antennas is increased, the fading dips become less deep. When all of the eight distributed antennas are selected, the fading dips are barely noticeable and hence the channel is significantly more stable, resulting in more reliable communication.

Using the same antenna selection procedure, the cumulative density function (CDF) of the measured normalized channel gain is plotted in Fig. 4 for the different antenna sets. Sequential antenna selection from top to bottom was used here as well and hence $\Delta h = 0.5\,\text{m}$. No significant difference in fading when going from one to two antennas is observed, i.e. when the subset is including the strongest antennas of the two top panels. When further increasing the number of antennas in the selected subset, the minimum gain level increases with steps of 1

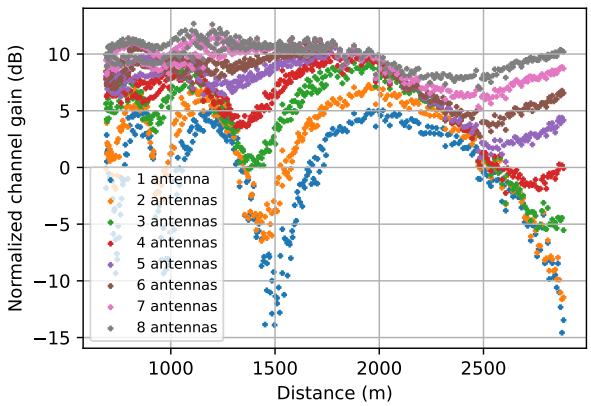

Figure 3: Normalized channel gain as a function of the distance and the number of vertically *distributed* antennas. The eight antennas are the strongest one of each panel.

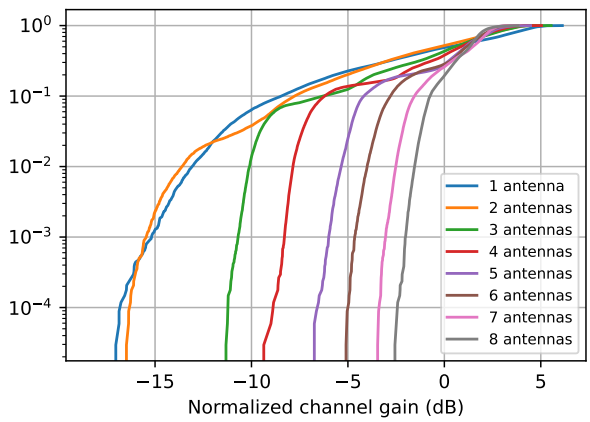

Figure 4: CDF of the normalized channel gain as a function of the number of *distributed* antennas with sequential antenna selection (top to bottom receiver antenna height)

to 5 dB with the largest gain being when going from two to three antennas. Also, note that the CDF curve for two antennas crosses the CDF curve for one antenna. This occurs because the $\|\tilde{\boldsymbol{h}}\|^2$ value of the second antenna in the set is slightly lower than that of the first antenna. After the normalization in (4.4), this results in the average channel gain being slightly lower compared to the one-antenna case. Nevertheless, one can also observe that the slope of the tail of the CDF has become steeper going from one to two antennas, indicating still a small amount of channel hardening. From these results, we can deduct that the antennas of the two top panels are still correlated and that a larger antenna spacing is needed in order to get more independent channels. This argumentation can be supported by inspecting the CDF of the channel gain when selecting antennas only within one panel, as shown in Fig. 6 for the top panel. Apart from the array gain, the reliability does not improve when adding more antennas to the subset.

Following from [8] and as summarized in Section 2, Δh could be chosen in another way to potentially improve the performance. Relating this value to the result in Fig. 1, for $M = 2$, the value 1.5 m lies between the bounds so it should result in a fading depth of around -7 dB, which is a significant improvement in comparison to the results in Fig. 4. Since the panels are spaced 0.5 m, the subset $S_2 = \{1, 4\}$ can be chosen as a suitable candidate with index 1 being the strongest antenna of the top panel and index 4 indicating the strongest antenna of the fourth highest panel. Following the same principle for the three antenna case, the subset $S_3 = \{1, 4, 7\}$ is appropriate. For higher antenna numbers, indices $\{8, 2, 3, 5, 6\}$ are added to the set in the given order. Index 8 is first added to increase to overall aperture of the array. After that, the order of the indices does not play a significant role. The results of this selection procedure can be seen in Fig. 5. By using only two antennas, the minimum gain level can be increased with about 10 dB. Finally, an increase of approximately 15 dB, in comparison to the one antenna case, can be achieved by using no more than three antennas. After this, adding more antennas to the selected subset does not contribute much to improving the reliability. The major change in terms of the slope also happens when going from one to two antennas and after that it is approximately the same, potentially as a result of that the two-ray model being an accurate model for propagation at the sea. One must however note that this more strategic selection technique relies on a given range of d wherein the fading depth is minimized and also depends on the value for h_t.

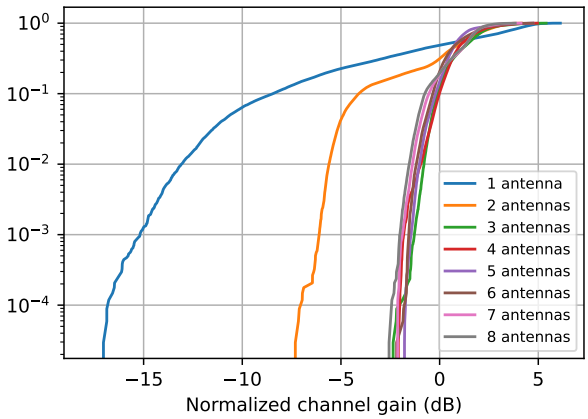

Figure 5: CDF of the normalized channel gain as a function of the number of *distributed* antennas with strategic antenna selection.

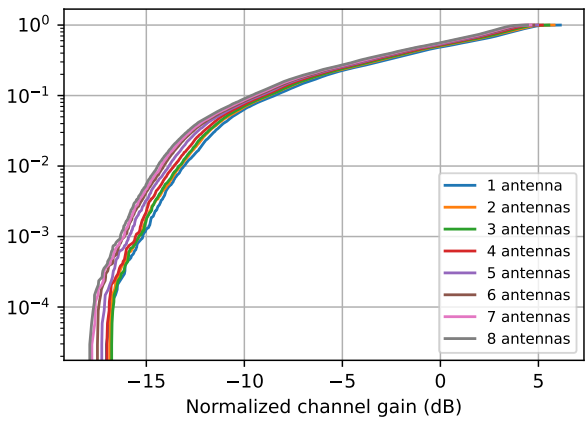

Figure 6: CDF of the normalized channel gain as a function of the number of *co-located* antennas.

6 Conclusion

Deploying multiple antennas is a highly effective strategy for combating sea surface fading. However, the performance benefits are significantly enhanced when the antennas are distributed rather than co-located, as the improved spatial diversity reduces the risk of simultaneous signal degradation at the different antennas. Moreover, careful planning of the infrastructure, particularly in terms of optimizing antenna spacing, can dramatically reduce the fading without the need for an excessive number of antennas. In this paper, it has been shown that as few as two or three base station antennas could be, depending on the application scenario, sufficient from a reliability point of view, also showing that the two-ray model is an adequate channel model for optimizing antenna spacing.

Acknowledgments

The authors would like to thank Christian Nelson, Juan Vidal Alegría, Aleksei Fedorov for their support during the measurement campaign. Additionally, the authors express their gratitude to the Royal Physiographic Society of Lund for partially funding the channel sounder.

References

[1] S. Willhammar, J. Flordelis, L. Van Der Perre, and F. Tufvesson, "Channel hardening in massive MIMO: Model parameters and experimental assessment," *IEEE Open Journal of the Communications Society*, vol. 1, pp. 501–512, 2020.

[2] S. Willhammar, L. V. D. Perre, and F. Tufvesson, "Fading in reflective and heavily shadowed industrial environments with large antenna arrays," *IEEE Open Journal of Antennas and Propagation*, pp. 1–1, 2024.

[3] H. Q. Ngo and E. G. Larsson, "No downlink pilots are needed in TDD massive MIMO," *IEEE Trans Wireless Commun*, vol. 16, no. 5, pp. 2921–2935, May 2017.

[4] X. Gao, O. Edfors, F. Rusek, and F. Tufvesson, "Massive MIMO performance evaluation based on measured propagation data," *IEEE Transactions on Wireless Communications*, vol. 14, no. 7, pp. 3899–3911, July 2015.

[5] K. Yang, A. F. Molisch, T. Ekman, T. Røste, and M. Berbineau, "A Round Earth Loss Model and Small-Scale Channel Properties for Open-Sea Radio Propagation," *IEEE Transactions on Vehicular Technology*, vol. 68, no. 9, pp. 8449–8460, Sep. 2019.

[6] M. Sandra, G. Tian, A. Fedorov, X. Cai, and A. J. Johansson, "Measurement-Based Wideband Maritime Channel Characterization," *The 17th European Conference on Antennas and Propagation (EuCAP 2023)*, 2023.

[7] W. Wang, G. Hoerack, T. Jost, R. Raulefs, M. Walter, and U.-C. Fiebig, "Propagation channel at 5.2 GHz in baltic sea with focus on scattering phenomena," in *2015 9th European Conference on Antennas and Propagation (EuCAP)*, Apr. 2015, pp. 1–5.

[8] M. Sandra, G. Tian, X. Cai, and A. J. Johansson, "Antenna Array Configuration for Reliable Communications in Maritime Environments," in *2022 IEEE 95th Vehicular Technology Conference: (VTC2022-Spring)*, Jun. 2022, pp. 1–5, iSSN: 2577-2465.

[9] M. Sandra, C. Nelson, X. Li, X. Cai, F. Tufvesson, and A. J. Johansson, "A Wideband Distributed Massive MIMO Channel Sounder for Communication and Sensing," Tech. Rep., Mar. 2024, arXiv:2403.11856 [eess] type: article. [Online]. Available: http://arxiv.org/abs/2403.11856

[10] B. Fleury, M. Tschudin, R. Heddergott, D. Dahlhaus, and K. Ingeman Pedersen, "Channel parameter estimation in mobile radio environments using the SAGE algorithm," *IEEE Journal on Selected Areas in Communications*, vol. 17, no. 3, pp. 434–450, Mar. 1999.

Leveraging the Two-Ray Model for C-band Ranging in Maritime Applications

Michiel Sandra, Markus Wirsing, Sara Willhammer,
Ronald Raulefs, Anders J Johansson

Paper V

Published as: M. Sandra, M. Wirsing, S. Willhammar, R. Raulefs, A. J. Johansson, "Leveraging the Two-Ray Model for C-band Ranging in Maritime Applications," *Submitted to IEEE Transactions on Vehicular Technology*, 2025.

Abstract

We present a novel ranging method based on channel estimates between an antenna on a vessel at sea and a land-based base station equipped with a vertical antenna array, leveraging the range information embedded in the two-ray model. Compared to delay-based ranging approaches, such as Time of Arrival (ToA), our approach uses only the spatial domain of the channel, eliminating the need for time synchronization between base stations and the requirement for high bandwidth for accurate delay estimation. This ranging method is therefore suitable as a backup positioning system when the Global Navigation Satellite System (GNSS) malfunctions, as it operates independently without relying on GNSS for time synchronization. Through Cramér-Rao bound analysis, we show that sufficient antenna spacing is crucial to combat two-ray fading, which heavily impacts the ranging performance. Knowledge of the vessel's antenna height also significantly affects the accuracy of the ranging. Implementation of this method, verified by measurements, revealed four practical challenges: calibration of the hardware contributions to the channel, calibration of the antenna phase centers, knowledge of the vessel's instantaneous antenna height, and characterization of the sea surface reflection. To address these challenges, we developed a channel model that incorporates the necessary calibration parameters and a corresponding estimation algorithm. We compared the estimated coherent sea surface reflection with existing models and characterized it empirically using a generalized rough surface reflection model. We also found that the sailboat antenna height is a non-stationary process. However, we could use the local mean height obtained via the IMU data to filter out local height changes through a Kalman filter. Final results show a root mean square error of 6.3 m (700-2800 m distance), highlighting its potential as a GNSS backup.

1 Introduction

The increasing importance of positioning and navigation at sea has become even clearer in recent years given the demand to support applications such as navigation, vessel tracking, and autonomous shipping. Global Navigation Satellite Systems (GNSSs) have been essential for this purpose, but can sometimes be unreliable or faulty, necessitating the need for alternative positioning solutions, especially in critical scenarios [1]. Such critical scenarios are evident in high density of moving vessels, or tight water streets with limited water depth, and also maneuver inside harbors with or without pilot boats. By incorporating terrestrial networks (TNs) and non-terrestrial networks (NTNs), 6G aims to broaden maritime connectivity even in sparsely populated coastal zones [2]. These networks are expected to utilize higher carrier frequencies than conventional maritime communications in the very high frequency (VHF) band, thereby offering substantially more spectrum and capacity for a variety of critical communication needs. The

International Maritime Organization (IMO), in its circular MSC.1/Circ.1575 [3], published guidelines for shipborne Position, Navigation, and Timing (PNT) data processing. These guidelines seek to improve navigational safety and efficiency by establishing a modular framework for processing PNT data from multiple sensors and services, thus providing bridge teams and onboard applications with robust and reliable information. They further emphasize the importance of resilience through multi-system diversity. With the advent of 5G, the maritime industry is visibly engaged for the first time in developing use cases that leverage these cellular mobile radio systems for broadband communication and navigation [4]. In the event of a GNSS outage, obtaining accurate timing data becomes both extraordinarily difficult and critically important. Because 5G positioning relies primarily on time-based ranging methods using specific positioning reference signals, their dependence on GNSS timing remains high, highlighting the need for reliable and redundant solutions. One major concern is the risk of signal interference and jamming, since GNSS signals can be deliberately jammed or spoofed by malicious actors, leading to false or inaccurate positioning data. This issue has even been highlighted by key institutions responsible for maritime safety (IMO) and spectrum management (International Telecommunication Union, ITU) [5]. The method presented in this paper expands current solutions by adding the essential capability of less strict time-dependent ranging.

Ranging is a fundamental component of multilateration, as it involves measuring the distance between a target and multiple reference points to accurately determine the target's position. These estimates are typically obtained through time-based ranging methods, which measure the signal propagation delay or time-of-flight (ToF). Common approaches include one-way time-of-arrival (ToA) ranging, two-way ToA ranging, and time-difference-of-arrival (TDoA) [6], [7]. One-way ToA ranging requires nanosecond-level synchronization between the vessel and base stations, which can be technically demanding. In contrast, two-way ranging estimates the range based on round-trip signal time and does not require a common time reference, but instead depends on the relative clock drift [6]. However, it requires at least two transmissions per base station, increasing communication overhead and limiting scalability. TDoA eliminates the need for synchronization between the vessel and the base stations, but requires tight time synchronization among the base stations themselves.

Unlike these ranging methods, we analyze and validate a novel one-way ranging method that does not require strict time synchronization between the vessel and the base station or between the base stations themselves. The proposed

method utilizes channel measurements from a large vertical base station antenna array to estimate the range. Information about the range to a vessel is embedded in the amplitude and phase differences among the antennas because of the two-ray propagation environment at sea. Because only amplitude and phase measurements are sufficient to estimate the range, there is no requirement for time synchronization. However, phase-coherent reception is required on the base station side. In [8], it was also shown that vertically distributed antennas were useful in mitigating the effects of large-scale fading caused by the sea surface, motivating this type of antenna configuration for maritime applications. We summarize the contributions of this paper as follows:

- We perform a theoretical analysis of the ranging performance and derive the Cramér–Rao lower bound in closed form, which also provides insight into antenna spacing.
- In order to verify the novel ranging method experimentally, we have performed a measurement campaign with a large vertical array on land and a single transmit antenna on top of a sailboat.
- Learning from our measurements, we develop a novel channel model, and corresponding estimation algorithm, which takes into account the RF hardware contributions and phase center offsets of the antennas. The estimation algorithm could be seen as an over-the-air calibration algorithm, which could be directly employed in a real-world application. In contrast to other models, where the specular reflection coefficient is derived from theories such as rough surface scattering, our approach treats the reflection coefficient as an unknown parameter to be estimated. This methodology allows for independent characterization of the reflection coefficient, also contributing to the field of channel modeling.

One of the limitations of this paper is that the ranging method is not validated for distances larger than 2800 m due to the lack of measurement data. The paper is structured as follows. First, we introduce the ranging problem and perform a theoretical investigation in Section 2. The measurement equipment and campaign are presented in Section 3. The channel model and parameter estimation are then elaborated in Section 4. This is followed by Section 5, which includes the estimation results for the overall model, the calibration parameters, the reflection coefficient, and the height of the antenna on the vessel. Section 6 assesses the real-world ranging performance. Conclusions are drawn in Section 7.

2 The Ranging Problem

In this section, we introduce the problem of estimating the distance or range between a vessel at sea and a base station on land based on propagation channel measurements. The base station has a vertical uniform linear antenna array with M antennas and the vessel has a single antenna.

2.1 Channel Model

At the basis of this paper lies the assumption that the maritime channel can be modeled by a two-ray model [9]. This assumption is valid when (1) there is no obstruction of the line-of-sight connection between the vessel and the base station, (2) the sea surface is the dominant scatterer, and (3) diffraction loss is negligible. This means that the vessel is in the coastal range, several kilometers from the shore. A common approach to modeling the maritime channel is to take the two-ray model as a basis and modify the reflection coefficient according to the sea surface roughness [10–13]. Additionally, the curvature of the Earth affects the geometry of the two-ray model. This effect is addressed by the round-Earth two-ray model [8, 13], which also accounts for atmospheric refractivity by adjusting the true Earth's radius to an "effective" Earth radius [14]. For larger distances, diffraction loss must also be considered; however, it is negligible for the coastal ranges considered in this paper. To introduce the problem and conduct an initial analysis, we adopt the planar two-ray model, thereby neglecting both the Earth's curvature and atmospheric refractivity; these factors, however, will be incorporated into the final ranging solution in Section 4. Let us formulate the complex propagation channel between the vessel and the base station $\boldsymbol{g} \in \mathbb{C}^{M\times 1}$ as

$$[\boldsymbol{g}]_i = \beta \left(1 + \rho_i \exp \frac{-\mathrm{j}4\pi h_\mathrm{t} h_\mathrm{r,i}}{\lambda d} + \chi_i\right), \tag{2.1}$$

where:

- $i \in [1, \ldots, M]$ is the antenna index,
- $\beta \in \mathbb{C}$ is a nuisance parameter that takes into account the changes in the propagation channel, which are the same for all antennas, such as the free-space path loss. The antennas are assumed to be identical and their contributions to the propagation channel are also captured by β,
- $\rho_i \in \mathbb{C}$ is the coherent reflection coefficient of the sea surface,

- $h_\mathrm{t} \in \mathbb{R}$ and $h_\mathrm{r} \in \mathbb{R}$ are the transmitter and receiver antenna heights, respectively,
- $\lambda \in \mathbb{R}$ is the wavelength,
- $d \in \mathbb{R}$ is distance over ground between the vessel and the base station,
- $\chi_i \in \mathbb{C}$ is the random incoherent scattering component.

2.2 Maximum Likelihood Range Estimation

According to the two-ray model, the range d can be estimated utilizing the delay difference between the line-of-sight component and the sea surface reflection. Jointly estimating these delays requires an unrealistic bandwidth. However, with a vertical ULA at shore, the amplitude and phase differences between the signals at vertically distributed antennas can be utilized to estimate d, even in a narrowband system. If all the parameters in (2.1) except d are known and the array is phase calibrated, d could be estimated by maximizing the likelihood. Let us denote the measured channel response as a vector $\boldsymbol{y} \in \mathbb{C}^{M\times 1}$:

$$\boldsymbol{y} = \boldsymbol{g} + \boldsymbol{\omega} \tag{2.2}$$

where $\boldsymbol{g} \in \mathbb{C}^{M\times 1}$ is the narrowband channel response. $\boldsymbol{\omega} \in \mathbb{C}^{M\times 1}$ is the i.i.d. Gaussian measurement noise. Assuming that also $\boldsymbol{\chi} \sim \mathcal{CN}(\mathbf{0}, \sigma_\chi^2 \mathbf{I}_M)$, the maximum-likelihood estimator (MLE) can be formulated as follows:

$$\hat{d} = \underset{d}{\operatorname{argmax}} \frac{1}{\sigma_\chi^2 + \sigma_\omega^2} \frac{|\boldsymbol{y}^H \boldsymbol{g}(d)|^2}{\|\boldsymbol{g}(d)\|^2}, \tag{2.3}$$

$$\hat{\beta} = \frac{\boldsymbol{g}(\hat{d})^H \boldsymbol{y}}{\|\boldsymbol{g}(\hat{d})\|^2}, \tag{2.4}$$

with

$$[\boldsymbol{g}(d)]_i = 1 + \rho_i \exp \frac{-\mathrm{j}4\pi h_\mathrm{t} h_{\mathrm{r,i}}}{\lambda d}. \tag{2.5}$$

2.3 Cramér-Rao Lower Bound

The variance of $\hat{d}$ is lower bounded by the Cramér-Rao Lower Bound (CRLB), which can be obtained by calculating the Fischer information matrix [15] and

inverting a 3×3 matrix. The final result can be expressed as

$$\sigma_{\hat{d}}^2(d,\beta) \geq \frac{\frac{1}{2}\frac{\sigma_\chi^2 + \sigma_\omega^2}{|\beta|^2}}{\left\| \frac{\partial \boldsymbol{g}(d)}{\partial d} \right\|^2 - \frac{\left| \boldsymbol{g}(d)^H \frac{\partial \boldsymbol{g}(d)}{\partial d} \right|^2}{\|\boldsymbol{g}(d)\|^2}}. \tag{2.6}$$

From (2.6), we can observe a difference of two positive terms in the denominator. The first term originates from the uncertainty of d. If β were known, then the second term would disappear. It would be desirable for the ranging performance if the second term is much smaller than the first term. The first term can be further formulated as

$$\left\| \frac{\partial \boldsymbol{g}(d)}{\partial d} \right\|^2 = \left(\frac{4\pi h_\mathrm{t}}{\lambda d^2} \right)^2 \sum_{i=1}^{M} |\rho_i|^2 h_{\mathrm{r},i}^2. \tag{2.7}$$

The value of (2.7) can be maximized by placing all antenna elements at the same maximum height. However, little or no antenna spacing is known to be subject to deep fades due to the sea surface reflection [8]. If a deep fade occurs, the channel gain $\|\boldsymbol{g}\|^2$ becomes small and the second term could reach a large value, degrading the estimation performance. Hence, the ranging performance is strongly affected by deep fades caused by the sea surface. In [8], the distance interval boundaries where deep fading does not occur have been derived for a vertical uniform linear array (ULA). Now, assume that the antenna spacing has been optimized so that within that interval the deep fades are mitigated, that is, $\|\boldsymbol{g}\|^2 > M$. Consequently, the estimate of β will have a low variance and the effect on the variance of $\hat{d}$ will be minimal. Hence, the second term in the denominator of (2.6) can be omitted, while the bound remains sufficiently tight. Now, the lower bound of (2.6) becomes

$$\sigma_{\hat{d}}^2(d,\beta) \geq \frac{\frac{1}{2}\frac{\sigma_\chi^2 + \sigma_\omega^2}{|\beta|^2}}{\left(\frac{4\pi h_\mathrm{t}}{\lambda d^2} \right)^2 \sum_{i=1}^{M} |\rho_i|^2 h_{\mathrm{r},i}^2}. \tag{2.8}$$

The two bounds are depicted in Fig. 1 for the antenna configuration of our measurement, explained in Section 3 with an SNR of 20 dB. The figure shows that the alternative bound in (2.8) is indeed tight to (2.6). An important conclusion we can draw from (2.8), is that the variance of the range estimate scales with d^4, which is not very desirable. However, utilizing (2.8), one could assess the viability

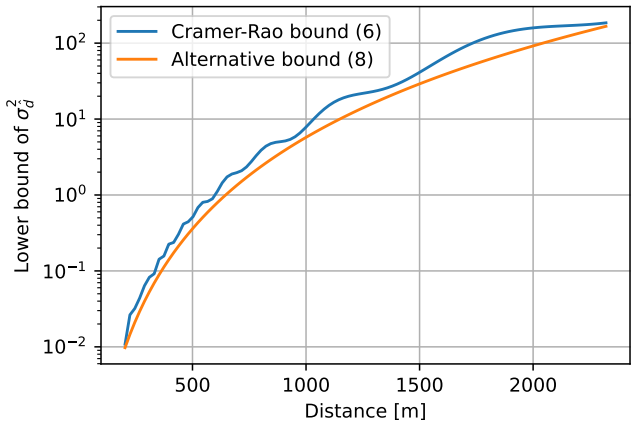

Figure 1: Cramér-Rao bound for range estimation using the two-ray model. $|\beta|^2/(\sigma_\chi^2 + \sigma_\omega^2) = 20\,\text{dB}$.

of range estimation for the considered system configuration. A Bayesian filter, such as a Kalman filter, would be quite effective in reducing error variance, as the filter estimates the range based on all previous measurements, leading to a more accurate and stable range estimate, see Section 6.

2.4 Transmitter Height Bias

So far, it has been assumed that all parameters except d are known. However, a vessel can be subject to small height variations due to the dynamic sea surface. From (2.1), it can be observed that the same ratio of h_t and d gives the same (scaled) channel response. When there is an error in the transmit height, there can be a significant error in the range:

$$\Delta d = \frac{d}{h_\text{t}} \Delta h_\text{t}, \tag{2.9}$$

where Δd and Δh_t are the respective errors in distance and transmit height. For $h_t = 10\,\text{m}$ and $d = 1\,\text{km}$, a transmit height error of 10 cm results in a ranging error of 10 m. If we model the antenna height as a normal distribution, i.e. $h_\text{t} \sim \mathcal{N}(\mu_{h_\text{t}}, \sigma_{h_\text{t}}^2)$, we can account for the effect of the variations of the antenna height on the range estimate and obtain a better prediction of its variance. By

Figure 2: Photographs of the sailboat (Tx) and the vertical array (Rx) ashore.

adding a term to (1) based on (2.9), the variance of $\hat{d}$ could be approximated by

$$\sigma_{\hat{d}}^2(d,\beta) \geq \frac{\frac{1}{2}\frac{\sigma_\chi^2+\sigma_\omega^2}{|\beta|^2}}{\left(\frac{4\pi h_\mathrm{t}}{\lambda d^2}\right)^2 \sum_{i=1}^{M} |\rho_i|^2 h_{\mathrm{r},i}^2} + \left(\frac{d}{\mu_{h_\mathrm{t}}}\right)^2 \sigma_{\hat{h}_\mathrm{t}}^2. \tag{2.10}$$

3 Measurement equipment and campaign

A measurement campaign was carried out in Klagshamn, Sweden (N 55.523° E 12.895°), in September 2023. A single-antenna transmitter was mounted on a sailboat at a height of approximately 10 m above sea level. The receiver side consisted of an antenna array installed on land with the top antenna positioned at 8.1 m above sea level, which can be seen in Fig. 2. The eight panels were vertically distributed with a spacing of 0.5 m, each consisting of 4×2 dual-polarized antennas, adding up to 128 antenna ports in total.

To measure the channel, a channel sounder based on the NI USRP X410 was used [16]. The eight radio frequency (RF) chains were connected to one panel each, as well as a low-noise amplifier (LNA) and a SP16T RF switch to iterate through the ports of each panel, making the channel sounder a hybrid-switched one. To increase the dynamic range of the system, a power amplifier was used at the transmitter side. During the measurement, a sounding signal was transmitted with a carrier frequency of 5.6 GHz and 250 MHz bandwidth every 5 ms. The snapshots were collected during the two-hour sailing in open sea, following

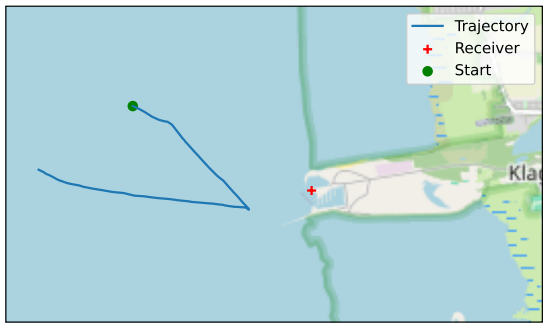

Figure 3: Trajectory of the sailboat during the measurement.

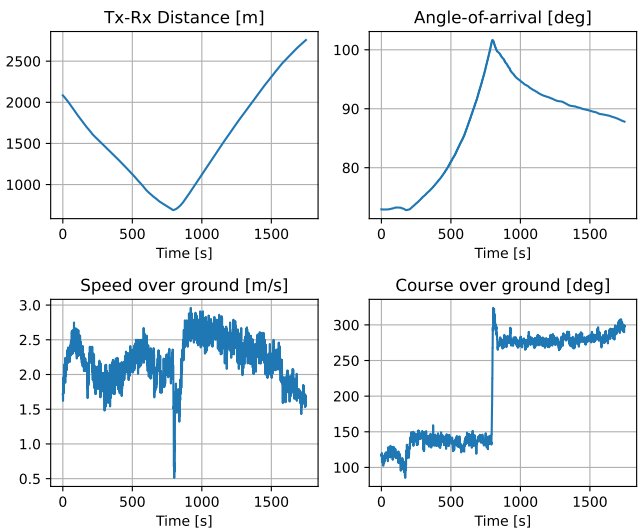

Figure 4: Tx-Rx distance, speed over ground, angle-of-arrival at the Rx, and course over ground as a function of time.

the trajectory displayed in Fig. 3 and the distance, angle-of-arrival, course and speed over ground in Fig. 4. The sea conditions at the time of measurement corresponded to approximately Beaufort scale 3, with a wind speed between 4 and 6 m/s. An RTK GNSS receiver (SwiftNav DURO), equipped with an integrated inertial measurement unit (IMU), was used as the ground truth positioning system. The receiver was mounted on the deck of the sailboat. Using the roll and pitch angles provided by the IMU, together with the known relative position of the transmit antenna with respect to the receiver, the height of the transmit antennas could be accurately estimated. An overview of the configuration parameters and the corresponding performance metrics of the channel sounder is presented in Table I.

4 Calibrated Channel Model and Parameter Estimation

4.1 Channel Model

Let $\boldsymbol{\mathcal{Y}} \in \mathbb{C}^{M\times N\times F}$ denote the measured channel response acquired from the channel sounder, where M is the number of antennas, N the number of channel snapshots in time, and F is the number of frequency points, equally spaced over the bandwidth. The tensor $\boldsymbol{\mathcal{Y}}$ can be expressed as

$$\boldsymbol{\mathcal{Y}} = \boldsymbol{\mathcal{G}} + \boldsymbol{\mathcal{N}}, \tag{4.1}$$

where $\boldsymbol{\mathcal{G}} \in \mathbb{C}^{M\times N\times F}$ is the channel response and $\boldsymbol{\mathcal{N}} \in \mathbb{C}^{M\times N\times F}$ is the noise. Due to the sparse scattering and the low delay spread in *open-sea* maritime propagation environments, especially when using directive antennas pointed at

Table 1: Configuration of the channel sounder

Description	**Value**
Center frequency	5.6 GHz
Bandwidth	250 MHz
Total number of transmit antennas	1
Total number of receive antenna	128
Transmit power at the antenna	20 dBm
Snapshot rate	200 Hz
Snapshot duration	2.5 ms
Max. delay spread	8μ
Max. Doppler frequency	100 Hz

the sea, the channel can be considered frequency-flat or narrowband. This means that most of the channel information can be captured with one frequency point. For modeling purposes, the narrowband channel response is extracted from the wideband channel measurements. This reduces the noise level as well as the computational complexity for the parameter estimation later on. To do this, the multipath components (MPCs) are extracted for each snapshot and antenna and then used to reconstruct the narrowband channel response. This process reduces the level of noise and narrowband interference. The underlying signal model of $\boldsymbol{\mathcal{Y}}$ can then be expressed as

$$[\boldsymbol{\mathcal{Y}}]_{ijk} = \sum_{\ell=1}^{L_{ij}} \alpha_{\ell,ij} \exp\left(-\mathrm{j}2\pi f_k \tau_{\ell,ij}\right) + n_{\ell,ijk}, \tag{4.2}$$

where $\alpha_{\ell,ij}$ and $\tau_{\ell,ij}$ indicate the complex amplitude and delay of the ℓ-th MPC, respectively. The scalar f_k is the absolute frequency of the k-th subcarrier and L_{ij} is the observed number of MPCs. The space-alternating generalized expectation-maximization (SAGE) algorithm is applied to estimate $\alpha_{\ell,ij}$ and $\tau_{\ell,ij}$. The measured narrowband channel $\boldsymbol{Y} \in \mathbb{C}^{M\times N}$ can now be calculated as

$$[\boldsymbol{Y}]_{ij} = \sum_{\ell=1}^{L_{ij}} \hat{\alpha}_{\ell,ij} \exp\left(-\mathrm{j}2\pi f_0 \hat{\tau}_{\ell,ij}\right), \tag{4.3}$$

where f_0 is the absolute frequency at which the narrowband channel is reconstructed, which is set to 5.6 GHz. Next, $\boldsymbol{Y}$ is to be expressed using the basic two-ray model from (2.1). However, since dealing with real-world channel measurements, there are two additional aspects that have to be captured by the model. First, there is the relative phase difference between the RF channels of the channel sounder. The channel sounder does not support absolute phase synchronization between the RF channels; hence, it should be taken into account in the channel parameter estimation. Second, the relative positions of the phase centers of the antennas in the antenna array must be considered. Due to the large size of the array and the flexibility of our antenna mast, the phase centers of the antenna elements are not perfectly aligned on a virtual line that goes through the center of the Earth. Consequently, the angle-of-arrival and the relative antenna phase center positions need to be considered in the channel model. Lets express $\boldsymbol{Y}$ as

$$\boldsymbol{Y} = \boldsymbol{G} + \boldsymbol{N}, \tag{4.4}$$

where $\boldsymbol{N} \in \mathbb{C}^{M \times N}$ is the measurement noise and $\boldsymbol{G} \in \mathbb{C}^{M \times N}$ is the narrowband channel model, which equates to

$$[\boldsymbol{G}]_{ij} = \alpha_i \beta_j \exp\left(-\mathrm{j}\frac{2\pi}{\lambda}(r_{\mathrm{los},ij} + \Delta r_i \cos(\phi_j - \psi_i))\right) \times \left(1 + \rho_{ij} \exp\left(\frac{-\mathrm{j}4\pi h'_{\mathrm{r},ij} h'_{\mathrm{t},ij}}{\lambda d_j}\right) + \chi_{ij}\right), \tag{4.5}$$

where:

- $i \in [1, \ldots, M]$ is the antenna index,
- $j \in [1, \ldots, N]$ is the snapshot index,
- $\alpha_i \in \mathbb{C}$ models the time-invariant relative amplitude and phase differences between the channels, e.g. the hardware contributions. The values for α_i are relative to the first channel/antenna, i.e. $\alpha_1 = 1$. Note that α is re-defined here and the old definition in (4.3) can be omitted,
- $\beta_j \in \mathbb{C}$ is a nuisance parameter that models the free space loss and changes in the channel which have the same effect on all channels. These changes include phase rotations due to increasing distance between the transmitter and the receiver array, polarization mismatch, changes in the transmit antenna response due to changing orientation, or changes in the receive antenna response due to changing angle of arrival. For the latter, it is assumed that the antennas have a similar antenna pattern and the same orientation,
- $\lambda \in \mathbb{R}$ is the wavelength,
- d_j is the great-circle distance between the transmit antenna and receiver array. The phase center position of the first receiving antenna is chosen as reference for the receiver array,
- $h'_{\mathrm{r},ij} \in \mathbb{R}$ is the modified receive antenna height of the i-th antenna, and is expressed as

  $$h'_{\mathrm{r},ij} = h_{\mathrm{r},i} - \frac{1}{2}\left(\frac{h_{\mathrm{r},i}}{h_{\mathrm{t},j} + h_{\mathrm{r},i}}\right)^2 \frac{d_j^2}{r_{\mathrm{e}}}, \tag{4.6}$$

  where $h_{\mathrm{r},i} \in \mathbb{R}$ is the receive antenna height above sea level and r_{e} is the effective Earth radius [8],

- $h'_{\mathrm{t},ij} \in \mathbb{R}$ is the modified transmit antenna at the j-th snapshot, and is expressed as

$$h'_{\mathrm{t},ij} = h_{\mathrm{t},j} - \frac{1}{2}\left(\frac{h_{\mathrm{t},j}}{h_{\mathrm{t},j} + h_{\mathrm{r},i}}\right)^2 \frac{d_j^2}{r_{\mathrm{e}}}, \tag{4.7}$$

  where $h_{\mathrm{t},j} \in \mathbb{R}$ is the transmit antenna height above sea level [8],

- d_j is the great-circle distance between the transmit antenna and receiver array. The phase center position of the first receiving antenna is chosen as reference for the receiver array,

- $\phi_j \in \mathbb{R}$ is the angle of arrival and is calculated based on the position of the transmitter and receiver,

- $\psi_i \in \mathbb{R}$ and $\Delta r_i \in \mathbb{R}$ model the antenna phase center positions relative to the first antenna in polar coordinates. For the first antenna, ψ_1 and Δr_1 are set to 0,

- $r_{\mathrm{los},ij} \in \mathbb{R}$ is the Euclidean distance between the transmit antenna and the i-th receive antenna $r_{\mathrm{los},ij}$ at time j, and is calculated as

$$r_{\mathrm{los},ij} = \sqrt{(h'_{\mathrm{t},ij} - h'_{\mathrm{r},ij})^2 + d_j^2}. \tag{4.8}$$

- $\rho_{ij} \in \mathbb{C}$ is the reflection coefficient of the sea surface. Since it is not possible to estimate ρ_{ij} for each (i, j) – although it would be of great interest – it is here assumed that ρ_{ij} follows some stationary distribution for a certain time frame and a range of angles of incidence. In this way, a reflection coefficient, with multiple entries of $\boldsymbol{Y}$, can be estimated. Lets define K sets $\mathcal{R}_k$, where $k \in [1, \ldots, K]$, of incidences (i, j) for which the associated angles of incidence are similar, then ρ_{ij} can be generally formulated as

$$\rho_{ij} = \overline{\rho}_k, \text{ if } (i, j) \in \mathcal{R}_k. \tag{4.9}$$

  The choice of $\mathcal{R}_k$ can be observed in Fig. 5.

- $\chi_{ij} \in \mathbb{C}$ is the diffuse component of the sea surface reflection. χ_{ij} has to be modeled as a random variable where the real and imaginary parts follow a distribution. In literature, this distribution is often assumed to be Gaussian, but little is known about the typical variance and its behavior. Its variance has to be derived through an empirical analysis because it is dependent on the sea state.

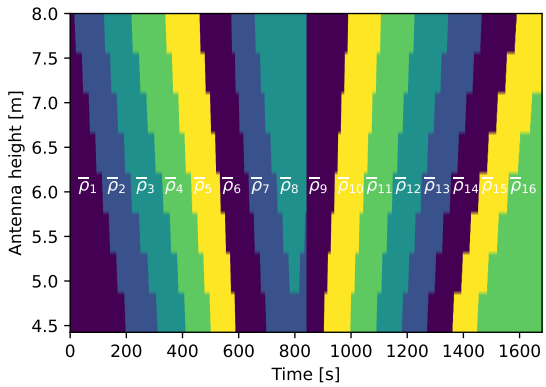

Figure 5: Visualization of $\overline{\rho}$. The colors show where region in which the reflection coefficient is averaged.

4.2 Parameter Estimation

In this section, we present the algorithm to estimate the parameters $\overline{\rho}_k$, α_i, β_j, Δr_i, ψ_i, and $h_{\mathrm{t},j}$. All other parameters are available from other measurements, e.g. d_j is calculated from the RTK GNSS measurements. The parameters are written as vectors: $\boldsymbol{\alpha} = \left[\alpha_2, \ldots, \alpha_M\right]^T$, $\boldsymbol{\beta} = \left[\beta_1, \ldots, \beta_N\right]^T$, $\boldsymbol{\Delta r} = \left[\Delta r_2, \ldots, \Delta r_M\right]^T$, $\boldsymbol{\psi} = \left[\psi_2, \ldots, \psi_M\right]^T$. $\overline{\boldsymbol{\rho}} = \left[\overline{\rho}_1, \ldots, \overline{\rho}_K\right]^T$, and $\boldsymbol{h_t} = \left[h_{\mathrm{t},1}, \ldots, h_{\mathrm{t},N}\right]^T$; and summarized as $\boldsymbol{\theta} = \left[\boldsymbol{\alpha}, \boldsymbol{\beta}, \boldsymbol{\Delta r}, \boldsymbol{\psi}, \overline{\boldsymbol{\rho}}, \boldsymbol{h_t}\right]^T$. Interpreting the complex parameters as two separate parameters, the total number of parameters to be estimated is given by $4(M-1)+K+3N$. Due to the lack of reliable information on the distribution of χ_{ij}, we assume that the power of the incoherent component, as it is believed to originate from diffuse scattering, is related to the power of the line-of-sight component. We also lack reliable information on the distribution of χ_{ij}. Therefore, a weighted non-linear least squares estimator is used, assuming that χ_{ij} is zero-mean distributed and that the realizations are uncorrelated. The estimation problem is formulated as follows:

$$\hat{\boldsymbol{\theta}} = \underset{\boldsymbol{\theta}}{\operatorname{argmin}} \left\| \tilde{\boldsymbol{Y}} - \boldsymbol{G}(\boldsymbol{\theta}) \right\|_F^2, \tag{4.10}$$

with

$$[\tilde{\boldsymbol{Y}}]_{ij} = [\boldsymbol{Y}]_{ij} / \frac{\lambda}{4\pi d_j}. \tag{4.11}$$

This is a challenging, high-dimensional non-convex optimization problem. By rewriting (4.10) as

$$\hat{\boldsymbol{\theta}} = \underset{\boldsymbol{\theta}}{\operatorname{argmin}} \sum_{j=1}^{N} \left\| \tilde{\boldsymbol{y}}_j - \beta_j \, \boldsymbol{g}_j(\boldsymbol{\alpha}, \boldsymbol{\Delta r}, \boldsymbol{\psi}, \overline{\boldsymbol{\rho}}, h_{\mathrm{t},j}) \right\|^2, \tag{4.12}$$

where

$$\begin{aligned}[\boldsymbol{g}_j]_i = &\alpha_i \, \exp\left(-\mathrm{j} \frac{2\pi}{\lambda} (r_{\mathrm{los},ij} + \Delta r_i \cos(\phi_j - \psi_i)) \right) \\ &\times \left(1 + \rho_{ij} \exp\left(\frac{-\mathrm{j}4\pi h'_{\mathrm{r},ij} h'_{\mathrm{t},ij}}{\lambda d_j} \right) \right),\end{aligned} \tag{4.13}$$

the dimensionality of the optimization problem can be further reduced by $2N$ by plugging the ordinary least squares estimate for β_j, given by

$$\hat{\beta}_j = \frac{\boldsymbol{g}_j(\boldsymbol{\alpha}, \boldsymbol{\Delta r}, \boldsymbol{\psi}, \overline{\boldsymbol{\rho}}, h_{\mathrm{t},j})^H \tilde{\boldsymbol{y}}_j}{\| \boldsymbol{g}_j(\boldsymbol{\alpha}, \boldsymbol{\Delta r}, \boldsymbol{\psi}, \overline{\boldsymbol{\rho}}, h_{\mathrm{t},j}) \|^2}, \tag{4.14}$$

into (4.12), resulting in the following optimization problem:

$$\hat{\boldsymbol{\alpha}}, \hat{\boldsymbol{\Delta r}}, \hat{\boldsymbol{\psi}}, \hat{\overline{\boldsymbol{\rho}}}, \hat{\boldsymbol{h}_{\mathrm{t}}} = \underset{\boldsymbol{\alpha}, \boldsymbol{\Delta r}, \boldsymbol{\psi}, \overline{\boldsymbol{\rho}}, \boldsymbol{h}_{\mathrm{t}}}{\operatorname{argmax}} \sum_{j=1}^{N} \frac{|\boldsymbol{g}_j(\boldsymbol{\alpha}, \boldsymbol{\Delta r}, \boldsymbol{\psi}, \overline{\boldsymbol{\rho}}, h_{\mathrm{t},j})^H \tilde{\boldsymbol{y}}_j|^2}{\| \boldsymbol{g}_j(\boldsymbol{\alpha}, \boldsymbol{\Delta r}, \boldsymbol{\psi}, \overline{\boldsymbol{\rho}}, h_{\mathrm{t},j}) \|^2}. \tag{4.15}$$

A quasi-Newton method can be applied to solve the optimization problem if the problem can be initialized well. Therefore, we have developed a robust initialization procedure that is explained in the following paragraphs.

We find the initial values for $\boldsymbol{\alpha}, \boldsymbol{\Delta r}, \boldsymbol{\psi}, \overline{\boldsymbol{\rho}}, \boldsymbol{h}_{\mathrm{t}}$ by first solving two optimization problems with lower dimensions. From (4.13), we can observe that a certain range of ϕ_j is needed to be able to estimate Δr_i and ψ_i to avoid phase ambiguity with α_i. If the changes of ϕ_j are small over time, then Δr_i and ψ_i could be left out of the model by setting them to 0. Given this, we segmentalize the measurements and channel model in time segments of length W during which ϕ_j does not change significantly, eliminating the need for parameters Δr_i and ψ_i. Instead, we estimate α_i for each segment separately. Following a similar procedure as before, we formulate the estimation problem as follows:

$$\hat{\tilde{\boldsymbol{\alpha}}}, \hat{\overline{\boldsymbol{\rho}}}, \hat{\boldsymbol{h}_t} = \underset{\tilde{\boldsymbol{\alpha}}, \overline{\boldsymbol{\rho}}, \boldsymbol{h}_t}{\operatorname{argmax}} \sum_{j=1}^{N} \frac{|\tilde{\boldsymbol{g}}_j(\tilde{\boldsymbol{\alpha}}, \overline{\boldsymbol{\rho}}, h_{\mathrm{t},j})^H \tilde{\boldsymbol{y}}_j|^2}{\| \tilde{\boldsymbol{g}}_j(\tilde{\boldsymbol{\alpha}}, \overline{\boldsymbol{\rho}}, h_{\mathrm{t},j}) \|^2}, \tag{4.16}$$

where $\tilde{\boldsymbol{\alpha}}$ collects the α_i for each segment s, denoted as $\tilde{\alpha}_i^s$, and $\tilde{\boldsymbol{g}}_j$ is expressed as

$$[\tilde{\boldsymbol{g}}_j]_i = \tilde{\alpha}_i^s \exp -\mathrm{j} \frac{2\pi \, r_{\mathrm{los},ij}}{\lambda} \left(1 + \rho_{ij} \exp\left(\frac{-\mathrm{j}4\pi h'_{\mathrm{r},ij} h'_{\mathrm{t},ij}}{\lambda d_j} \right) \right), \tag{4.17}$$

with the index $s = \lceil \frac{j}{W} \rceil$ indicating the segment. The parameters $\overline{\boldsymbol{\rho}}$ are initialized according to the Fresnel equations using the mean angle of incidence of a set. The heights of the transmit antenna $\boldsymbol{h}_t$ are initialized by the local mean of the transmit antenna data obtained from the IMU and RTK data. The RF chain parameters $\tilde{\boldsymbol{\alpha}}$ are initialized using a singular value decomposition:

$$\boldsymbol{U}^s \boldsymbol{\Sigma}^s (\boldsymbol{V}^s)^H = \tilde{\boldsymbol{Y}}^s \oslash \tilde{\boldsymbol{G}}^s, \tag{4.18}$$

where $\tilde{\boldsymbol{Y}}^s$ are the measurements corresponding to the first segment, i.e. a sub-matrix of $\tilde{\boldsymbol{Y}}$ and $[\tilde{\boldsymbol{G}}^s]_{ij} = \tilde{\boldsymbol{g}}_j$ The initial values of $\tilde{\alpha}_i^s$ are set to the elements of the first column of $\boldsymbol{U}$. For the optimization problem in (4.16), the limited-memory Broyden–Fletcher–Goldfarb–Shanno (L-BFGS) algorithm is employed. Using the results of (4.16), we can calculate the initialization for $\boldsymbol{\alpha}$, $\boldsymbol{\Delta r}$, $\boldsymbol{\psi}$, $\boldsymbol{h}_{\mathrm{t}}$. A model for $\tilde{\alpha}_i^s$ can be formulated as

$$\tilde{\alpha}_i^s = \alpha_i \exp\left(-\mathrm{j}\frac{2\pi}{\lambda}\Delta r_i \cos(\overline{\phi}^s - \psi_i)\right) \tag{4.19}$$

where $\overline{\phi}^s$ is the mean angle of arrival in segment s. An initial value for α_i, Δr_i, ψ_i can be obtained by

$$\hat{\Delta r}_i, \hat{\psi}_i = \underset{\Delta r_i, \psi_i}{\operatorname{argmax}} \left| \sum_{s=1}^{S} \tilde{\alpha}_i^s \exp\left(\mathrm{j}\frac{2\pi}{\lambda}\Delta r_i \cos(\overline{\phi}^s - \psi_i)\right)\right|^2, \tag{4.20}$$

$$\hat{\alpha}_i = \frac{1}{S}\sum_{s=1}^{S} \tilde{\alpha}_i^s \exp\left(\mathrm{j}\frac{2\pi}{\lambda}\hat{\Delta r}_i \cos(\overline{\phi}^s - \hat{\psi}_i)\right). \tag{4.21}$$

A grid search can be implemented to solve the maximization problem in (4.20). Estimates $\hat{\alpha}_i$, $\hat{\Delta r}_i$, $\hat{\psi}_i$ together with $\hat{\overline{\boldsymbol{\rho}}}$ from (4.16) can now be used to initialize (4.15).

5 Parameter Estimation Results

We estimated the parameters of the channel model in (4.5) using the methodology described in Section 4. The dimensions of the measurement data are $N = 16200$, $M = 8$ and $F = 2048$. Every second of measurement data has $N = 20$ data points. Although the measurement sounder has 64 dual-polarized antennas in total, distributed over height vertically spaced panels, we choose to select the first V-polarized antenna of each panel. The reason behind this is that the model in (4.5) assumes that the radiation patterns of the receive antennas are

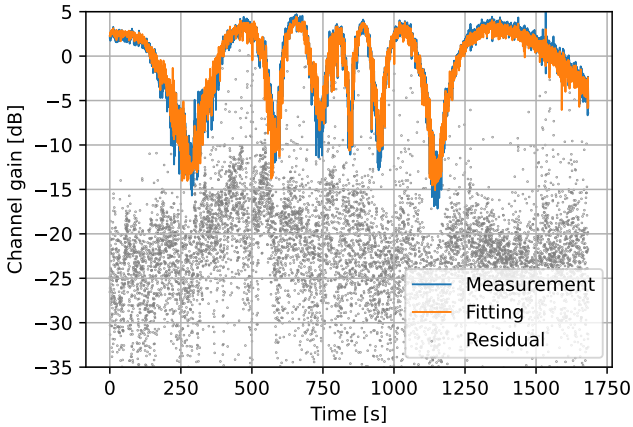

Figure 6: Fit of the model to the measurements (amplitude).

equal. However, in a real antenna array, the antennas can have a slightly different pattern depending on their location in the array. The segment size W was chosen as $W = 1200$, which corresponds to one minute of measurement data. An effective Earth radius r_e of 8500 km is assumed in accordance with standard practice [14].

5.1 Model Fit and Residual

In Fig. 6 the general fit of the model can be observed where the measured and modeled narrowband channel gain for the first antenna are plotted. Visually, the fitted model closely matches the model as it largely overlaps with the measured channel. Fig. 7 shows that the proposed model can also accurately model the phase difference between channels. Fig. 7 includes the phase difference between antenna 1 and 3 over the measurement time. The residual is depicted in Fig. 6 as small dots and is calculated as

$$\boldsymbol{R} = \boldsymbol{Y} - \boldsymbol{G}(\hat{\boldsymbol{\theta}}). \tag{5.1}$$

The residual gives an indication of three elements: 1) the performance of the estimator, 2) the accuracy of the model, and 3) the variance of the noise term. For channel characterization and, therefore, range performance evaluation, it would be useful to characterize the noise term that is attributed to the incoherent scattering. However, due to the "averaging" of the reflection coefficient over space and time of the model in (4.5), a model mismatch inherently exists. Therefore, we cannot say anything meaningful about the statistics of incoherent scattering. We can, however, treat the residual as zero-mean complex Gaussian noise term and

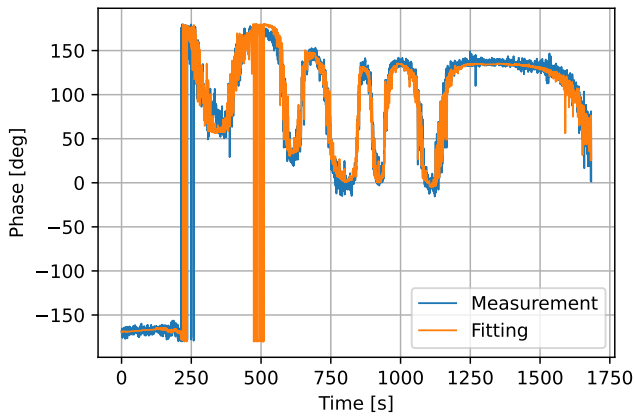

Figure 7: Fit of the model to the measurements (phase difference between antenna 1 and 3).

use its variance to assess the ranging performance. To further assess the residual, we calculated the residual variance for each antenna and each time window of 100 s and visualized the result in Fig. 8. The figure shows two distinct parts in time with a separation at around 900 s, with the left part having a higher variance than the right part. At this point in time, the vessel has changed its heading. Hence, the change in the heading indicates that this might be attributed to the radiation pattern of the transmit antenna. A change in antenna gain as a consequence of a change in angle of departure is modeled by β_j; however, the two-ray model used in this paper assumes that the antenna gain is equal for both the line-of-sight ray and the reflection ray. Hence, the magnitude of the residual being correlated with the heading of the boat indicates that this assumption might not be valid. Yet, the validity of every model depends on its application, and later on, it will be shown that the ranging performance is still satisfactory using this assumption.

5.2 Reflection Coefficient

In the field of channel modeling, researchers have favored faster asymptotic methods over electromagnetic (EM) simulations to calculate coherent reflection coefficients. Various methods have been developed to model these coefficients while accounting for sea state conditions. These methods can be categorized into two approaches. The first approach is based on the Kirchhoff approximation, where reflection is modeled by multiplying the Fresnel reflection coefficient with a rough-

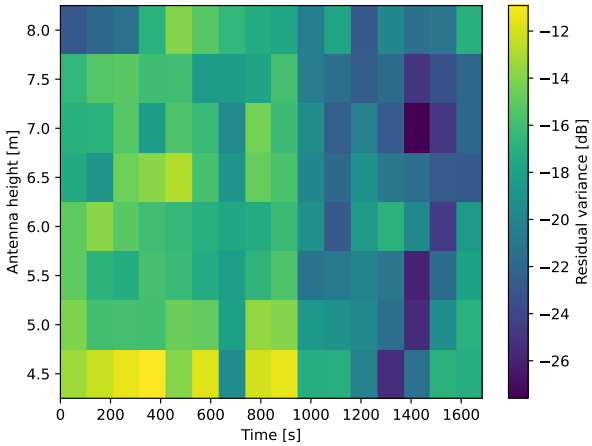

Figure 8: Average residual variance in dB for different antenna height and time windows.

ness factor. This approach was first introduced by [17] (known as the "Ament approximation") and similarly by [18] (the "Miller-Brown approximation"). The simpler Ament approximation can be derived as follows:

$$\rho(\theta) = \rho_0(\theta) \int_{-\infty}^{+\infty} \exp(-\mathrm{j}2k_0 z \sin\theta)\, p_z(z)\, \mathrm{d}z, \tag{5.2}$$

where ρ_0 is the Fresnel reflection coefficient, $k_0 = \frac{2\pi}{\lambda}$, θ is the grazing angle of the incident field of the surface, and $p_z(z)$ is the sea surface height distribution. In [17], the sea surface height was assumed to follow a zero-mean Gaussian distribution with variance σ_z^2, then (5.2) becomes

$$\rho(\theta) = \rho_0(\theta) \exp\left(-2k_0^2 \sigma_z^2 \sin^2\theta\right). \tag{5.3}$$

These approximations have a limitation: they do not account for the shadowing effect, where not all points on rough surfaces receive illumination. The methods assume a zero-mean Gaussian surface height distribution, but when shadowing is considered, the height distribution of illuminated points deviates from this assumption. Specifically, the height distribution's mean increases while its variance decreases, as the deeper and shadowed points are not illuminated. New distributions for $p_z(z)$ that account for the shadowing effect [19–21] have been derived. For example, in [19], a distribution has been derived by introducing another parameter: the slope rms of the surface. In the remainder of the manuscript we refer to this model as the “Smith” model.

The geometric approach to approximating coherent reflection coefficients, as shown in equation (5.3) and including shadowing effects, has gained widespread acceptance in channel modeling and has been supported by multiple measurement studies, including [11–13, 22]. The second approach uses perturbative theory, known as the Small Perturbation Method (SPM), first derived by [23], which utilizes the spectrum of the surface. Although SPM is more sophisticated and works better for slightly rough surfaces and lower grazing angles, it lacks the intuitive nature and practicality of the first category.

We have calculated the values for the coherent reflection coefficient according to the model of Ament [17], Smith [19] and the SPM [21] and plotted the results in Fig. 9 and 10, together with the estimation results of Section 4. Matlab code provided by [21] was partially used in this task. The parameters used for the models are the root mean square (RMS) surface height $\sigma_z = 0.17$ and the RMS surface slope $\sigma_s = 0.17$, which were obtained from the simulation of a sea surface using the model in [24] with a wind speed at 10 m elevation of 5 m/s. As expected, there is a reduction in the magnitude of the reflection coefficient relative to the Fresnel coefficient because the Fresnel coefficient is derived for smooth surfaces, while the sea surface is a rough surface most of the time. The estimates follow the same downward trend as the grazing angle increases, which agrees with the models. For the amplitude of the reflection coefficient, there appears to be a good agreement with the Ament and Smith model. However, the Smith model does not model the phase of the reflection coefficient well. The large phase disagreement can be attributed to the change in the mean of the surface height distribution when adjusting for shadowing. The SPM model, on the other hand, gives a more accurate phase prediction. However, its prediction does not perform better than the Ament or Fresnel model. Note that the estimated phase of the reflection coefficient could also be attributed to small errors in the height of the array above the sea surface. The mismatch of the models with the reflection coefficient estimates may be the result of an inaccurate estimate of the parameters of the sea state σ_z and σ_s. In fact, these are also varying with time. Therefore, an approach to model the coherent reflection coefficient could be to assume a normal-distributed sea surface and estimate the mean μ_z and variance σ_z^2 based on the estimated values of the reflection coefficient, effectively estimating the sea state from the radio channel. In this case, (5.2) can be expressed as

$$\rho(\theta) = \rho_0(\theta) \exp\left(-\mathrm{j}2k_0\mu_z - 2k_0\sigma_z^2\right) . \tag{5.4}$$

Using the ordinary least squares technique we estimated the parameters $\mu_z = 0.023$ and $\sigma_z = 0.11$ and depicted the model fit in Fig. 9 and 10. In the figure,

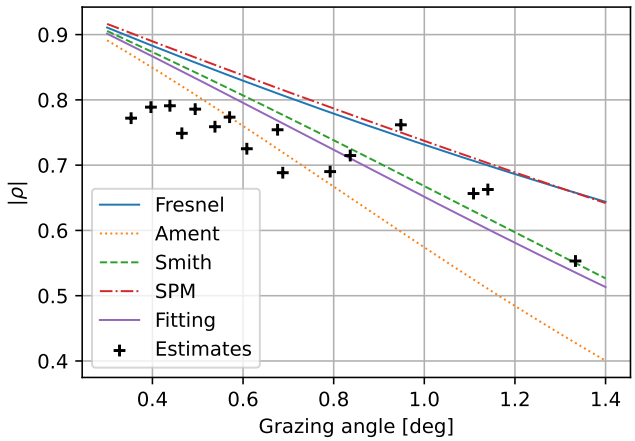

Figure 9: Absolute value of the estimated reflection coefficients and the models from literature.

we can observe that the absolute value of the fitting reflection coefficient model agrees well with the Smith. The phase of the fitted reflection coefficient fits the measurement better than the other models.

5.3 Transmit Antenna Height

The results of the transmission antenna height estimation are shown in Fig. 11. The top plot shows the moving average of the estimated transmit antenna height based on the channel measurements and based on the IMU and RTK data. The moving average was applied to improve visibility and show that the local mean of the antenna height changes over time due to the heeling of the sailing boat, which depends on the wind speed. There is a good agreement of between the two estimates, yet it is not possible to say which one is more correct since we do not have any error statistics of the IMU. The bottom plot shows the direct estimate of the transmit antenna height during a short segment of the measurement. The figure shows a smooth and periodic change in antenna height over time. The period is around 2 s, which is in line with what one would expect from a changing sea surface. The global mean of the transmit antenna height is 9.97 m and the standard deviation is 0.15 m. The local standard deviation is 0.10 m.

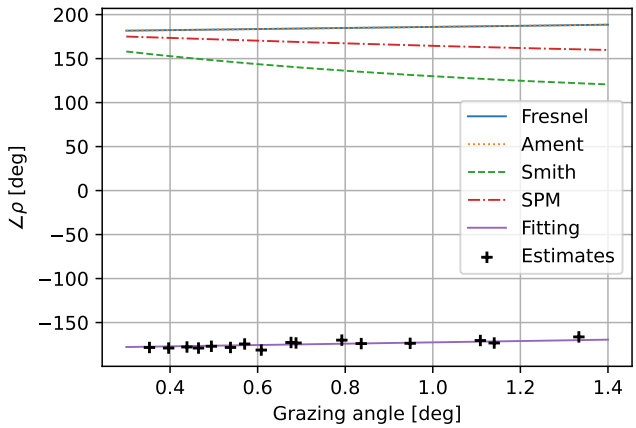

Figure 10: Phase of the estimated reflection coefficient and models from literature.

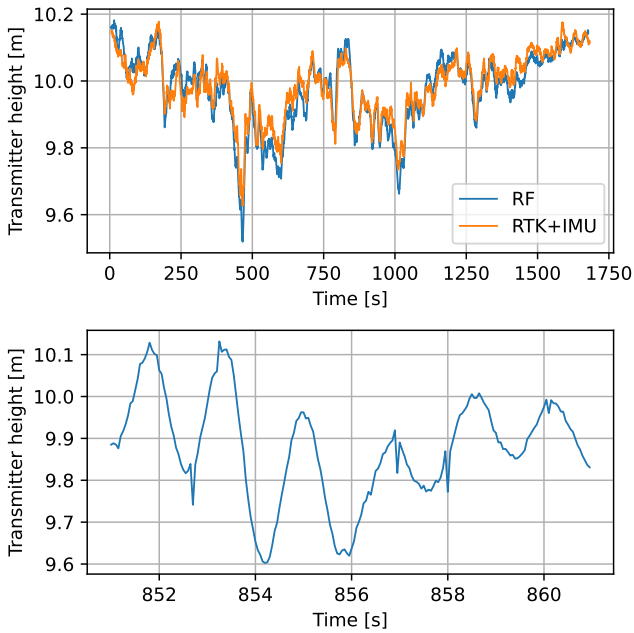

Figure 11: *Top*: Moving average of the estimated transmitter height based on channel estimation and RTK+IMU data. *Bottom:* Unfiltered antenna height estimates based on the channel over a period of 10 seconds.

6 Range Estimation Results

In this section, we use the calibration and modeling results of the previous sections to assess the real-world ranging performance with measurements. We employ the same estimator as in (2.3) but change the model for $\boldsymbol{g}$:

$$[\boldsymbol{g}(d)]_i = \alpha_i \exp\left(-\mathrm{j}\frac{2\pi}{\lambda}(r_{\mathrm{los},i} + \Delta r_i \cos(\phi - \psi_i))\right) \times \left(1 + \rho_i \exp\left(\frac{-\mathrm{j}4\pi h'_{\mathrm{r},i} h'_{\mathrm{t}}}{\lambda d}\right)\right). \tag{6.1}$$

where the parameters are as introduced in the previous sections. For ρ_i we use the model in (5.4) with the estimated values μ_z and σ_z^2 in Section 5. Note that the variables $r_{\mathrm{los},i}$ and ρ_i also depend on the range. Because the array is slightly tilted, we have to include the ground-truth angle-of-arrival ϕ in our signal model. In a practical deployment, this would not be the case as the location of the vessel is unknown. If additional antennas are deployed in the horizontal direction, the range and the angle-of-arrival could most likely be jointly estimated. A simpler approach is to mechanically calibrate the array to point straight down to the center of the earth, which was unfortunately not done in our measurement as we did not foresee this issue. In Section 5.3, it was shown that the local mean of the antenna height is changing, i.e. it is a non-stationary process. This means that if we used the global mean of the antenna height in (6.1), the local mean of the range error will not be zero. Therefore, we used the local mean within a time window of 10 s of the transmit antenna height obtained from the IMU to estimate the range. The snapshot-based range error is shown in Fig. 12 with the blue line. The measurement variance is calculated using (2.10) with parameters $\mu_{h_\mathrm{t}} = 9.97$, $\sigma^2_{h_\mathrm{t}} = 0.01$, $\sigma^2_\chi = 0.021$, and is shown in Fig. 12. Here, we have assumed $\sigma^2_\chi \gg \sigma^2_\omega$. A Kalman filter was applied to further reduce the variance of the ranging estimate from an RMSE of 15.7 m to an RMSE of 6.3 m. The Kalman filter has two states: the range d and its velocity v_d, and uses a constant velocity motion model. Because the variance of (2.10) is significantly larger than (2.8), the Kalman filter mainly filters out the ranging errors due to the local changes of h_t. Hence, the ranging accuracy is limited by the accuracy of the local mean transmit antenna height. This limitation could potentially be alleviated when three base stations are utilized to estimate the position, as the transmit antenna height could also be estimated jointly with the position. Further investigation and verification of the joint estimation of the transmit antenna height and position are planned as part of future work.

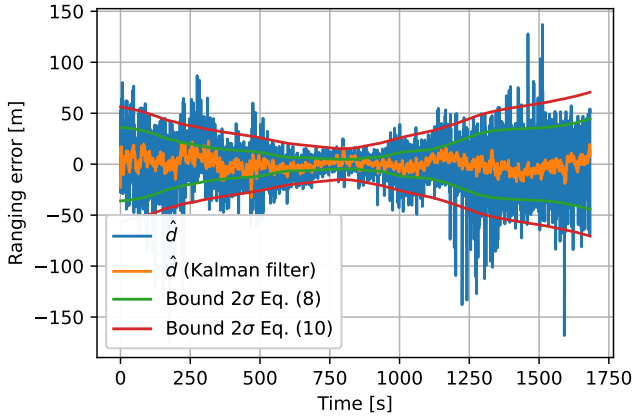

Figure 12: Range estimation result as a function of time.

7 Conclusion

We conclude that in the two-ray propagation environment at sea, large-aperture vertical arrays are not only effective in mitigating sea surface fading, but are also useful for ranging as part of a redundant positioning system for GNSS. The proposed ranging method does not require time synchronization between base stations and is suitable for narrowband systems. This method can be applied in a multilateration scenario with multiple base stations or with a single base station when combined with an angle-of-arrival estimate. The ranging performance depends on several factors: proper calibration of the RF chains, ensuring that the array is perfectly vertical, and having knowledge of the reflection coefficient. Our study demonstrates that calibration can be performed over-the-air and that the influence of the sea state can also be characterized through measurements. When effective calibration is achieved, and the vessel's antenna height is known or can be reliably estimated, the variance of the range estimate scales with the fourth power of the range for a constant SNR. To address the large variance at greater distances, an approach that integrates ranging information over time, such as a Kalman filter, may be necessary to achieve the desired performance. If the vessel's antenna height is not exactly known, variations in the antenna height will dominate the ranging performance. However, if the local mean and variance of the antenna height are known, accurate ranging can still be achieved using a Kalman filter, as demonstrated by our results. Using only eight vertically distributed antennas, a ranging RMSE of 6.3 m could be achieved for distances

between 700 m and 2800 m.

Acknowledgments

The authors would like to acknowledge the help of Christian Nelson, Juan Vidal Alegría, Aleksei Fedorov during the measurement campaign. In addition, the authors would like to thank the Klagshamn Harbor Association for allowing us to use part of the harbor infrastructure for our measurement campaign.

References

[1] C. Günther, "A Survey of Spoofing and Counter-Measures," *NAVIGATION*, vol. 61, no. 3, pp. 159–177, 2014.

[2] S. Saleh, P. Zheng, X. Liu, H. Chen, M. F. Keskin, B. Priyanto, M. Beale, Y. Ettefagh, G. Seco-Granados, T. Y. Al-Naffouri, and H. Wymeersch, "Integrated 6g tn and ntn localization: Challenges, opportunities, and advancements," 2025. [Online]. Available: https://arxiv.org/abs/2501.13488

[3] International Maritime Organization, "MSC.1/Circ.1575 Guidelines for shipborne position, navigation and timing (PNT) data processing," June 2017. [Online]. Available: https://www.imo.org/en/OurWork/Safety/Pages/Docs-ShipborneRC-NavigationEquipment.aspx

[4] C. Casetti, "Get Yourself a Private, Portable 5G Network [Mobile Radio]," *IEEE Vehicular Technology Magazine*, vol. 18, no. 2, pp. 9–15, 2023.

[5] The Secretary General of the International Telecommunication Union and The Secretary General of the International Civil Aviation OrganizationThe Secretary General of the International Maritime Organization, "Protection of the radio navigation satellite service from harmful interference," 2025. [Online]. Available: https://www.itu.int/en/mediacentre/Documents/2025/ICAO-IMO-ITU-Joint-Statement.pdf

[6] D. Dardari, A. Conti, U. Ferner, A. Giorgetti, and M. Z. Win, "Ranging With Ultrawide Bandwidth Signals in Multipath Environments," *Proceedings of the IEEE*, vol. 97, no. 2, pp. 404–426, Feb. 2009.

[7] L. Italiano, B. C. Tedeschini, M. Brambilla, H. Huang, M. Nicoli, and H. Wymeersch, "A tutorial on 5g positioning," *IEEE Communications Surveys Tutorials*, pp. 1–1, 2024.

[8] M. Sandra, G. Tian, X. Cai, and A. J. Johansson, "Antenna Array Configuration for Reliable Communications in Maritime Environments," in *2022 IEEE 95th Vehicular Technology Conference: (VTC2022-Spring)*, Jun. 2022, pp. 1–5.

[9] A. Goldsmith, *Wireless Communications*. Cambridge University Press, 2005.

[10] W. Wang, R. Raulefs, and T. Jost, "Fading Characteristics Of Ship-To-Land Propagation Channel At 5.2 GHz," in *OCEANS 2016 - Shanghai*, Apr. 2016, pp. 1–7.

[11] R. Raulefs, M. Bellido-Manganell, A. Dammann, M. Walter, and W. Wang, "Verification and modeling of the maritime channel for maritime communications and navigation networks," *Frontiers in Marine Science*, 2023.

[12] W. Wang, R. Raulefs, and T. Jost, "Fading Characteristics Of Maritime Propagation Channel For Beyond Geometrical Horizon Communications In C-Band," *CEAS Space Journal*, vol. 11, no. 1, pp. 95–104, Mar. 2019.

[13] K. Yang, A. F. Molisch, T. Ekman, T. Røste, and M. Berbineau, "A Round Earth Loss Model and Small-Scale Channel Properties for Open-Sea Radio Propagation," *IEEE Transactions on Vehicular Technology*, vol. 68, no. 9, pp. 8449–8460, Sep. 2019.

[14] J. C. Schelleng, C. R. Burrows, and E. B. Ferrell, "Ultra-Short Wave Propagation," *The Bell System Technical Journal*, vol. 12, no. 2, pp. 125–161, Apr. 1933.

[15] S. M. Kay, *Fundamentals Of Statistical Signal Processing: Estimation Theory*. USA: Prentice-Hall, Inc., 1993.

[16] M. Sandra, C. Nelson, X. Li, X. Cai, F. Tufvesson, and A. J. Johansson, "A Wideband Distributed Massive MIMO Channel Sounder for Communication and Sensing," *IEEE Transactions on Antennas and Propagation*, vol. 73, no. 4, pp. 2074–2085, Apr. 2025.

[17] W. S. Ament, "Toward a Theory of Reflection by a Rough Surface," *Proceedings of the IRE*, vol. 41, no. 1, pp. 142–146, Jan. 1953.

[18] A. R. Miller, R. M. Brown, and E. Vegh, "A New Derivation For The Rough Surface Reflection Coefficient And For The Distribution Of Sea Wave Elevations," *NASA STI/Recon Technical Report N*, vol. 84, p. 17453, Sep. 1983.

[19] B. Smith, "Geometrical Shadowing Of A Random Rough Surface," *IEEE Transactions on Antennas and Propagation*, vol. 15, no. 5, pp. 668–671, Sep. 1967.

[20] R. J. Wagner, "Shadowing Of Randomly Rough Surfaces," *J. Acoust. Soc. Am.*, vol. 41, pp. 138–147, 1967.

[21] C. Bourlier, *Radar Propagation And Scattering In A Complex Maritime Environment*, Jul. 2018.

[22] W. Wang, G. Hoerack, T. Jost, R. Raulefs, M. Walter, and U.-C. Fiebig, "Propagation Channel At 5.2 GHz In Baltic Sea With Focus On Scattering Phenomena," in *2015 9th European Conference on Antennas and Propagation (EuCAP)*, Apr. 2015, pp. 1–5.

[23] S. O. Rice, "Reflection Of Electromagnetic Waves From Slightly Rough Surfaces," *Communications on Pure and Applied Mathematics*, vol. 4, no. 2-3, pp. 351–378, 1951.

[24] T. Elfouhaily, B. Chapron, K. Katsaros, and D. Vandemark, "A Unified Directional Spectrum For Long And Short Wind-Driven Waves," *Journal of Geophysical Research: Oceans*, vol. 102, no. C7, pp. 15 781–15 796, 1997.


ctrl
+
d